UCLouvain

epl

École polytechnique de Louvain

Application of surface analysis techniques to the study of metal carboxylates in Southern Netherlandish oil paintings

Towards a better understanding through ToF-SIMS and XPS

Author: **Sarah Gonzalez Merino**
Supervisors: **Arnaud Delcorte, Francisco Mederos-Henry**
Readers: **Sophie Hermans, Jana Sanyova**
Academic year 2022–2023
Master [120] in Physical Engineering

Acknowledgements

Completing this master's thesis would not have been possible without the support and encouragement of numerous individuals, to whom I am deeply grateful.
First and foremost, my sincere thanks to my supervisors, Pr. Arnaud Delcorte and Pr. Francisco Mederos-Henry, for their kind and thoughtful mentorship. Their invaluable advice and unwavering support kept me motivated throughout this journey. Thanks also to the two readers, Pr. Sophie Hermans and Pr. Jana Sanyova, for agreeing to read and being part of the committee of this master's thesis.
I extend my appreciation to Claude Poleunis and Pierre Eloy for their technical expertise and willingness to help. Their assistance was crucial in overcoming challenges. I also want to acknowledge all those who have contributed, like the team at KIK-IRPA who prepared all the samples for their fastidious work.
I am also thankful to the C2 lab team for providing a stimulating environment and fostering a sense of camaraderie, with special gratitude for the fellow master's students I have befriended along the way.
To my dear family and friends, thank you for your unwavering encouragement and love throughout my academic journey. Especially to my mom and grandfather, Nicolas, Shauna, and those who have contributed in any way even if not mentioned here, thank you for your understanding and support during this process.

Abstract

Historical paintings form an important aspect of our cultural heritage and their preservation is vital for honouring our history. Metal carboxylates, particularly copper and calcium oxalates, pose significant threats to historical oil paintings, and comprehending them is vital for proper artwork restoration. This work comprises two main sections.

The main study utilized ToF-SIMS to detect and locate copper oxalate and calcium oxalate in cross-sections from Southern-Netherlandish oil paintings. The aim was to establish a reliable method for identifying these compounds, given their frequent occurrence in damaged paintings. Assessing the reliability and effectiveness of ToF-SIMS in achieving these objectives can provide insights into its potential for future similar research.

We also characterized XPS spectra of metal oxalate powders. The XPS analysis of calcium, copper, lead, and zinc oxalates in historical samples has remained so far unexplored, making this theoretical investigation crucial for potential future research and foundational for historical sample examinations.

Our results showed that we could detect $CuC_2O_4^-$ and $CaC_2O_4^-$ in ToF-SIMS. To confirm the presence of CuOx and CaOx in the samples, we verified consistency with ATR-µFTIR results, ion localization, and peak definition. Unfortunately, the mass resolution of ToF-SIMS does not allow us to conclusively confirm whether these peaks correspond to these ions. Exploring alternative techniques with enhanced mass resolutions, such as delayed extraction (which showed successful enhancement in this study), could be beneficial.

The XPS study showed that it is possible to identify distinct characteristics of CaOx, CuOx, PbOx, and ZnOx, suggesting their potential identification in complex samples. Considering their limited detectability by ToF-SIMS, employing XPS for 3D analysis, particularly with a GCIB-equipped instrument, could be an intriguing avenue. However, before applying this to historical cross-sections, a systematic mock-up procedure is essential due to potential chemical changes and concerns about representation accuracy.

Acronyms and abbreviations

ATR-µFTIR	Attenuated total reflectance micro-Fourier-transform infrared spectroscopy
BG	Bandgap
BSMA	Bio- and Soft Matter
CaOx	Calcium oxalate
CuOx	Copper oxalate
DE	Delayed extraction
D-SIMS	Dynamic SIMS
ESCA	Electron spectrometry for chemical analysis
FWHM	Full width at half maximum
GCIB	Gas cluster ion beam
IMCN	Institute of Condensed Matter and Nanoscience
IMFP	Inelastic mean free path
KIK-IRPA	Koninklijk Instituut voor het Kunstpatrimonium - Institut Royal du Patrimoine Artistique
LMIG	Liquid metal ion gun
MC	Maximal count
MetOx	Metal oxalate
OM	Optical microscopy
PbOx	Lead oxalate
POL	Polarised
ROI	Region of interest
SEM	Scanning electron microscopy
SIMS	Secondary ion mass spectrometry
SOS	Spin-orbit splitting
S-SIMS	Static SIMS
TC	Total count
ToF	Time-of-flight
UV	Ultraviolet
VB	Valence band
XPS	X-ray photoelectron spectroscopy
XR	X-ray
ZnOx	Zinc oxalate
µSR-XRD	Micro X-ray diffraction with synchrotron radiation

Contents

Introduction

The preservation of cultural heritage, including paintings, is essential in the context of a globalized world. It honors roots, nurtures a sense of pride, and fosters a harmonious coexistence among diverse communities. Safeguarding cultural heritage ensures that future generations can continue to benefit from its richness and contribute to its ongoing evolution. Historical paintings, particularly prone to degradation, require special attention to maintain their original appearance. From the discoloration of historical paintings to the appearance of thick crusts disfiguring them, various types of degradation appear and can be very difficult to overcome.

Metal oxalates and soaps are part of the compounds that can form on the surface of paintings and inside the paint layers, causing damage over time. Researchers from around the globe are seeking to develop analytical methodologies to better understand the origin and accumulation of these compounds on and below the paint surface. Scientists also study the chemical and physical properties of the materials used in the creation of the painting, such as pigments and binders, as well as the interactions between them. Several studies have tried techniques such as Raman and attenuated total reflectance micro-Fourier-transform infrared spectroscopies (ATR-µFTIR) or scanning electron microscopy (SEM). A better understanding of how metal carboxylates form in aging oil paint materials will help to preserve paintings and preventing further damage. Overall, the development and application of these analytical methods can have significant positive implications for preserving cultural heritage objects. At the same time, it can shed new light on the materials and techniques used by artists throughout history.

The first challenge of this work concerns the detection of metal carboxylates, especially calcium and copper oxalates, in Southern Netherlandish oil paintings using ToF-SIMS (time-of-flight secondary ion mass spectrometry). Indeed, such species have already been investigated using ATR-µFTIR spectroscopy and ToF-SIMS, and this work aims to assess the role of the latter in this field and which novel pieces of information it could offer. In the perspective of future XPS (X-ray

photoelectron spectroscopy) studies and to obtain information about the physical properties of common metal oxalates, XPS investigation has also been performed.

This master's thesis was supervised by Prof. Arnaud Delcorte of the Institute of Condensed Matter and Nanosciences (IMCN) at UCLouvain, in the Bio- and Soft Matter (BSMA) research division, as well as Prof. Francicso Mederos-Henry from the Royal Institute for Cultural Heritage (KIK-IRPA). It is part of the continuation of Hadelin Le Brun's master's thesis, completed in 2021 which focused on metal oxalates and soaps in oil paintings from the Southern Netherlands using ToF-SIMS [1]. The latter was made in the scope of the MetOx project, an interdisciplinary project aiming to enhance our understanding of oil paint material's aging and alteration phenomena by uniting conservation scientists, conservators-restorers, and art historians [2, 3].

This introduction is followed by four main parts. First, the state of the art provides a literature review presenting the theoretical background necessary to understand the subject. Different aspects are addressed, starting with knowledge related to the genre of painting and degradation observed in the studied samples. Then, the analytical techniques are detailed. This includes the roles and working principles of ToF-SIMS and XPS.
Secondly, the goals of this research and the associated experiments are thoroughly outlined.
Thereafter, an experimental section describes the materials and methods used when working on this equipment. Samples and methodologies are specified for each experiment performed.
The last part gathers the results obtained during these studies and their interpretation. Limitations of the work performed are also discussed and future prospects are suggested.

Part I

State of the art

Chapter 1

Painting techniques and components of interest

1.1 Typical composition of a painting

As stated in the introductory section, this work focuses on artworks originating from the Southern Netherlands and conceived between the 15^{th} and the early 17^{th} centuries. Pictorial art and its techniques did not cease evolving since their beginnings. Nevertheless, there are certain constants in the art of this time and place. Their identification is the first step towards a global understanding of how these objects degrade as they age. This section aims to provide relevant information necessary to understand the conducted experiments.
Let's start by investigating the complex layered structure of heterogeneous composition of a typical historical oil painting. Looking at a cross-section (an example is shown in Figure 1.1), different layers of different purposes and materials are clearly distinguishable. It can be divided into four main layers, written on the right of the picture, which can, in turn, contain several sublayers.

The layering takes place on a support, which is either a wood panel or a textile canvas. In Southern Europe, from the middle of the 16^{th} Century, and more accurately from the 17^{th} Century with regard to the Netherlands, canvas stretched on wooden frames started to take precedence over panels for easel paintings [4–6].

The support must be treated before the paint can be applied. This treatment is made of several preparation layers, including a ground layer, often chalk-based in Northern-Europe [7]. If so, its whitish color and the abundance of calcium carbonate ($CaCO_3$) allow its identification by diverse analytical methods. Gypsum ($CaSO_4 \cdot 2\,H_2O$) [8], an alternative to chalk, was also commonly found in the ground

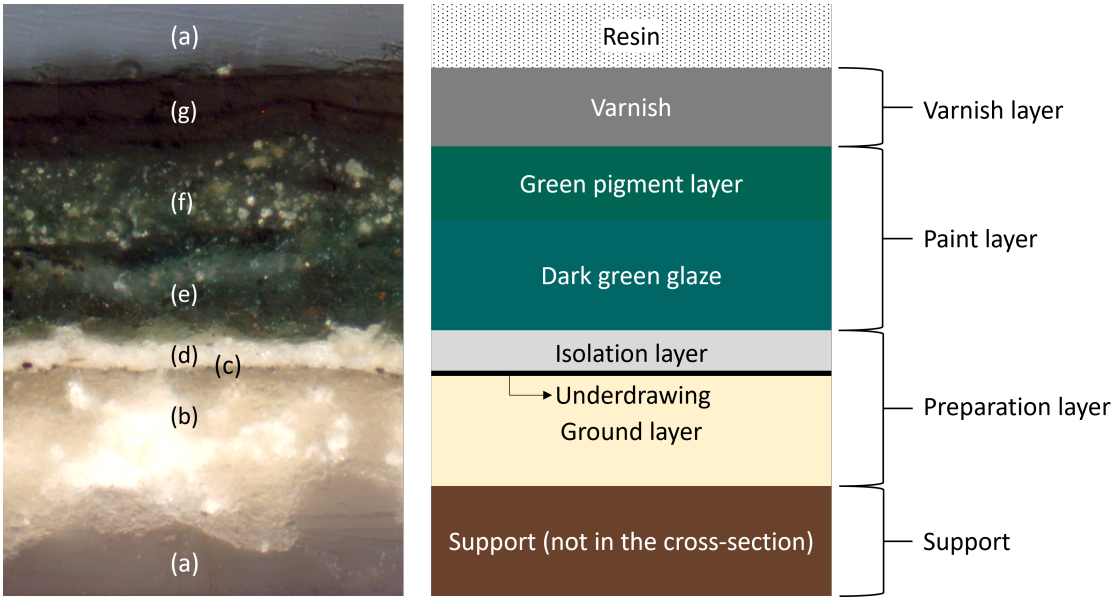

Figure 1.1: Example of layering taken from cross-section C17-085 (more information about this sample in Figure 8.6, section 8.2). The support is not present in this cross-section, but is supposed to lay underneath the ground layer. (a) Resin embedding the cross-section. (b) White ground layer. (c) Bone-black underdrawing. (d) Lead white isolation layer. (e) Dark-green glaze containing copper resinate. (f) Pigment layer containing malachite and lead-tin yellow. (g) Two varnish layers separated by a dirt layer, indicating that varnish has been applied in two different moments.

layers of 15^{th} Century altarpieces in Italy [9]. The chalk, gypsum or equivalent was combined with a binding medium such as oil or animal-skin glue containing collagen for instance, sometimes mixed with egg in tempera paintings [4, 10, 11]. On this ground layer can lie an underdrawing, traced for example with black chalk, charcoal or bone black [12].
These preparation layers can be completed by a primer, also called insulation or intermediate layer. They typically contain calcium carbonate or phosphates, lead white, and a lot of binder [11].

The main layer, the one that justifies the presence of the others, is the colored paint layer. It is sometimes composed of several sublayers, depending on the technique used by the artist. Pigments are mixed with an organic binder and sometimes additives such as powdered glass [11, 13]. Among the most commonly found pigments that are relevant in this work, there are green organo-copper pigment verdigris and red lake pigments. The composition of verdigris varies depending on the artwork [11]. Simonsen et al. give it the formula $Cu(CH_3COO)_2 \cdot H_2O$ [14].

Finally, after the paint had dried for about a year, one or more coats of transparent

varnish were applied. Located at the upper surface, it constitutes the protective layer between the paint and the air. The objectives of the varnish range from saturating the colors [12] to shielding them from environmental contaminants [4]. Ideally, it should also be and stay colorless, while some resin-based varnishes happen to turn yellow over time [15]. Typically, varnishes consist in organic biological substances made from natural resins like mastic, amber, copal, sandarac or dammar [6].

1.2 Degradation knowledge

As the years go by, many chemical reactions occur within these complex substrates, causing the visual appearance of the painting to deteriorate. This section gathers key facts on painting degradation and is strongly based on "Harmony in Bright Colors: Memling's "God the Father with singing and music-making angels" by Catherine Higgitt [16].

1.2.1 Degradation-related challenges in historical oil paintings

A very harmful consequence of aging is the appearance of opaque and extremely insoluble grey or brownish crusts on the surface of easel paintings. This kind of disfiguring layer is especially problematic on darker areas, where it can obscure the original illustration completely. When they form, these layers can be extremely unsightly due to their ability to scatter light and capture dirt particles, cementing them to the surface. Although these layers are typically thin on easel paintings, the scattering they induce can cause painted surfaces to appear faded or washed-out, which can be particularly disconcerting visually, especially in areas with low lighting. Figure 1.2 shows an example of a degraded oil painting before and after restoration.

Figure 1.2: *The Virgin and Child*, by Benvenuto di Giovanni, from the National Gallery, London (tempera on wood).

In addition to deteriorating the appearance of the painting, these layers also pose a challenge for conservation. Before attempting to remove them, it is important to carefully evaluate whether removal is necessary and what method should be used. In fact, permanent alteration of the underlying layers in which the degradation products develop, as well as the interfaces between these layers, has been noted. Due to their complex association with internal layers and high insolubility in restoration solvents, selectively removing such crusts is a complicated task. Informed decision-making is key in addressing this cleaning challenge.
Furthermore, material characterization may also be affected. Degradation products and resulting changes settle in the already complex environment of the multilayer structure of the painting, complicating the interpretation of analytical data and the identification of the original materials used.

1.2.2 Prevalent species

The most common degradation products are metal oxalates and soaps. They both are complexes between a carboxylate-containing species and a metal cation. The oxalate anion is referred to as a bidentate dibasic ligand due to its two negatively

charged oxygen atoms that serve as bonding sites for metal ions. With these two pairs of electrons, it can form two coordinate covalent bonds in the oxalate anion [17].

While this work is more focused on oxalates, metal soaps like palmitate and stearate have often been found in historical oil paintings with various techniques such as ToF-SIMS [18], ATR-µFTIR, µRaman, and µSR-XRD (micro X-ray diffraction with synchrotron radiation) [9]. These species and their chemical formulas are displayed in Figure 1.3. Concerning oxalate, the metal is often calcium, copper, lead or zinc, of which the corresponding oxalates are respectively abbreviated CaOx, CuOx, PbOx and ZnOx in this manuscript. In the study of the degradation in Southern-Netherlandish Memling's *God the Father with Singing and Music-Making Angels*, dating from the end of the 15$^{\text{th}}$ century, C. Higgitt revealed the preponderance of calcium and copper oxalates. In particular, the MetOx project research revealed that copper oxalates are often associated with the presence of verdigris.

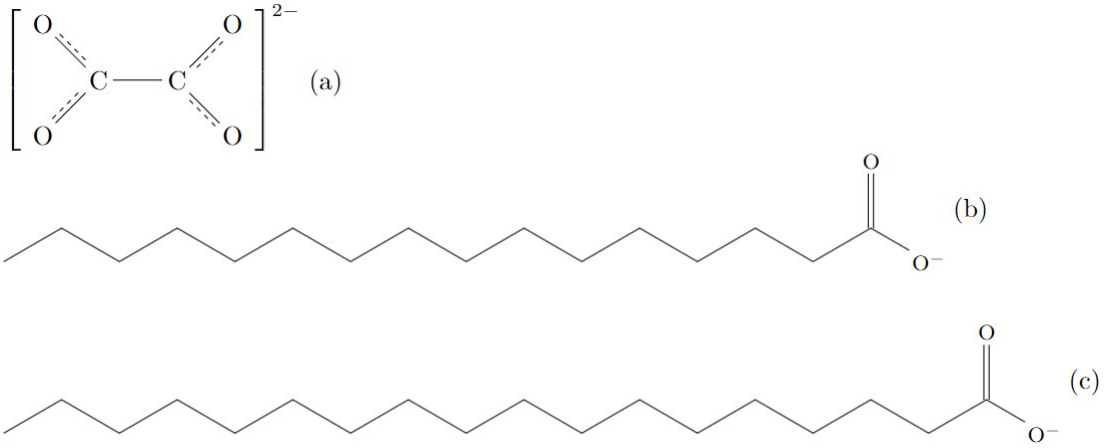

Figure 1.3: Species of interest in painting degradation. (a) Oxalate anion: $C_2O_4{}^{2-}$ [19]. (b) Palmitate anion: $C_{16}H_{31}O_2{}^-$ [20]. (c) Stearate anion: $C_{18}H_{35}O_2{}^-$ [21].

Problematic gray layers such as mentioned in subsection 1.2.1, mainly composed of calcium oxalate and other constituents that correspond to dirt confined to the surface, have also been found. More precisely, two calcium oxalate species were identified: calcium oxalate monohydrate ($CaC_2O_4 \cdot H_2O$) and dihydrate ($CaC_2O_4 \cdot 2\,H_2O$), respectively known as whewellite and weddellite. The MetOx project demonstrated that they always appear mixed together in degraded historical paintings, and that whewellite transforms into its dihydrate form over time.

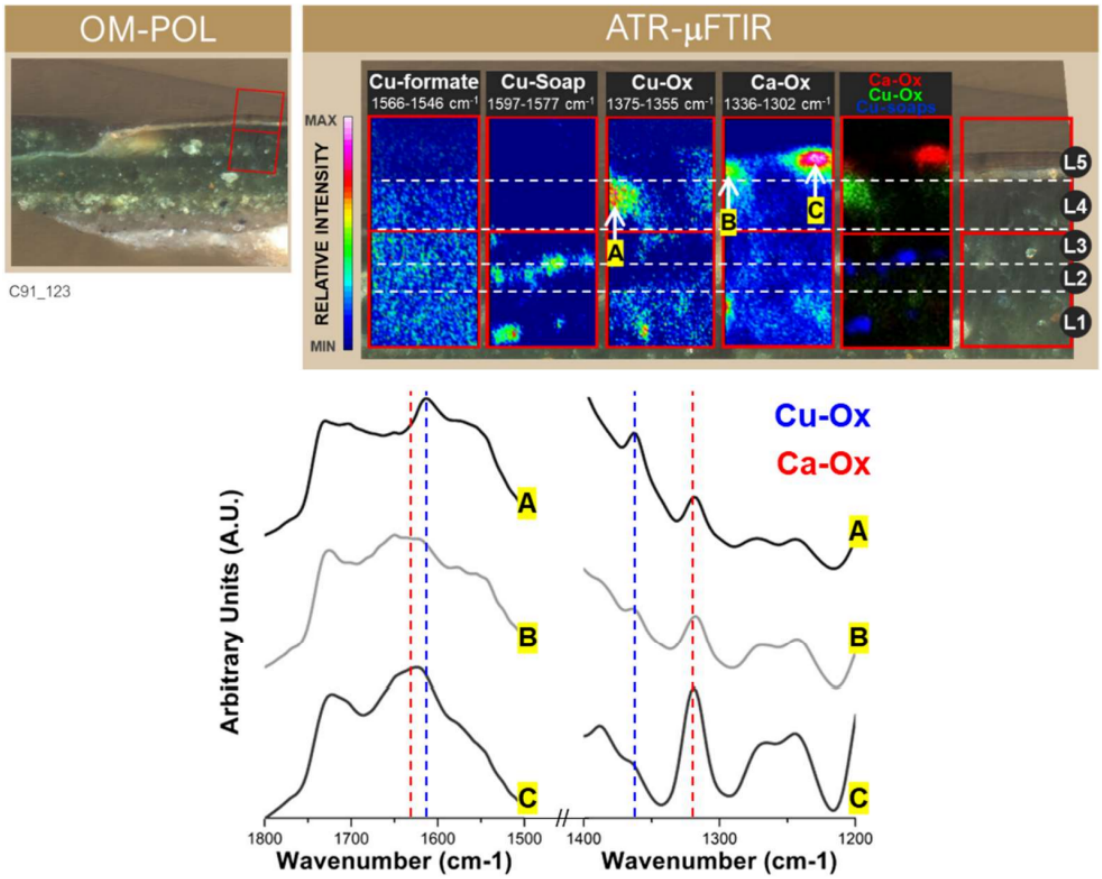

Figure 1.4: Microphotograph under polarized light (OM-POL) and ATR-µFTIR results showing copper formates, copper soaps, CuOx and CaOx colocalized in the verdigris-based paint layer of a fragment of *The Virgin Annunciate panel* of the Ghent altarpiece by Jan and Hubert Van Eyck, i.e. cross-section C91-123 [22].

Although the two hydrate forms of calcium oxalate are typically present in most oxalate-rich surface layers, CuOx have also been found in various historical oil paintings, as shown in Figure 1.4 [22]. As stated previously, their formation is not limited to the surface of painted artworks, and CaOx and CuOx have also been found in depth, at the level of the paint layers. More precisely, infrared spectra extracted from the CuOx and CaOx ATR-µFTIR mappings at points A, B and C in Figure 1.4 illustrate a gradual shift in the composition of metal oxalates, evolving from a mixture of copper and calcium oxalates towards a CaOx phase within the surface varnish.

1.2.3 Origin

An oxalate salt is formed as a result of a reaction between a metal ion and oxalic acid, as shown in Figure 1.5.

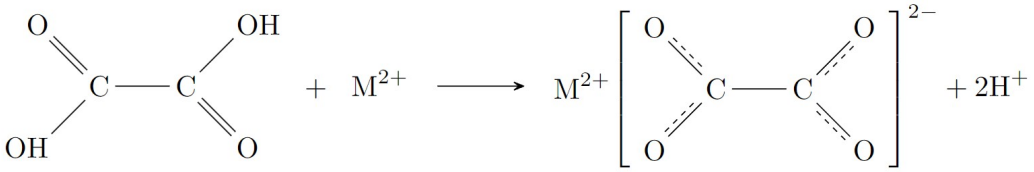

Figure 1.5: Oxalic acid and metal cation reacting to form metal oxalate. Adapted from [16].

Therefore, the formation of metal oxalates requires the presence of both these species somewhere within or on the paint layers. To this day, the precise sources of the oxalate anion remain uncertain, but various leads regarding their appearance have come to light. These causes can be divided in internal factors, coming from the painting itself (factors 1, 5 and 7 visible at the bottom of Figure 1.6), and external ones, assimilated to the environment in which it is located (factors 2, 3, 4 and 6 on the upper half of Figure 1.6). It should be noted that, broadly speaking, the factors outlined are not necessarily independent of each other.

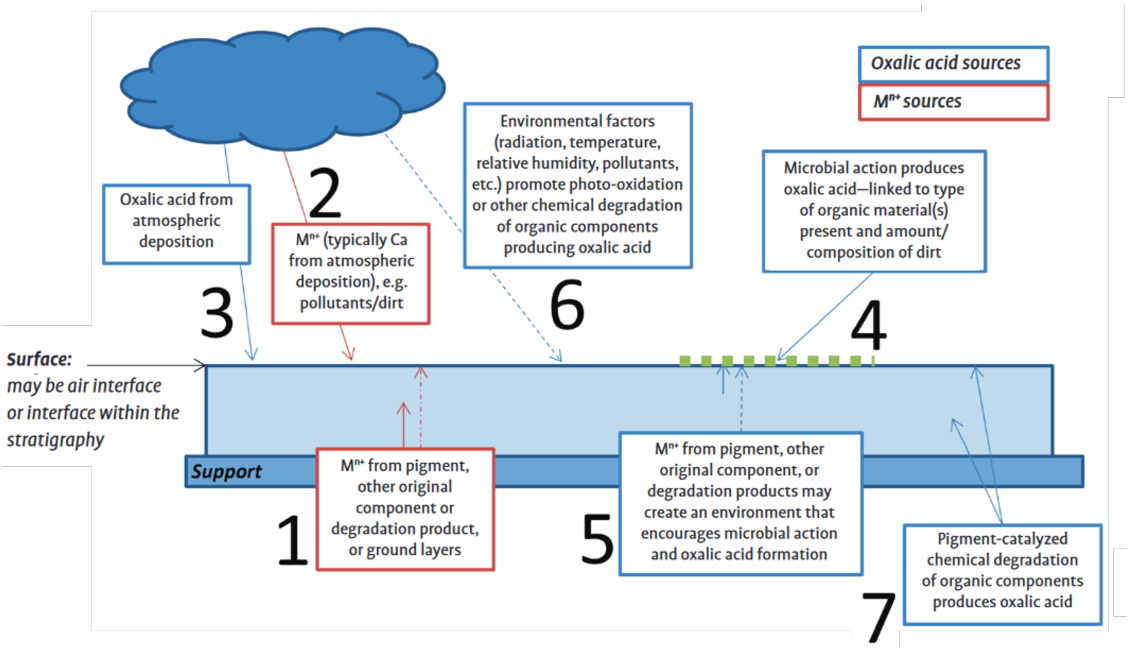

Figure 1.6: Sources of reactants leading to metal oxalate formation. The painting and its support are represented by blue rectangles. External factors are located above the surface of the artwork (upper half of the figure), while internal factors are located below [16].

Most metal cations originate from either the deposition of calcium-rich particles such as dirt on the surface, especially for oxalate crusts, (2) or from the paint or preparation layers (1).

In this second case, one possible explanation for the formation of metal oxalates is that they could be produced by a direct reaction between original compounds such as pigments and driers. If it is the case, the crucial factor would be the material's reactivity with acids such as oxalic acid. Another possibility is that the metal ions may originate from degradation products of original compounds.

As proved by the MetOx project [22], chemical degradation like photo-oxidation of organic components may also be favored by the environment in which the artwork is conserved (6). These environmental factors include temperature, high humidity and light exposure, especially ultraviolet radiation.
Additionally, the project stresses the importance of considering the likelihood of direct pigment-catalyzed or mediated chemical degradation of organic components, which can result in the production of oxalic acid (7). This varies with the organic species present in the components (binding medium, pigments, coatings, etc.) chosen by the artist(s) or, in some cases, added during conservation treatments. In particular, it is heavily dependent on the pigment (especially red lakes, ultramarine, verdigris and smalt) and its interaction with the binder and catalyzed by ultramarine, verdigris, madder lake and chalk white. Indeed, cadmium oxalate originating from cadmium sulfide pigments used in treatments may lead to oxalate formation, even if it is quite unusual in easel paintings. Chemical degradation processes are also influenced by external factors cited above.

1.2.4 Formation

Oxalate formation phenomena can be classified according to three categories, but certain situations may entail combinations of these groups.

The first group includes layers that are relatively uniform over the entire surface of a painting, without apparent correlation with particular pigments. This kind of crust usually results mostly from environmental factors and is of heterogeneous composition.
Oxalate-rich crusts may lie directly on the paint layers or over varnish. In the latter case, metal ions, generally calcium, come mainly from atmospheric sources, and the crusts also contain various dirt-related compounds and other salts such as silicates, carbonates, sulfates, and phosphates. Some microorganisms (bacteria, fungi, lichens) also generate oxalic acid as a byproduct of their metabolism. Chemical breakdowns like photo-oxidation may also promote the formation of oxalic acid that can react with calcium from the atmosphere. In easel paintings, oxalates have been found in the presence of every typical organic compound, whether original or

brought by restoration, but to various extents. The properties of the materials, the environment and the organic breakdown mechanisms can influence the formation of oxalate-containing layers. Therefore, they can also be favored when organic-rich varnishes or other coatings are exposed on the surface of paintings. Fortunately, oxalate layers on top of varnish layers are easier to remove.
When there is no resin-containing varnish between the oxalate layer and the paint, a glue coating can induce oxalic acid. Calcium ions may then arise from the gesso (mix of chalk and gypsum) preparation layer. As detailed in section 1.1, it can be chalked-based and thus contain a lot of $CaCO_3$ of which Ca^{2+} ions can migrate to the surface, especially if the paint layers are bound with an aqueous medium, thin or highly porous. However, when species associated with dirt are present in a calcium oxalate layer, it is likely that the calcium comes from the environment.
Eventually, oxalate crusts on top of varnish layers may sometimes develop more in darker areas as a result of the treatments the artwork has undergone in these regions, rather than because of the underlying original paint layers. More precisely, an application of additional varnish on these zones or the fact that the removal of dirt has only been performed on lighter sections could have promoted the formation of oxalate in the darker passages.

The second category also gathers surface oxalate crusts but those that are localized rather than uniformly distributed. As a matter of fact, their distribution is directly correlated with the pigment of the underlying paint layer. Areas containing glass siccatives or certain pigments, such as copper greens (verdigris for example), red lake pigments, or other blue pigments, are often associated with more observed oxalate layers. This correlation may be due to the properties of the pigment itself, the way it is applied and the compounds with which it tends to be mixed (the organic binder for instance), or both. For instance, when incorporated into a glaze, the mixture acquires translucency, which renders it more susceptible to photochemical degradation. By enabling light to penetrate deeper, the glaze is more vulnerable to the harmful effects of UV rays. Moreover, supplementary coatings might have been applied originally on areas containing these pigments, facilitating the formation of oxalic acid. Again, most of these crusts are calcium-based with an origin mostly environmental, even though the migration of calcium ions from other layers should not always be discarded. Indeed, calcium oxalate crusts often appear above calcium-rich pigment layers like ultramarine or some red lakes.
Glass-containing passages (like cobalt glass pigments or smalt) are also commonly found underneath these crusts, suggesting that they could be promoted by glass degradation. In addition to calcium, they also contain other species like potassium

sulfate and potassium calcium sulfate. Specifically, the alkali metal ions sodium and potassium can leach from the glass to its vicinity and react with the binding medium, forming metal soaps. Potassium may then reach the surface of the painting and form crusts by reacting with environmental species. Intermediate products could include metal oxalates with higher solubility, such as potassium oxalate.

Finally, the third and last class focuses on the formation of oxalate inside the paint layers. It is important to note that some paintings present metal oxalate from their bulk to their surface, blurring the distinction between this group and the previous one. The pigment may act as a source of metal ions or as a source of oxalic acid, facilitating the breakdown of organic materials within the binding medium.
In the case where metal ions come from the pigment, the oxalate is likely to come from the degradation of organic compounds such as the oil binder in the painting, even if environmental sources are not totally ruled out either, especially when the painting is porous or has cracks that favor the penetration of external species.
Verdigris pigment often contains copper oxalate. The high mobility of copper ions facilitates their migration from the paint or glaze layers to the surface coating, sometimes up to the varnish. The absence of copper on the paint's outermost surface, coupled with the presence of calcium, suggests that the latter primarily originates from the environment, since even the most mobile ions fail to reach that surface. There are two main reasons why calcium and copper oxalates are the most frequent oxalate salts encountered in Old Master paintings. First, it can be due to their high water-insolubility, which causes them to accumulate, unlike others that can be removed during restoration or converted into more stable or less soluble compounds. Secondly, pigments containing calcium and copper are the most soluble in acid, hence they have the highest reactivity with oxalic acid. Nevertheless, certain compounds employed in paintings can result in the formation of other metal oxalates. For example, zinc sulfate-based driers can promote the formation of zinc oxalate, while lead-tin yellow can contribute to the formation of lead oxalate. More soluble oxalates like ZnOx or PbOx may also appear at some point and be lost during cleaning or converted into more stable oxalates. On another note, when metal ions are in the presence of resin acids or egg yolk-based binders, they may interact with the fatty acids present and give rise to the formation of other metal carboxylates such as metal soaps. Correlations have been observed between the presence of copper and zinc soaps and the occurrence of their respective oxalates. However, it is noteworthy that while calcium oxalates are commonly found, reports on calcium soaps are relatively rare. Conversely, lead soaps are more frequently reported. Unfortunately, the reasons and mechanisms behind these phenomena are

still unknown to this day.
The severe chemical breakdown of the binding medium can also generate low molecular weight molecules like oxalic acid. Some pigments and calcium carbonate, as well as environmental causes such as the ones presented in subsection 1.2.3 may catalyze and promote this degradation process. This phenomenon is often observed in the presence of ultramarine, a blue pigment, or other pigments that tend to whiten over time, such as smalt. Additionally, the presence of zinc white has been linked to the formation of zinc oxalate or other carboxylates on the surface of paintings [14].

Chapter 2

ToF-SIMS: Role and working principle

ToF-SIMS is a surface analysis technique used for its remarkable sensitivity, high spatial resolution, depth profiling capabilities, and molecular information. This technique offers chemical information by collecting secondary ions emitted when ion beams impact the sample. Positive and negative ions are collected separately.

2.1 Instrumentation and operation

A typical ToF-SIMS instrument is represented in Figure 2.1. The analysis must be performed under ultra-high vacuum. The samples are first introduced into a preparation chamber (loadlock) before going into the analysis chamber, typically under a vacuum of 10^{-9} mbar [23].

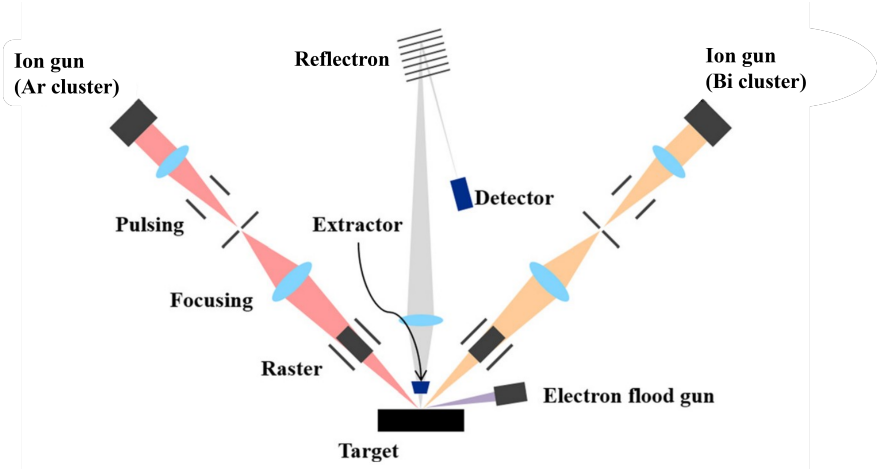

Figure 2.1: Schematic view of a ToF-SIMS instrument. Figure adapted from [24].

Two primary ion sources can be distinguished. The first one, in yellow in Figure 2.1, is a liquid metal ion gun (LMIG) and is used to analyze the surfaces of samples. The metal ions are typically gallium (Ga^+) or bismuth ($Bi_3{}^+$, $Bi_3{}^{++}$, $Bi_5{}^+$). These beams can be focused with high precision, offering a great spatial resolution.
A second type of source that can be used is a gas cluster ion beam (GCIB), represented in red in Figure 2.1. Argon is one of the most used elements for this kind of source, in the form of clusters of up to several thousand atoms ($Ar_{1000-5000}{}^+$). The important advantage of these clusters is that being composed of many Ar atoms, the energy per atom is really low (eV/atom). The desorption they cause is thus softer, and they are less destructive in depth [25]. Therefore, they can etch the surface of a sample without destroying the underlying layers, allowing molecular depth profiling.
The energy of these ion sources typically ranges from 1 eV to 50 keV and the shorter the pulse ($\sim$ 1 ns), the better for mass resolution.

The emitted particles are then channeled into the ToF mass analyzer. It has a high transmission and a resolving power in the 10^3, as well as a wide mass range [25]. Its working principle is based on the following relation:

$$E_k = \frac{mv^2}{2} = qV_{\text{acc}} \iff v = \sqrt{\frac{2qV}{m}} \tag{2.1}$$

where E_k is the kinetic energy, m the mass and v the velocity of the ion. q is the charge and V_{acc} is the constant acceleration voltage applied depending on the desired kinetic energy. Then, the ToF t_{flight} of an ion can be expressed as

$$t_{\text{flight}} = \frac{L}{v} = L\sqrt{\frac{m}{2qV}}, \tag{2.2}$$

where L is its path length in a field-free drift region. Therefore, ions with larger m/z ratios will have greater ToF. Another notable characteristic of ToF-SIMS is the monocharged nature of secondary species ($z = 1$), enabling their differentiation based on their mass m. This property ensures that secondary ions carry a single charge, simplifying the process of distinguishing and identifying them in ToF-SIMS analysis by mass-to-charge ratio.
After being pulsed and focused, the cation beam reaches the target sample. Following its impact on the surface, secondary ions are produced through sputtering from the topmost surface layers. If the surface is non-conductive, charges will accumulate on it over time and increase its surface potential, which can deflect and modify the kinetic energies of the emitted ions. Let's say that positive ions are

being collected. When leaving the surface, they will be repelled by its increasing positive charge, acquiring higher kinetic energies than expected and thus, shorter ToF. Since the mass resolution is directly correlated with the ToF distribution, this phenomenon can be heavily detrimental to the quality of the spectrum, broadening the peaks and sometimes resulting in loss of signal if the kinetic energies become greater that the ones accepted by the analyzer. A typical way to overcome this issue is to compensate the charge by bombarding the surface with electrons thanks to a low energy electron floodgun [26, 27].

Following their extraction and acceleration, the ions enter an ion mirror, also called reflectron, to enhance again the mass resolution. Initially, different emitted ions have a distribution of kinetic energies. As explained previously, a particle with a higher kinetic energy than expected will have a shorter ToF than expected. Thanks to this device, the higher the kinetic energy of an ion, the further it will travel through the reflectron before bouncing back (or never bounce back but collides with the roof of the reflectron if the energy is way too high) and thus extend its ToF, and vice-versa. This compensates the kinetic energy differences of the different ions and results in narrower spectral peaks. For insulating materials, the appropriate voltages must be determined for each analysis, depending on the level of charging [27].

Ultimately, the emitted ions reach the detector and data can be collected [28].

2.2 Physical principles

This section is strongly inspired by the book "ToF-SIMS: Materials Analysis by Mass Spectrometry" by J. C. Vickerman et al. [26].

2.2.1 Sputtering

When an ion beam reaches the sample, it generates a collision cascade in the material. Sputtering starts to occur with primary particle energies of about 20 to 40 eV and maximizes within the energy range of 5 to 50 keV. Several models are used to describe it, while molecular dynamics simulations are the most used these days.
The sputtering yield corresponds to the ratio between the number of emitted atoms, neutral or ions, and the number of incident ions. It depends on the incident beam and the nature of the surface. Its typical value range from 10^{-1} to 10.

2.2.2 Ionization

The ionization mechanisms are complex and still not fully understood to this day. A fraction of the sputtered particles will be ionized, at or above to the surface, but the exact location is unknown. A compound M can ionize through several pathways. First, one of its electrons can be ejected, resulting in an ion M^+. Proton exchange can also occur for acids and bases, which gives $(M+H)^+$ or $(M-H)^-$ ions. When compounds like Na or K are present in the matrix, cationisations such as $(M+Na)^+$ are favored.

2.2.3 Signal intensity

Let I_p be the primary particle current [C/s], y_m the sputtering yield, $\alpha^{\pm}$ the ionization probability to positive/negative ions, θ_m the fractional concentration of species m at the surface, and η the transmission of the spectrometer. The secondary ion current of m is then

$$I_m = I_p y_m \alpha^{\pm} \theta_m \eta \text{ [C/s]}. \tag{2.3}$$

$\alpha^{\pm}$ is strongly influenced by matrix effect, i.e. the strong dependence of the measured ion yields on the molecular environment. Consequently, the signal intensity for a given compounds does not reflect its exact quantity in the sample, but is significantly dependant on the ionization process. ToF-SIMS is thus only semi-quantitative. Proving that a compound is not in a sample can be challenging since its non-detection could be due to its lack of ionization rather than its absence.

2.3 Analysis modes

One of the advantages of this technique lies in its different modes of analysis, offering a wide variety of information. The four of them are represented in Figure 2.2 and detailed hereafter.
When the fluence exceeds 10^{13} ions/cm^2, SIMS has the ability to perform more in-depth investigations. This threshold, referred to as the static limit, serves as a demarcation point between static SIMS (S-SIMS), which operates below the static limit, and dynamic SIMS (D-SIMS), which operates above it. S-SIMS is thus useful to analyse surfaces, while D-SIMS allows depth profiling and 3D analysis, at the cost of a greater degradation of the sample due to erosion.

Mass spectrometry is the first and most used analysis mode, which allows to chemically characterize the surface. Mass spectra for positive and negative ions

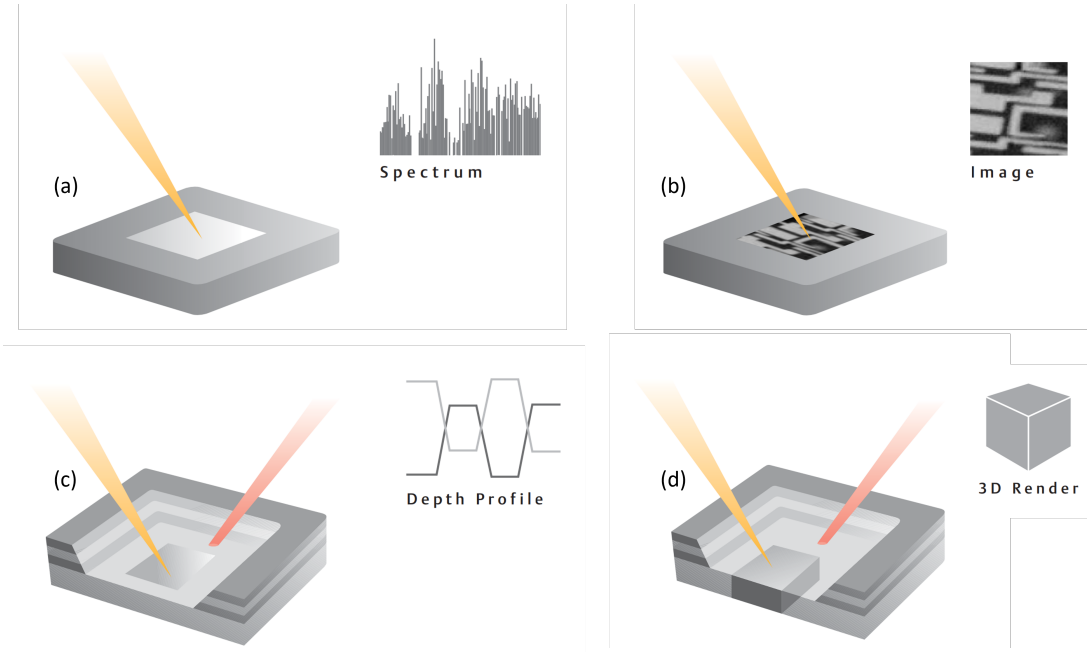

Figure 2.2: Schematic view of the four modes available in ToF-SIMS. The sample is represented in grayscale, the analysis ion beam in yellow, and the sputter ion beam in red. (a) Mass spectrometry. (b) Chemical imaging. (c) Depth profiling. (d) 3D rendering. Figure adapted from [29].

are provided during two separate analyses with appropriate parameters, following LMIG or GCIB scans [23]. Mass calibration of the spectrum is required to identify the detected compounds.

To generate chemical images of a surface, the instrument scans an area and captures the chemical composition at each point of beam incidence. Images can then be constructed using selected peaks and their corresponding relative intensities. Additionally, specific regions of interest (ROI) within an image can be chosen to obtain spectra specific to those areas.

LMIG and GCIB can be used in concert to provide depth profiles. LMIG analyses the surface and establishes its chemical composition, then GCIB etches the sample to reach a lower layer. LMIG performs another analysis on this new depth, and so on. Since this mode involves an etching GCIB source, it is considered as a D-SIMS technique.

Finally, volume analysis is possible in D-SIMS by combining the last two techniques. This mode allows parallel mass detection, as well as high depth and image resolutions [29]. An image of the surface is taken by the LMIG beam, then GCIB comes into play and reaches a lower depth on which further images will be taken. However, combining high lateral resolution images with depth profiling to achieve 3D image reconstruction is very time-consuming.

2.3.1 Delayed extraction

Delayed extraction (DE) is a technique used to improve the mass resolution and/or the lateral resolution of the analysis. It was initially employed in MALDI (matrix-assisted laser desorption/ionization) and has since been extended to ToF-SIMS. In ToF-SIMS, the secondary ions are usually accelerated and fly directly into the mass spectrometer's detector, having different masses and energies. The wide range of kinetic energies that they can have induce that while they are all accelerated into the mass spectrometer's detector simultaneously, they arrive at different times, which broadens the peaks.
DE constists of postponing the acceleration voltage, so that the secondary ions with higher kinetic energies will move further towards the detector during the delay and the ones with lower energies will remain closer to the surface. They will thus undergo a greater acceleration, allowing them to catch up with the higher-energy ions. As a result, the kinetic energy range is compensated, and all ions will reach the detector at the same time [30].

2.4 Applications

2.4.1 Benefits

This technique offers high lateral ($\sim$100 nm) and depth ($\sim$5 nm) resolutions, as well as a high surface sensitivity ($\sim$1 nm in the best case scenario) [25]. It also allows the parallel detection of both organic and inorganic ions, which is very useful in several fields such as cultural heritage.

2.4.2 Limitations

The first drawback of ToF-SIMS is its inability to provide quantitative information due to matrix effect. Data treatment can also be complex and tedious, and fragmentation of molecular ions often occurs, making it even more difficult to interpret the results. The samples must also be vacuum-compatible and may undergo vacuum degradation, or micro-damage due to the ion beams. Nonetheless, the ion beams used in ToF-SIMS typically cause minimal damage to a small portion of the sample, making it possible to reuse the sample for subsequent analyses, provided it is of sufficient size. Alternatively, if necessary, polishing the analysed surface might be adequate to achieve further analysis.

2.4.3 Utility in cultural heritage

ToF-SIMS has already been used for various cultural-related purposes, including pigment analysis [31] and chemical characterization and imaging of materials present in historical paintings [18, 32–38].

H. Lebrun [1] has also used ToF-SIMS to study the formation of oxalates and metallic soaps in oil paintings from the Southern Netherlands during the XVth to XVIIth centuries. The first part of his study examined pure powders of metal oxalates and soaps (azelate, palmitate and stearate) for Ca, Cu, Co, K, Pb and Zn, to serve as reference signatures for analyzing more complex samples. Concerning the oxalates powders, the detection of PbOx was the more successful, followed by CuOx and ZnOx, with much less conclusive results for calcium oxalate.

In the next phase, the technique was applied to mixtures of these compounds with linseed oil in mock-ups. The colocalization of lead and stearic acids, but also of lead stearates and oxalates, has been clearly observed in certain distinct zones of mock-ups. It indicates that oxalates are derived from stearates and originate from pigment-binder interaction.

He also emphasized that the signal intensities in historical cross-sections are notably lower than those in mock-ups for the compounds of interest. This difference could be attributed to their reduced concentration within historical samples, where a more diverse range of compounds is present. Furthermore, this detection of a greater variety of elements also results in interference within the ToF-SIMS spectra of the cross-sections. Some of these elements appear at masses similar to those of the components of interest, leading to complexities in distinguishing their peaks and affecting the accuracy of their mappings. There were many samples for which no conclusive observations were obtained, possibly due to the matrix effects of the binder.

Still, as illustrated in Figure 2.3, the analysis of a sample from the *Adoration of the Mystic Lamb* (by Jan and Hubert Van Eyck) confirmed the presence of copper oxalates in lower layers, as found in ATR-µFTIR, which is promising for this project.

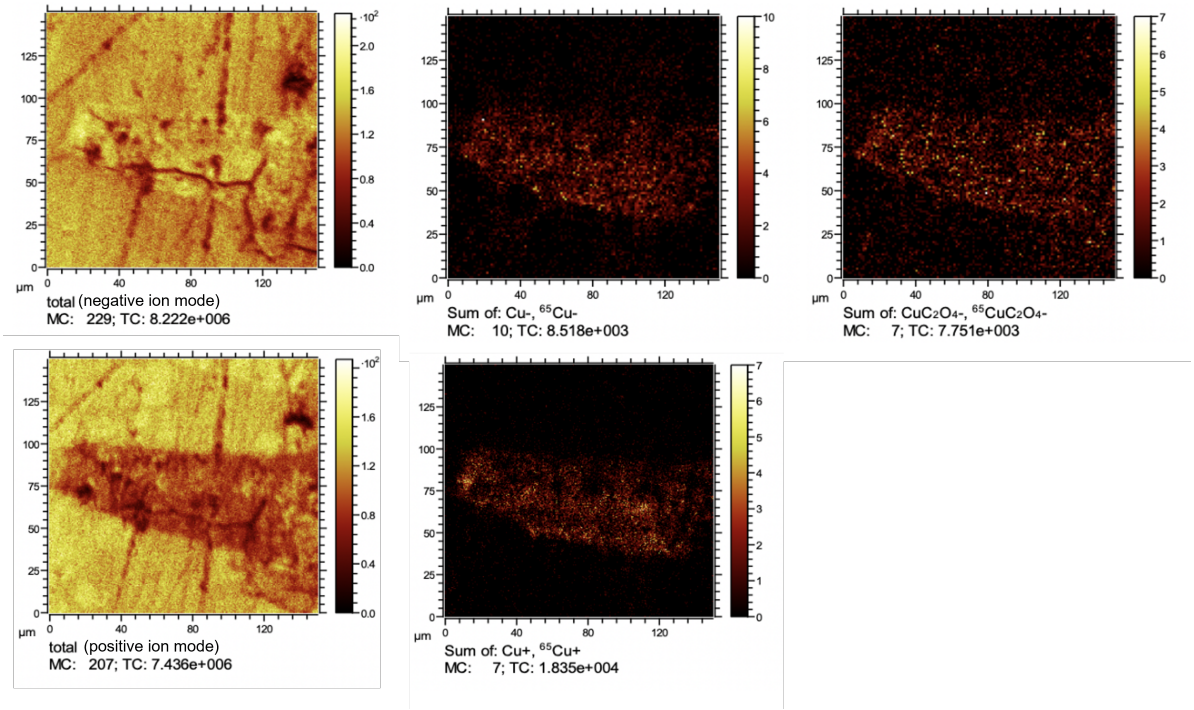

Figure 2.3: ToF-SIMS ion images of copper oxalate-related compounds in cross-section C91-123 obtained in H. Lebrun's work [1].

Lebrun encouraged extensive analyses of numerous additional historical samples to enable more comprehensive comparisons and enhance the likelihood of detecting certain compounds [1], which is one of the objectives of this work.
However, there is no scientific report demonstrating the detection of calcium oxalate using ToF-SIMS, even when its presence is attested by other techniques such as ATR-µFTIR or synchrotron radiation X-Ray powder diffraction (SR-XRPD). Usually, it is deduced by the presence of CaOx fragments in the absence of the detection of whole molecular ions [18, 38–42].

Chapter 3

XPS: Role and working principle

X-ray photoelectron spectroscopy (XPS for short, sometimes called ESCA for electron spectrometry for chemical analysis) is a quantitative and highly surface-sensitive technique. In this work, XPS was used for a more theoretical study aiming to characterize the powdered metal oxalates of interest. The objective was to better understand several of their properties such as the chemical state and the electronic structure of the atoms. As a matter of fact, reference spectra are needed for future research on the subject.

3.1 Instrumentation and operation

Figure 3.1 shows an XPS instrument operation scheme. The analysis takes place under ultra-high vacuum at typically 10^{-8}-10^{-10} mbar to ensure a sufficiently high signal intensity and low background noise level for satisfactory analysis. A higher pressure would result in too much scattering of ejected low-energy photoelectrons by the gas molecules, as well as too much contamination of the surface. Nonetheless, near-ambient pressure XPS is currently feasible, but it is not relevant in this context as we do not possess the necessary equipment for its implementation. The analysis chamber must also be magnetically shielded, as even weak magnetic fields such as that of the Earth can influence the path of the signal electrons [44].

The X-Ray (XR) source consists of a photon beam induced by the impact of high-energy electrons on a metal anode. Often, and as is the case in this work [45], the anode is made in aluminium, although magnesium is a commonly used alternative. When characteristic Al Kα X-rays are emitted, the energy is $h\nu = 1486.6$ eV, where h is Planck's constant and ν the frequency of the photon. Since this energy is lower than 5 keV, the emission is considered as "soft X-rays". As opposed to hard

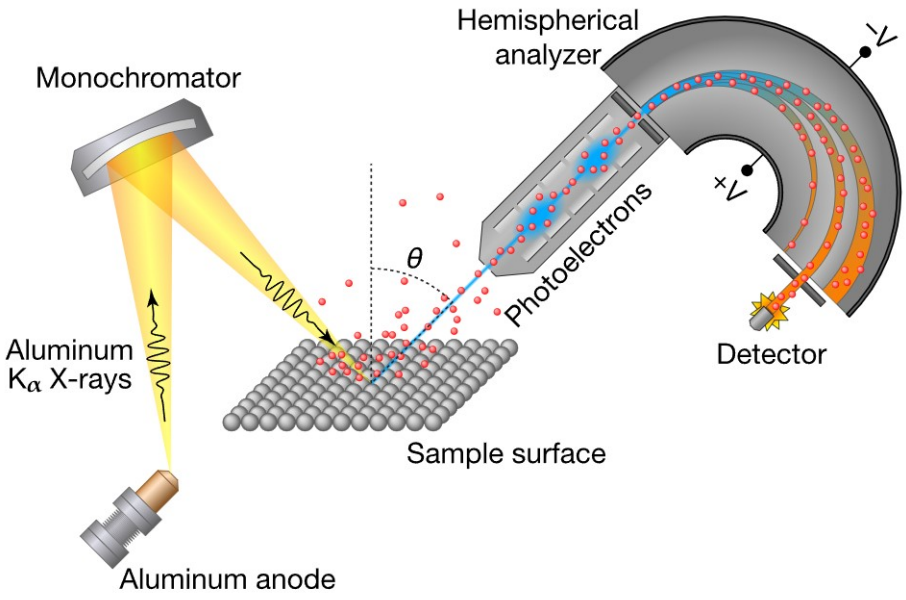

Figure 3.1: Schematic view of an XPS instrument [43].

XR that have higher energies, this kind of X-radiation has a narrower line width and penetrates less deeply into materials. The natural linewidth of the source is a limiting factor for achieving high spectral resolution. Due to the spin-orbit coupling of $2p_{3/2}$ and $2p_{1/2}$ levels (see subsection 3.3.5), Kα rays actually generate two spectral lines, called Kα_1 and Kα_2. For aluminium, they are separated by $\Delta E = 0.85$ eV, which broadens the resulting peak Kα, since it is the sum of the two. However, a crystal monochromator can significantly narrow the peak. Therefore, using a monochromatic source is beneficial in obtaining XPS spectra with improved spectral resolution, even if it comes at the cost of reduced X-ray intensity [44, 46].

According to the photoelectric effect, electrons are emitted from the surface of the sample when X-rays strike it. The basic principles behind this phenomenon are detailed in subsection 3.2.1. XPS can be performed on insulating samples, although similarly as in ToF-SIMS, charge compensation is required in this case.

These photoelectrons then pass through a retarding field and an extraction lenses to reach an energy analyzer. In the case of this work, it is a hemispherical analyzer. It can be a portion of a hemisphere or a complete one. This second option avoids electric field distortions due to the edges of the hemispheric sector, which improves electron transmission. As depicted in Figure 3.1, a hemispherical energy analyzer consists of two concentric hemispherical electrodes to which specific potentials are applied. The median potential is called the pass energy. The lower this energy, the better the resolution.

The electrons enter and exit the analyzer by narrow slits to minimize their angular dispersion [44, 47].

By recording the number of electrons detected as a function of their kinetic energy for the different energy intervals, one obtains a complete spectrum. Once the electrons of desired energies have reached the detector, the spectra will be captured, making the data available for processing.

3.2 Physical principles

3.2.1 Photoelectric effect

XPS is based on the photoelectric effect, which designates the phenomenon during which photoelectrons are ejected from a material, following its exposure to photons. Here, a soft XR photon of energy $h\nu$ strikes the sample. The atom that absorbs this photon emits a core electron at a certain kinetic energy. The basic equation governing the XPS principle is

$$E_B = h\nu - E_K - \Phi, \tag{3.1}$$

where E_B is the binding energy of the emitted photoelectron, E_K its measured kinetic energy, and Φ the work function of the spectrometer. Unlike E_K, E_B is specific to the atom. Therefore, a binding energy scale is generally used to represent the spectrum (except for Auger spectra) and perform its analysis [44, 46–48].

3.2.2 Core-hole relaxation

After the ejection of a core electron by photoelectric effect, two competitive relaxation phenomena can occur. The first one is XR fluorescence and the second consists in the emission of an Auger electron, as depicted in Figure 3.2. Their relative probabilities depend on the atomic number of the element and the specific electron shell. The higher this number, the more likely fluorescence and vice versa. Both processes begin with the neutralization of the core hole by an electron of a higher level. Their difference lies in the way the energy of this transition is evacuated from the system. In the case of fluorescence, the atom emits an XR fluorescence photon. In the other instance, more important in the case of XPS since photons are not detected, another electron, called Auger electron, is ejected [49]. These electrons also generate peaks that are sometimes useful to the analysis, as explained in subsection 3.3.4.

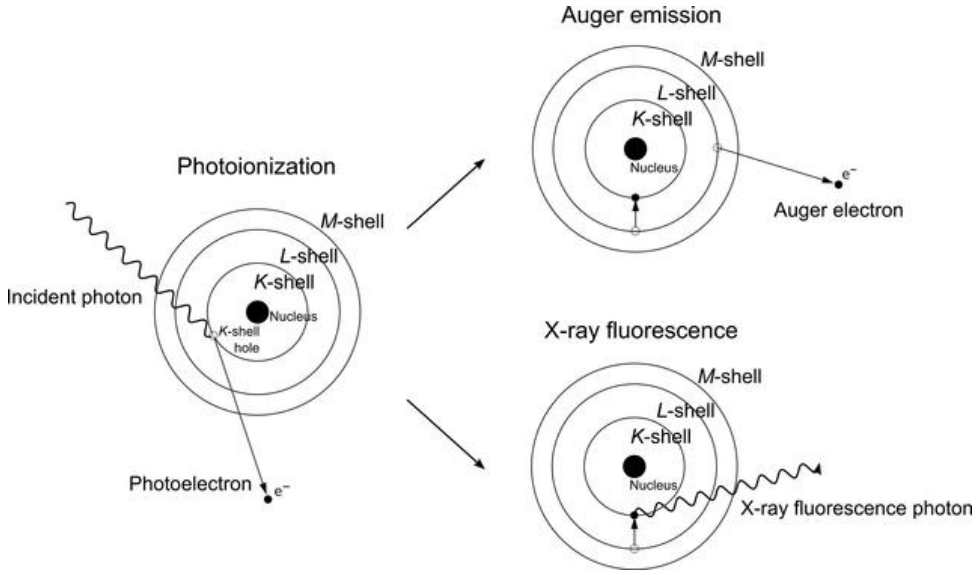

Figure 3.2: Competition between the two core-hole neutralisation processes. After the photoionization, either Auger emission or XR fluoresence may happen [49].

3.2.3 Information depth

XPS is a very surface sensitive technique. The intensity of the measured signal decreases exponentially with the depth from which the photoelectron comes, due to the inelastic collisions of the electrons inside the material. The deeper the photoelectron comes from, the more kinetic energy it loses on the way and the less chance it has to escape from the surface. If it does, its energy is altered and the photoelectron is counted in the background of the spectrum.
The measured signal of photoelectrons originating from the depth z, noted $I(z)$, can be computed as follows:

$$I(z) = I_0 \exp\left(\frac{-z}{\lambda \sin\theta}\right), \tag{3.2}$$

where I_0 is the non-attenuated surface signal, λ the inelastic mean free path (IMFP), and θ the take-off angle of the electrons relative to the surface as they travel toward the analyzer. λ designates the average distance traveled between two electronic inelastic scattering events, which is typically a few nanometers. It is experimentally determined as a function of the electron kinetic energy E_K, following the empirical universal curve in Figure 3.3 and the equation

$$\lambda = \frac{538}{E^2}a + 0.41a(aE_K)^{\frac{1}{2}}, \tag{3.3}$$

where a is the atomic size in nm. The IMFP increases as the kinetic energy of the

photoelectron increases above a minimum located around $E_K \sim$ 50-100 eV.

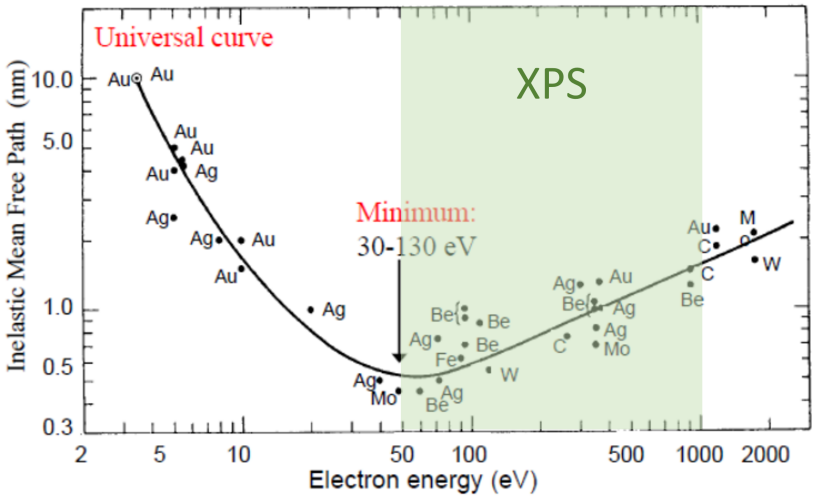

Figure 3.3: Universal curve describing the variation of the IMFP in function of the electron energy [50]. The energy range obtained in XPS is highlighted [25].

One way to assess the surface sensitivity of XPS is to look at the information depth. It is defined so that 95% of the perceived signal comes from the region between it and the surface, and is equal to 3λ [51].

3.3 Spectrum characteristics

To perform data processing consciously and apply it to metal oxalates, a thorough understanding of spectrum characteristics is essential.

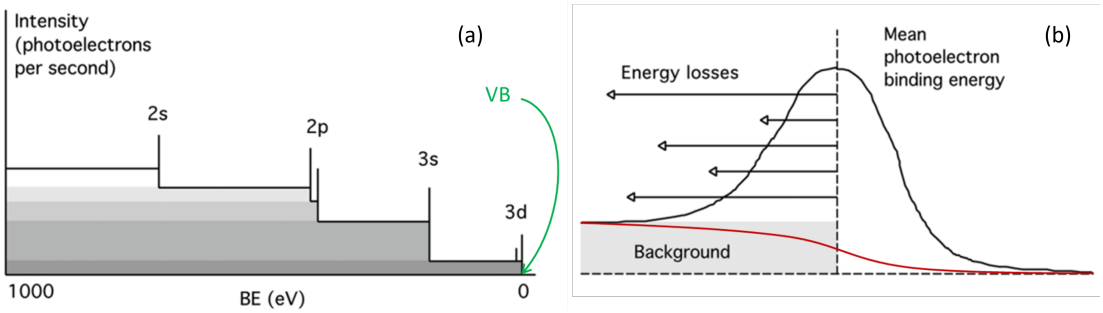

Figure 3.4: (a) Typical aspect of an XPS spectrum. (b) Typical shape of an XPS core-level peak. Figure adapted from [25].

3.3.1 General shape

The general aspect of an XPS spectrum is shown in Figure 3.4 (a). As indicated in green, one finds the valence band (VB) spectrum at positive binding energies

near zero. From then on, when going to higher binding energies, the background is increasing after each core-level peak. This is caused by electrons of the main peak that have lost energy through inelastic collisions.
Figure 3.4 (b) is more focused on the typical shape of a peak. Considering the background of the spectrum, clear peak boundaries must be defined to allow for decent quantitative analysis. A Shirley-type baseline (red curve on the figure) is often used for background subtraction, due to its ease of use and satisfying accuracy. Kinetic energy losses, detailed in subsection 3.3.6, induce structures shifted to the left with regards to the core-level peak.

3.3.2 Chemical shift

The specific amount of energy required to release a photoelectron is influenced by the charge localized on the atom, which depends on the ligands it is connected to (electronegativity effect) [52]. It allows the differentiation of non-equivalent atoms, i.e. the same chemical element but in other configurations or molecules. Therefore, the chemical shift provides information about the chemical bonds in addition to the elements. A higher oxidation state leads to fewer valence electrons and thus, according to the screening effect, a higher E_B for the core electrons and vice versa.

3.3.3 Valence band

In XPS, it is possible to record the valence spectrum of a sample. Obviously, it is only visible at very low binding energies, i.e. between 0 and about 30 eV. Given the very low photoelectric cross-section of valence electrons, valence peaks are much weaker than the core level peaks, and an excellent resolution is required to get useful information from it.
Energy distribution of the valence spectrum directly portrays the density of occupied states in the VB and may provide chemical bonding information [44, 46, 48].

3.3.4 Auger peaks

As explained in subsection 3.2.2, Auger relaxation may occur after the photoelectric process. When it is the case, Auger structures appear in the XPS spectrum, as shown in Figure 3.5 (b). These peaks are independent of the photon energy. In some compounds, the differentiation between different oxidation states is really tedious because of too small chemical shifts. In these cases, Auger features involving VB electrons can be useful thanks to their usually larger chemical shifts. Usually, a kinetic energy scale is used for this task.

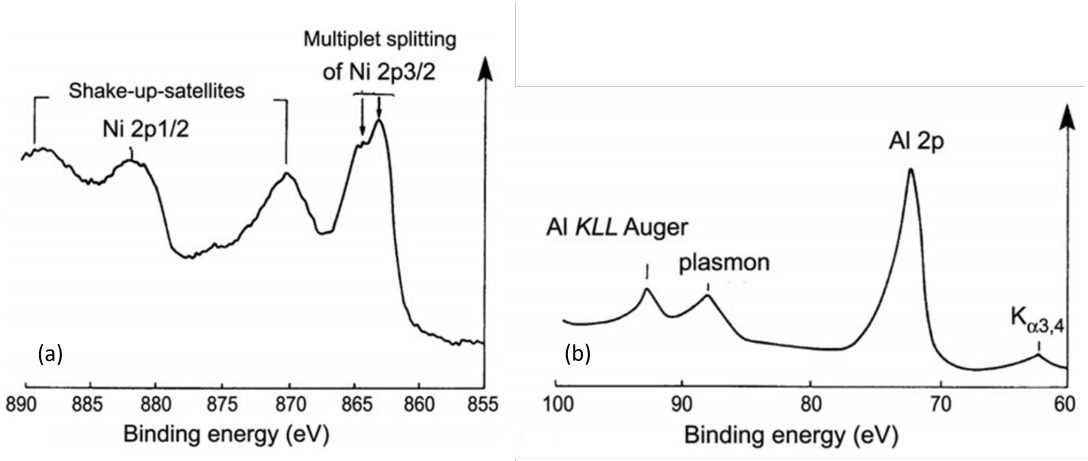

Figure 3.5: Energy loss in XPS spectra. (a) Intrinsic loss: Ni 2p shake-up satellites and multiplet splitting in NiO. One can also see the two peaks resulting from the SOS of Ni $2p_{1/2}$ and Ni $2p_{3/2}$. (b) Extrinsic loss: Al plasmon peak in pure aluminium. This graph also displays core-hole and Auger peaks. Figure adapted from [46].

The modified Auger parameter corresponds to the sum of the binding energy of the core level peak and the kinetic energy of the Auger line and is expressed as α' [52].

3.3.5 Spin-orbit splitting (SOS)

The coupling between the electron's intrinsic angular momentum (spin), and the angular momentum associated with its orbital motion around the nucleus (orbit) results in a doubling of the associated line. The quantum numbers associated with these quantities are respectively $s = \pm\frac{1}{2}$ for positive and negative spins and $l =$ 0, 1, 2, 3 for s, p, d and f orbitals. Taking into account these two contributions leads to the total angular momentum quantum number $j = |l \pm s|$. Apart from s orbitals where $l = 0$, there are then two possible j values. m_j, the secondary total angular momentum quantum number that takes all the values by steps of 1 between $-j$ and j, is thus $2j + 1$ times degenerate. It is noteworthy that the ratio of the areas of the two peaks resulting from the SOS corresponds to the ratio of the degenerations. The peak with the lower binding energy and the larger area is always the one with the higher j value, as shown in Figure 3.5 (a). Figure 3.6 illustrates the different cases according to the orbitals [25, 46].

3.3.6 Energy loss

Among the features induced by intrinsic kinetic energy loss, shake-up satellite peaks can appear when a photoelectron interacts with a valence electron and excites it to

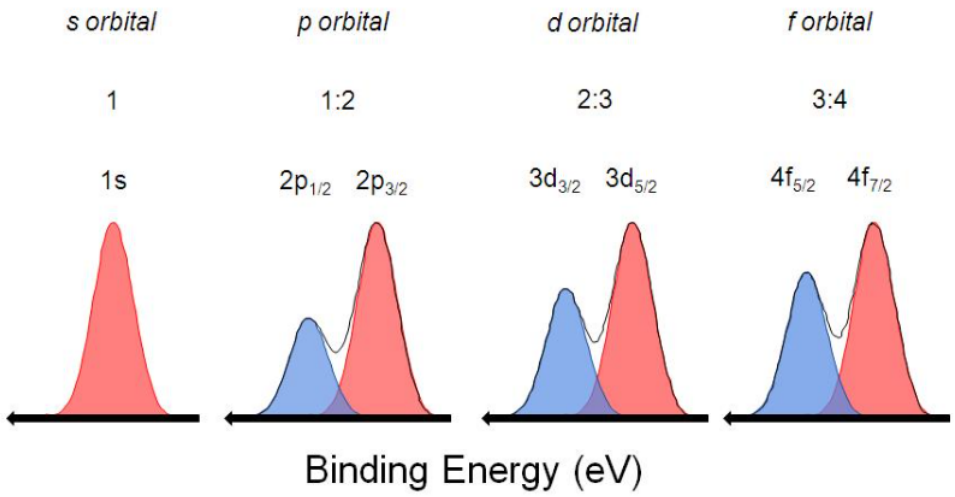

Figure 3.6: SOS for s, p, d and f orbitals. The ratio between the two peaks is shown for each case. For instance, the ratio between the $2p_{1/2}$ and $2p_{3/2}$ peak areas is to 1:2 because $2 \cdot 1/2 + 1 = 2$ and $2 \cdot 3/2 + 1 = 4$, which gives a ratio of 2 to 4, or 1:2 [53].

a higher energy level. Satellite structures appear broad because of the broad and featureless density of states.
Multiplet splitting of a peak can occur if the analyzed compounds have unpaired electrons in their VB. Strong interactions between these and unpaired core electrons left alone after photoemission may lead to more than one final state, inducing several "sub-peaks", called multiplet structure [46]. This effect is actually used in XPS spectrum analysis, as it allows to differentiate similar materials.

On the other hand, an important source of extrinsic loss in metals consists in collective oscillations of conduction electrons, which are called plasmons. Plasmon loss is generally one of the main sources of energy loss for electrons in metal compounds. Plasmon-related structures appear as well-defined peaks at precise binding energies, but are generally featureless and not amenable to analysis. Depending on their shape and position, they may even disturb the interpretation of other peaks [44].

3.3.7 Quantitative interpretation

XPS is, indeed, a quantitative technique; however, the peak areas cannot be directly utilized for quantification purposes. The atomic fraction of the element i in a sample must be computed as

$$X_i = \frac{A_i/S_i}{\sum_{j=1}^{n} A_j/S_j}. \tag{3.4}$$

The term $A_{i(j)}$ refers to the area under the elemental peak of interest and $S_{i(j)}$ to its relative sensitivity factor.

$$S_i = \sigma_{ij}\lambda \tag{3.5}$$

where σ_{ij} is the photoionization cross-section of peak j from element i and λ is still the IMFP [47, 51].

3.4 Applications

3.4.1 Benefits

The strength of XPS lies in its low degradation and the information it provides, i.e. quantitative surface analysis and chemical information. It can also be performed on insulating samples, which is crucial in the context of this project.

3.4.2 Limitations

The photoionization cross-sections of hydrogen and helium are too small to allow their detection in XPS. In addition, although this technique is still very surface-sensitive, this sensitivity is strongly energy-dependent and often on the order of a small fraction of a percent, which hinders the detection of trace elements. Furthermore, the spatial resolution is limited by the difficulty of having a highly focused X-ray beam compared to ions or electrons. Data processing can also be tedious due to decomposition problems that can occur in complex spectra, sometimes making it impossible to distinguish between several nearby peaks [25].

3.4.3 Utility in cultural heritage

To date, the place of XPS in historical painting degradation research is less than that of ToF-SIMS. However, there exist several XPS studies on pure metal oxalates [54–56]. Transition metals such as cobalt, nickel, iron and copper oxalates have been frequently studied. However, to the best of our knowledge, there is still no XPS paper about metal oxalates in cultural heritage. Furthermore, there has been no systematic investigation conducted to date on CaOx, PbOx, and ZnOx, precisely the ones of interest in this field.

In particular, Chenakin's paper [56] studies the binding energies between the aforementioned transition metal cations and the oxalate anions, but examining the

binding energies of the MetOx associated with paintings could elucidate certain puzzling patterns found in historical artworks, as detailed in chapter 5.

Part II

Objectives

Chapter 4

Goals using ToF-SIMS

The primary objectives of this work were to employ Time-of-Flight Secondary Ion Mass Spectrometry to detect and localize copper oxalate within historical samples. The investigation focused on establishing a reliable method for identifying the presence of CuOx compounds, which are of significant interest due to their common presence in impaired paintings.
Similarly, the study aimed to identify and localize calcium oxalate species in the same kind of samples. Understanding the distribution and occurrence of CaOx is also crucial for gaining a comprehensive understanding of their potential impact on the paintings.
Ultimately, the study aims to evaluate the significance and implications of the ToF-SIMS technique. The assessment of its role in achieving the aforementioned objectives is aimed at determining its reliability and effectiveness in the detection of these specific compounds. Valuable insights into the strengths and limitations of ToF-SIMS for future applications in similar research endeavors can be gained through this evaluation.

Chapter 5

Goals using XPS

In the context of potential future XPS studies on historical samples or to gain a deeper understanding of the nature of common MetOx, the present research aims to investigate and characterize the XPS spectra of metal oxalate powders.
Unlike the study conducted using ToF-SIMS, which belongs to a relatively common type of research, there is no literature on metal oxalates within this context when it comes to XPS analysis. Therefore, conducting a theoretical and fundamental analysis of pure compounds becomes particularly important. This analysis could lay the groundwork for future historical sample examinations, for instance.

The data analysis and presentation of the results in chapter 9 heavily rely on the 2020 article by S. Chenakin et al., which focuses on characterizing transition metal oxalates in XPS [56]. Chenakin and his team conducted a comprehensive study of the XPS spectra of Mn, Fe, Co, Ni, and Cu oxalates, comparing a large number of parameters among these five species.
In Chenakin's study, an investigation was conducted into the binding energies between metal cations and oxalate anions. However, the metal oxalates analyzed in their research differ from those encountered in historical paintings.
Consequently, an exploration was undertaken to assess whether an approach to the binding energies of these painting-related metal oxalates could shed light on certain perplexing patterns observed in historical paintings. For example, despite hundred of analyses carried out across numerous cross-sections, the identified metal oxalates are exclusively limited to CaOx, CuOx, and ZnOx. The presence of PbOx, despite concentrated efforts to detect it, has never been established.
This problem cannot originate from its limit of detection by ATR-µFTIR, because the MetOx project demonstrated that CaOx, CuOx and ZnOx have almost the same limit of detection, from which they deduced that it does not depend on the oxalate type.

However, an alternative possibility is that the typical FTIR vibrations related to PbOx could be masked by those originating from CaOx or other compounds. Alternatively, it is plausible that PbOx is found in concentrations below the limit of detection.
Another potential explanation is that the binding energy between cations and anions in PbOx is too low, thereby facilitating cationic exchange. Over time, this could lead to the gradual disappearance of PbOx from the paintings, favoring compounds with higher binding energies such as CaOx, CuOx, or ZnOx.

In this master's thesis, the aim is to extract as much fundamental information as possible about the spectra of CaOx, CuOx, PbOx, and ZnOx and deepen the understanding of this kind of phenomena. However, due to the greater dissimilarity among these species compared to the transition metals analyzed by Chenakin, the dimension of comparison is reduced, as these species exhibit distinct spectral shapes.

Part III

Materials and methods

Chapter 6

ToF-SIMS

6.1 Samples

Within the framework of this study, eleven ToF-SIMS analyses were carried out, on a total of 7 historical cross-sections and one mock-up. All samples were provided by KIK-IRPA. During the MetOx project, research conducted using ATR-µFTIR (Bruker µFTIR Hyperion 3000 with a 150-micron Germanium tip) enabled the detection and spatial localization of metal oxalates in all of these samples.

Micrometric historical samples were obtained from chosen paintings using a scalpel and embedded in a resin (Technovit 2000® LC resin, Kulzer, Germany). They were polished until the desired depth was achieved to obtain analyzable cross-sections. In total, the analyzed samples originated from six distinct paintings, and one of those paintings produced two cross-sections (C101-040 A and B come from *The Seven Joys of Our Lady* by L. Blondeel). Details of all the cross-sections are provided in Table 6.1. All of them originate from oil paintings on wood panels from the Southern Netherlands and date from the fifteenth to the early seventeenth centuries. The paintings themselves and the collections they come from are presented in Appendix A.

The mock-up was realized at KIK-IRPA. It consists of a mixture of red lake and linseed oil (Standoil 73200, Kremer Pigmente, Germany). To produce CaOx, it was artificially aged in an aging chamber (Weiss Technic, Global UV tester model UV 200 RB/20DU type BAM) at the University of Antwerp for ten weeks. The aging conditions were the following: ultraviolet type A (31.5 ± 2.6 W/m^2) and visible (1250 ± 210 lux) radiations, 40°C and a relative humidity of 80% (dew point: 35.9°C). It was then stored and left to age naturally in the dark, at a temperature of 20°C and relative humidity of 50% for three years [22]. It is embedded in the

same resin as the historical cross-sections [1].

Table 6.1: Main information on the historical cross-sections analyzed in ToF-SIMS.

	Project	**Artist**	**Sample**
C17-085	*Pietà*	Petrus Christus	Dark green, robe
C21-053	*The resurrection of the Christ*	Peter Paul Rubens	Green, ground, left panel wing
C30-153	*Adam and Eve*	Master of the Mansi Magdalen	Green
C32-038	*The Holy Trinity*	Master of the Holy Blood	Green
C88-145	*Deploration of Christ*	Jacob Jordaens	Red, Saint John's robe
C101-040	*The Seven Joys of Our Lady*	Lanceloot Blondeel	Dark red, Virgin and Child scene (center)

Optical microscopy (OM) was performed at KIK-IRPA on each sample using an Axio Imager M1 optical microscope equipped with a CCD Deltapix camera (Zeiss, Oberkochen, Germany). This was done under white polarized (POL) light as well as ultraviolet (UV) radiation with an excitation band-pass filter ranging from 390 to 420 nm and magnification up to 500×.

The ToF-SIMS analyses performed in this work are based on previous results obtained during the MetOx project using ATR-µFTIR. This technique has allowed to produce mappings in which the spatial distribution of CaOx and CuOx is observed in the different strata. As Lebrun suggested in the perspectives of his work, a comparison of the mappings of these two techniques would help to certify the presence of the compounds of interest. An example is displayed in Figure 6.1. In each mapping, false-colour scale ranges from deep blue to pink white, indicating the absence or the highest relative intensity of the visualized vibration, respectively (see Figure 1.4). The red squares show the area analyzed using this technique.

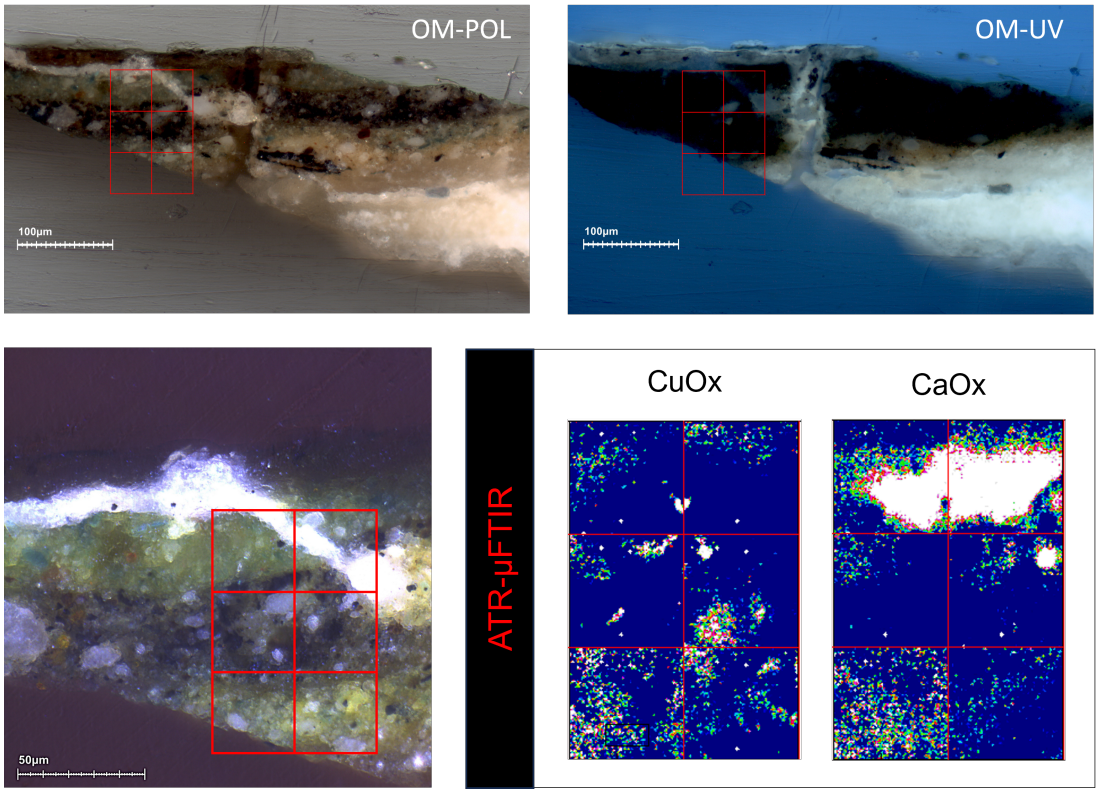

Figure 6.1: POL and UV microphotographs and ATR-µFTIR mappings showing the spatial distribution of CuOx (1375-1355 cm^{-1}) CaOx (1336-1296 cm^{-1}) in cross-section C21-053. The red squares in the OM images represent respectively the analysis areas in ATR-µFTIR.

ATR-µFTIR analyses were performed on a Bruker Vertex 70 FTIR coupled to a Bruker Hyperion 3000 FTIR microscope equipped with a 250 µm diameter germanium ATR tip.

6.2 Experimental parameters and protocol

The ions on which the research was focused were chosen based on Lebrun's work [1]. He demonstrated the difficulties of obtaining an oxalate peak ($HC_2O_4^-$) in historical cross-sections, which had already been deduced from previous studies, notably within the scope of the MetOx project [22]. He did however detect it in pure powdered samples, so it will still be consistently examined to see if his results (i.e. the low intensity and absences of a well-defined oxalate peak and localization in cross-sections) are confirmed in our work. However, in pure powdered metal oxalate samples, he successfully detected the metal ions but much less the entire metal oxalate complex, especially for CaOx. Interestingly, the opposite was true

when analyzing historical cross-sections, where CuOx was detected more easily than $HC_2O_4^-$.
Moreover, following his advice, both negative and positive polarity images are acquired. Even if the main oxalate-related compounds are observed in negative polarity (anions $HC_2O_4^-$, $CuC_2O_4^-$ and $CaC_2O_4^-$), it is important to correlate their localizations with the metal cations of interest, which appear in positive ion mode Cu^+, $^{65}Cu^+$ and Ca^+. Copper ions also appear in negative ion mode, but verifying their counterparts in the positive polarity allows to ensure that it is, indeed, copper, and to validate the results.
To demonstrate the presence of copper oxalate in a cross-section, the ions presented in Table 6.2 and their localizations were examined.

Table 6.2: Investigated compounds for the search of copper oxalate.

Negative ion mode		**Positive ion mode**	
m/z	Formula	m/z	Formula
63	Cu^-	63	Cu^+
65	$^{65}Cu^-$	65	$^{65}Cu^+$
123	$CuCO_3^-$		
125	$^{65}CuCO_3^-$		
151	$CuC_2O_4^-$		
153	$^{65}CuC_2O_4^-$		
89	$HC_2O_4^-$		

Similarly, the ions presented in Table 6.3 and their localizations were examined to demonstrate the presence of calcium oxalate in a cross-section.

Table 6.3: Investigated compounds for the search of calcium oxalate.

Negative ion mode		**Positive ion mode**	
m/z	Formula	m/z	Formula
128	$CaC_2O_4^-$	40	Ca^+
89	$HC_2O_4^-$	57	$CaOH^+$

Analyses were carried out on an ION-TOF V instrument (IONTOF GmbH, Münster, Germany).
In the first place, the surface is briefly cleaned with Ar_{3000}^+ at 5 nA. Right after, a depth profile is conducted to determine the optimal depth at which the signal for oxalate (more exactly its protonated ion $HC_2O_4^-$) and copper or calcium oxalate ions (respectively $CuC_2O_4^-$ and $CaC_2O_4^-$) is the highest. Given the worth of the historical samples and the frequent obligation to perform both the profile and the

analysis on the same area due to their small size, profiles are only performed in the negative polarity and stopped after a few seconds once the intensity ceases to increase. This aims to minimize damage to the analysis surface and maximize the chances of observing these ions. Complete profiles were however conducted in both polarities on the mock-up, as its larger size enabled the selection of a different area than the one being analyzed. These profiles are displayed in Appendix E and allow good visualization of the main species and their relative depth. After that, image acquisition can begin, alternating GCIB and LMIG.
The parameters used for the depth profiles and the images are listed Table 6.4.

Since the analyses are performed on insulating samples, did not dig very deep and that there was no need to do rapid analysis, non-interlaced mode [1, 57] was used in each analysis for prioritizing data quality, as the interlaced mode may lead to issues such as low signal intensity and compromised mass resolution.
Some parameters such as the primary ion doses, the LMIG currents and the reflector voltage vary depending on the analysis and the nature of the sample. The values presented in Table 6.4 give their order of magnitude. The number of scans in a profile also changes with the depth at which the signal of the desired compounds is maximal, but remains naturally way shorter than for the images.
Below each ToF-SIMS image, the chemical formulas of the counted ions are provided, along with their maximal count (MC) and total count (TC). The image color scale can thus be interpreted as ranging from black (count = 0) through various shades of red and yellow to white (count = MC). TC represents the sum of the counts of every pixel for the specified ion(s) [10].

The analysis areas are chosen based on ATR-µFTIR images indicating the presence of the species of interest. Data treatment was performed on the SurfaceLab analysis software. The spectra were calibrated using CH_3^+, $C_2H_5^+$, $C_3H_5^+$ and $C_4H_7^+$. Shift correction has been systematically applied to every analysis in both polarities.

Table 6.4: ToF-SIMS experimental parameters used for each acquisition.

Variable	**Setting**
Primary ion gun for sputtering	GCIB Ar_{3000}
GCIB energy	10 keV
GCIB current (profiles)	45 pA
GCIB current (images)	5 pA
Crater size	600 µm × 600 µm
Dose density of GCIB	Variable
Primary ion gun for analysis (profiles)	LMIG Bi_5^+
Primary ion gun for analysis (images)	LMIG Bi_3^{++}
LMIG energy (profiles)	30 keV
LMIG energy (images)	60 keV
LMIG mode (profiles)	High current bunched
LMIG mode (images)	Burst alignment
Analyzed area	200 µm × 200 µm
Dose density of LMIG	Variable
Raster mode	Random
Raster size (profiles)	128 by 128 pixels
Raster size (images)	1024 by 1024 pixels
Flood gun energy	20 eV
Reflector voltage	200-400 V
Cycle time (profiles)	200 µs
Cycle time (images)	100 µs
Total number of scans (profiles)	Variable
Total number of scans (images)	∼40

Delayed extraction has also been tested to improve mass-resolution on the mock-up, with an extraction delay of 0.89 µs.

Chapter 7

XPS

7.1 Samples

Experiments were performed on metal oxalate powders synthesized at KIK-IRPA using $K_2C_2O_4$ and metal nitrates. Four different metal oxalates were analyzed: CaOx, CuOx, PbOx and ZnOx. The powders were pressed uniformly inside cupules and placed in a carousel for analysis (see Appendix F).

7.2 Experimental parameters

Analyses were carried out on an SSX 100/206 spectrometer from Surface Science Instruments (USA). The source was a monochromatized and micro-focused Al Kα X-ray beam used at an operating power of 200 W (width of 800 $\times$ 800 µm). The instrument uses a hemispherical analyzer and performs automatic sample analysis [45]. It has a resolution of 0.1 eV. The core-level, Auger and VB spectra were acquired using a pass-energy of 50 eV and energy steps of 0.1 eV and the general surveys with a pass-energy of 150 eV and energy steps of 1 eV. A charge neutralization system employing an 8 eV operating flood gun has been used. Analyses have been performed on CaOx first, then PbOx, and finally ZnOx. However, since the survey spectrum for CuOx had not been recorded by the technician during this sequence, CuOx data comes from another analysis sequence performed a few months before, except for the VB spectra that was recorded in the other sequence. Spectra were recorded in the following order for each powder: C 1s, O 1s, Me, Auger lines, survey, VB, C 1s. The second occurrence of C 1s allows one to assess possible degradation or surface changes that might have occurred during analysis. They were calibrated using the reference value of 284.8 eV for the C 1s (C-C/C-H) peak [58]. Following the subtraction of a Shirley-

type background, the core-level spectra were decomposed using a curve-fitting approach that utilized mixed Gaussian-Lorentzian lines (with a 85% Gaussian and 15% Lorentzian composition). Data analysis was conducted using the CasaXPS software.

Part IV

Results and discussion

Chapter 8

Detection of calcium and copper oxalates using ToF-SIMS

8.1 Copper oxalate

8.1.1 Results

Copper oxalate has been successfully detected in two ToF-SIMS analyses, in cross-section C21-053 and in the left side of cross-section C30-153. ToF-SIMS ion images of the other analyses are displayed in Appendix C.
Figure 8.1 displays cross-section C21-053 and the long whitish crack that extends from its center to its left end. It probably appeared during polishing and let the resin and/or adjacent layers penetrate. According to the obtained ATR-µFTIR results, this sample has been used to investigate the presence of both calcium and copper oxalates using ToF-SIMS.
This figure also shows high and localized intensities for the main copper oxalate-related compounds Cu^+, Cu^-, $CuCO_3{}^-$ and fortunately $CuC_2O_4{}^-$, as well as the corresponding species with the ^{65}Cu isotope. They are concentrated in the paint layers, although they appear to be present in all of the cross-section to a lesser extent. The ATR-µFTIR images indicate a relatively disparate distribution of small CuOx clusters, which matches the diffuse shape observed in ToF-SIMS.

ToF-SIMS ion images in Figure 8.2 reveal that C30-153 contains a high concentration of copper ions along the entire length of its paint layer in both polarities. When examining $CuC_2O_4{}^-$, a slightly higher intensity than in the rest of the image is observed in this same zone. It is indeed consistent with the ATR-µFTIR mappings shown in the same figure, which also indicate the presence of CuOx in the top layer, especially at the extreme surface of the painting.

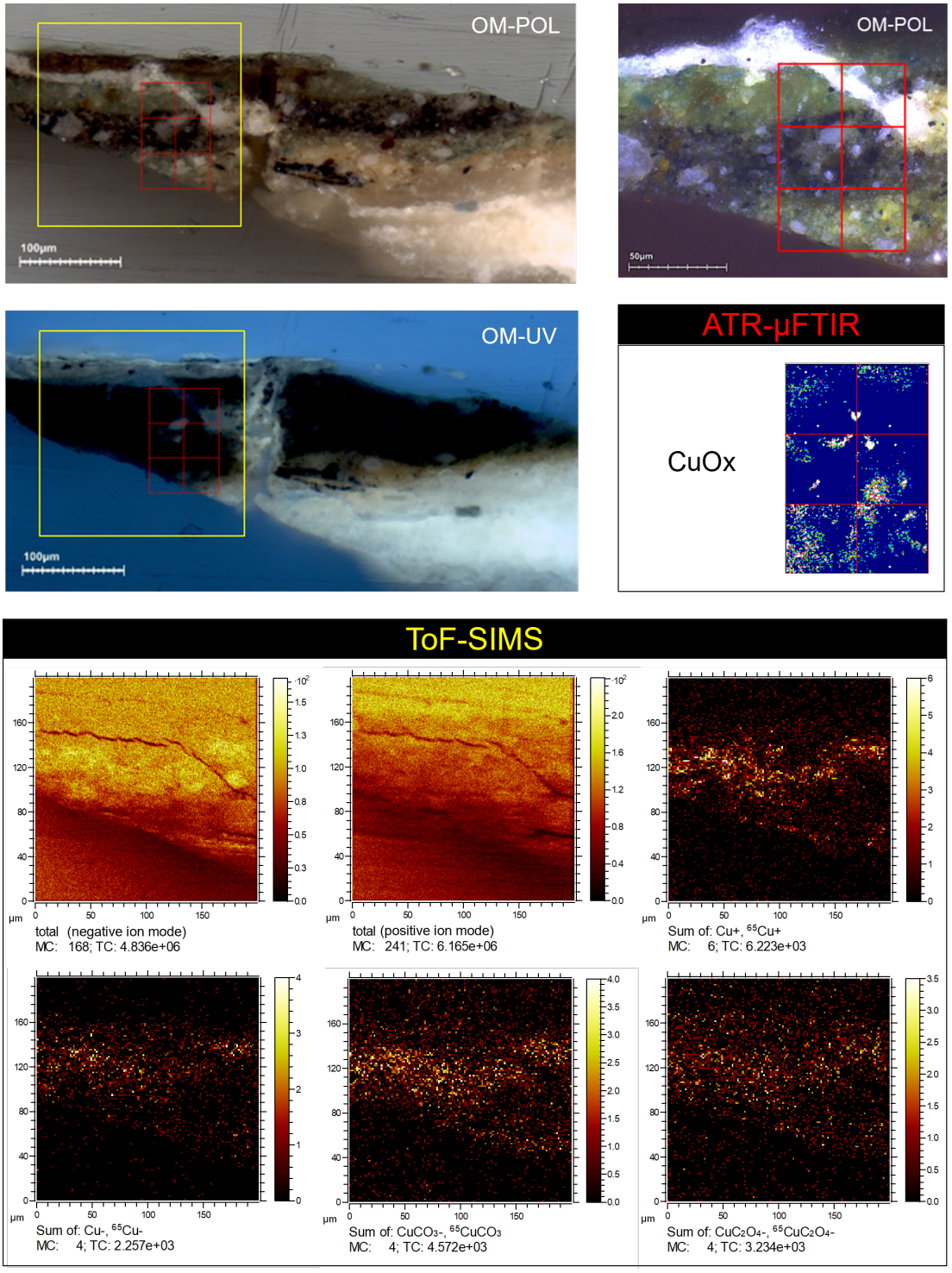

Figure 8.1: POL and UV microphotographs, ATR-µFTIR mappings showing the spatial distribution of CuOx (1375-1355 cm^{-1}), and ToF-SIMS ion images of CuOx-related compounds in cross-section C21-053. The red and yellow squares in the OM images represent respectively the analysis areas in ATR-µFTIR and ToF-SIMS.

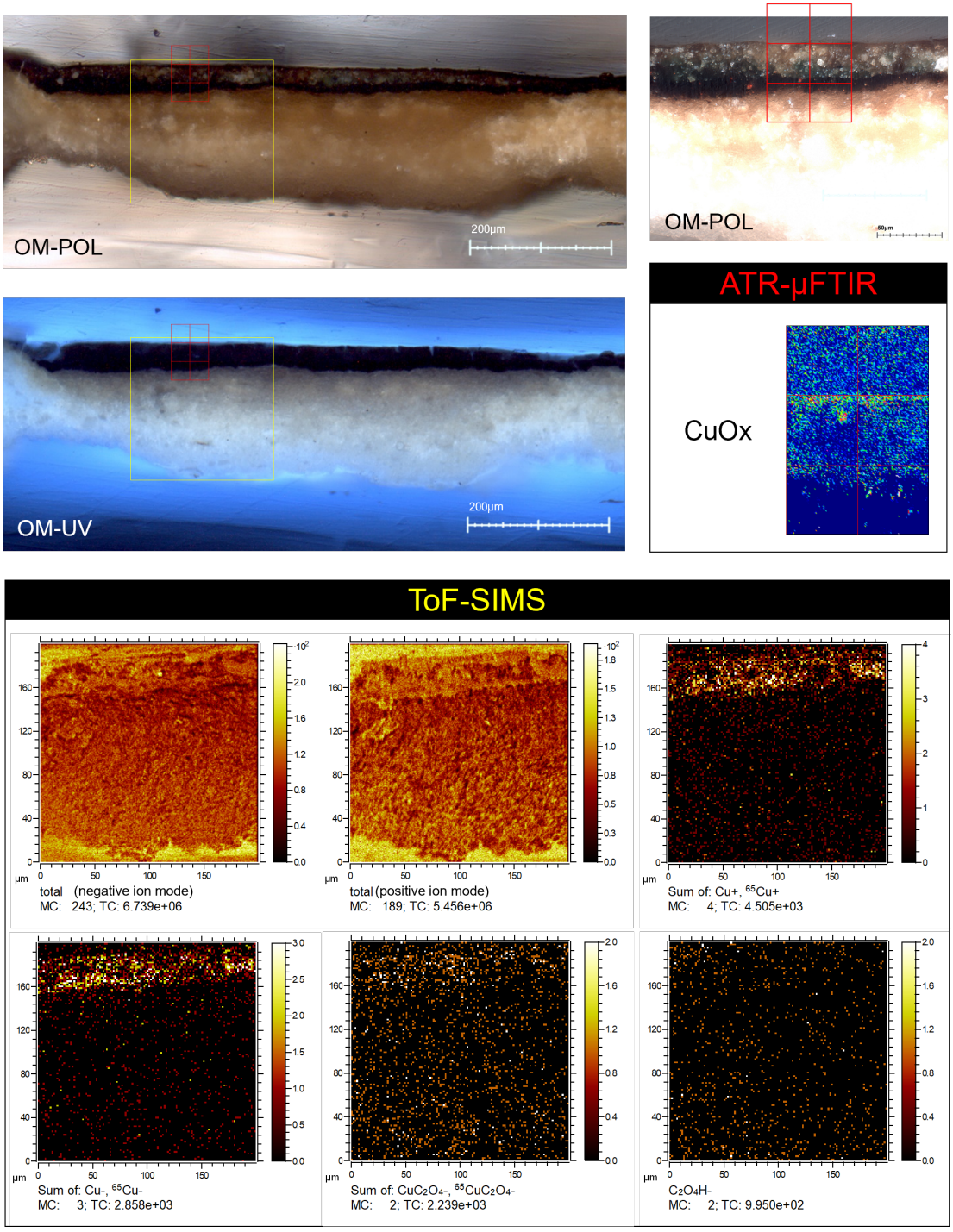

Figure 8.2: POL and UV microphotographs, ATR-µFTIR mappings showing the spatial distribution of CuOx (1375-1355 cm^{-1}), and ToF-SIMS ion images of CuOx-related compounds in the left part of cross-section C30-153. The red and yellow squares in the OM images represent respectively the analysis areas in ATR-µFTIR and ToF-SIMS.

8.1.2 Interpretation

The colocalization of various copper-containing ions, including the copper oxalate ion $CuC_2O_4^-$, suggests the presence of copper oxalate in cross-sections C21-053 and in the left side of C30-153. These satisfactory results are a first proof of the effectiveness of this analysis technique and method.
Concerning the oxalate ion $HC_2O_4^-$, its non-detection is not surprising given the results obtained by H. Lebrun [1]. He did not observe it in historical cross-sections, and barely in the mock-up and pure samples.
The presence of the copper carbonate ion $CuCO_3^-$ is characteristic of the presence of malachite, another green pigment used between the XVth and the XVIIth centuries, with the chemical formula $Cu_2CO_3(OH)_2$. This suggests that malachite was utilized in cross-section C21-053, either alone or mixed with verdigris. Malachite has also been observed to produce copper oxalate as a degradation product over time [59], but to a lesser extent than verdigris. The MetOx project [22] highlighted the fact that CuOx was found in malachite-containing layers in only ∼50% of the historical cross-sections they analyzed, and always in the presence of other copper-containing materials such as verdigris, preventing the conclusion of a direct correlation between malachite and CuOx. The malachite pigment has also been found to exhibit increased stability of the carbonato and/or hydroxo ligands surrounding the Cu (II) cation. Consequently, it displays reduced reactivity towards carboxylate ligand exchange. However, they observed copper oxalate in malachite-based mock-ups, which suggests that this pigment may still contribute to the generation of such metal oxalates under specific circumstances.

8.2 Calcium oxalate

8.2.1 Results

Samples C21-053, C30-153 (left and right), C17-083, and the mock-up showed traces of calcium oxalate. In every sample, $CaOH^-$ and $HC_2O_4^-$ intensities are very low, as shown in Figure 8.3, Figure 8.4, Figure 8.5 and Figure 8.6.
Cross-section C21-053 presents relatively high and localized ion intensities for the main calcium oxalate-related compounds Ca^+, $CaOH^+$, and $CaC_2O_4^-$.

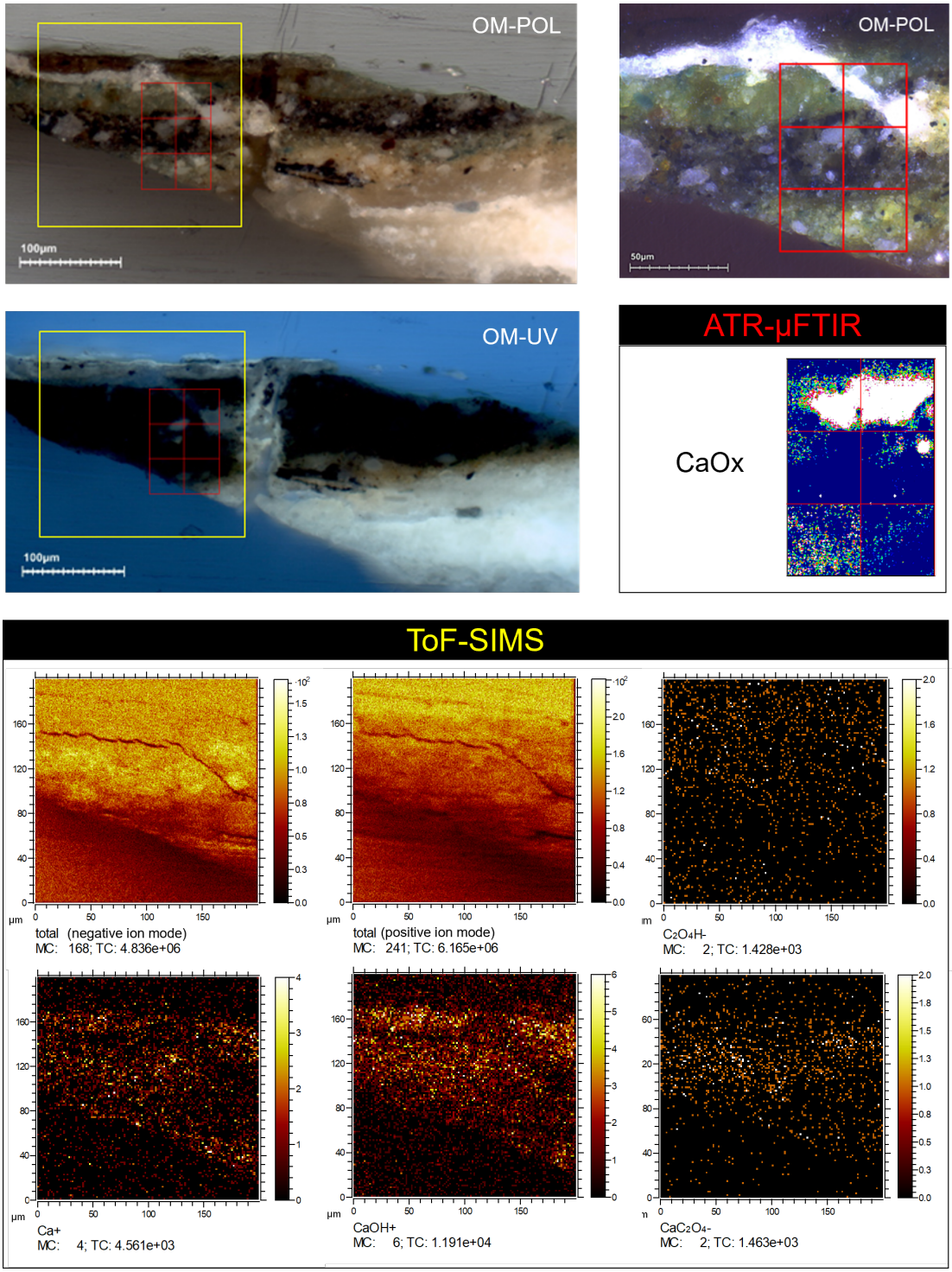

Figure 8.3: POL and UV microphotographs, ATR-µFTIR mappings showing the spatial distribution of CaOx (1336-1296 cm^{-1}), and ToF-SIMS ion images of CaOx-related compounds in cross-section C21-053. The red and yellow squares in the OM images represent respectively the analysis areas in ATR-µFTIR and ToF-SIMS.

Cross-section C21-053, represented in Figure 8.3, contains Ca^+, $CaOH^+$ and $CaC_2O_4^-$ ions in the same area. CaOx does not appear to be concentrated

primarily on the painting's outer surface. Instead, it is found within the paint layers, with a notable concentration in the light green layer located just below the crack. This observation aligns consistently with the ATR-µFTIR image.

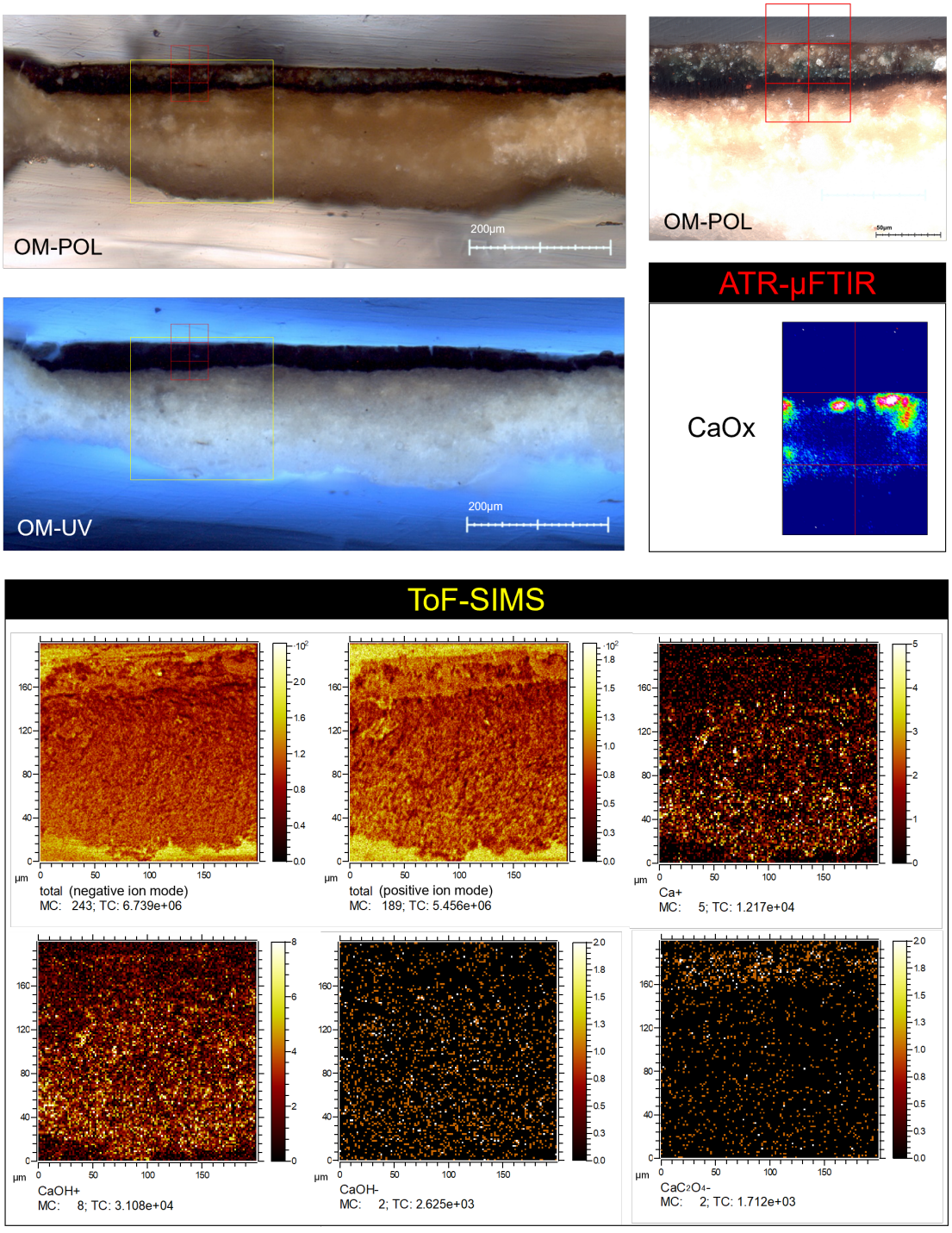

Figure 8.4: POL and UV microphotographs, ATR-µFTIR mappings showing the spatial distribution of CaOx (1336-1296 cm^{-1}), and ToF-SIMS ion images of CaOx-related compounds in the left part of cross-section C30-153. The red and yellow squares in the OM images represent respectively the analysis areas in ATR-µFTIR and ToF-SIMS.

Figure 8.4 presents the left part of cross-section C30-153. Calcium-containing ions Ca^+ and $CaOH^+$ are found, particularly in the preparation layer. Above, in the paint layers, calcium oxalate ion $CaC_2O_4^-$ is detected at the surface of the painting, as demonstrated in ATR-µFTIR.

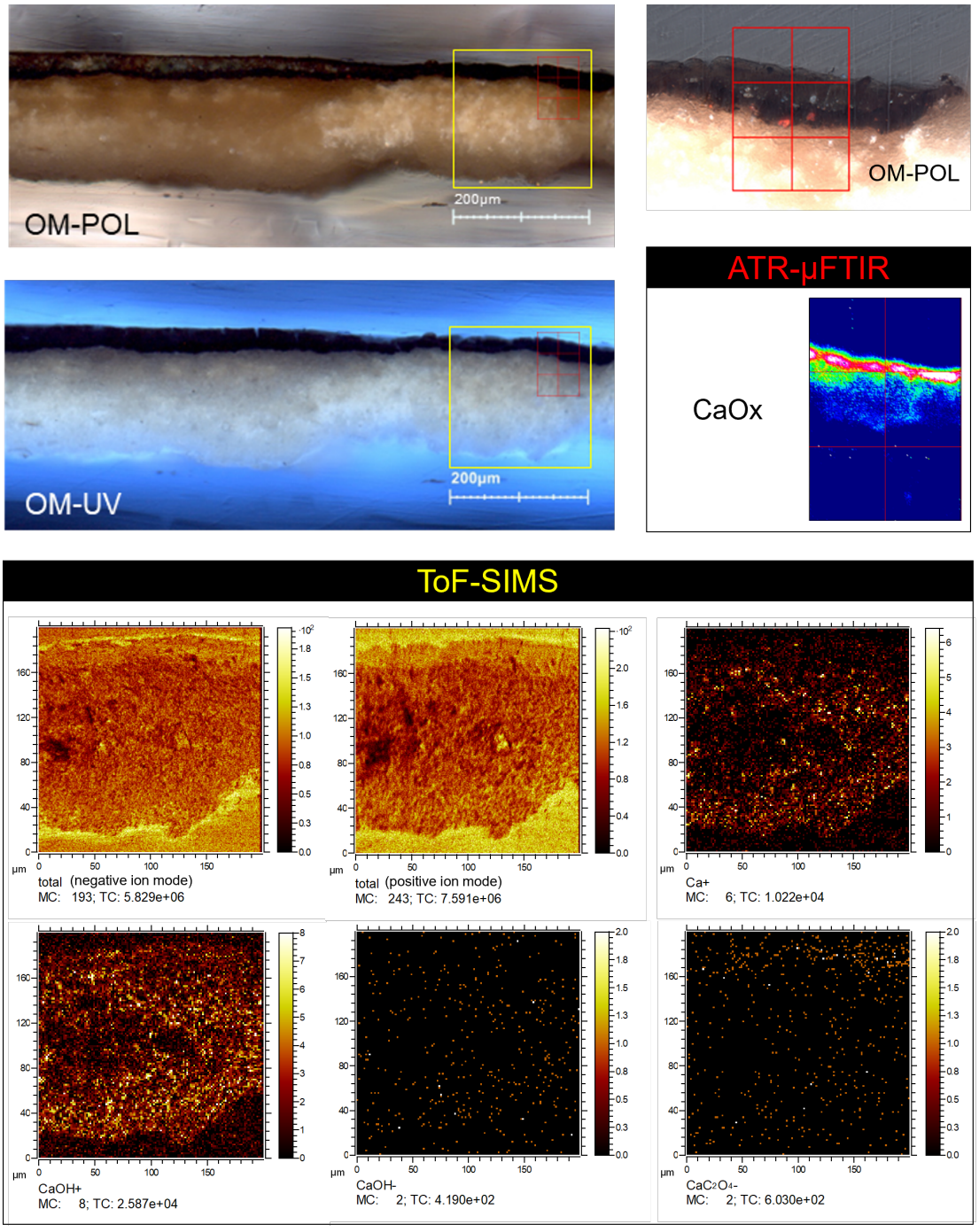

Figure 8.5: POL and UV microphotographs, ATR-µFTIR mappings showing the spatial distribution of CaOx (1336-1296 cm^{-1}), and ToF-SIMS ion images of CaOx-related compounds in the right part of cross-section C30-153. The red and yellow squares in the OM images represent respectively the analysis areas in ATR-µFTIR and ToF-SIMS.

The right side of C30-153 also presents a high concentration of Ca^{+} and $CaOH^{+}$ in the preparation layer and $CaC_2O_4{}^{-}$ in the paint layers, as shown in Figure 8.5. ATR-µFTIR results indeed revealed the presence of CaOx in the top layers.

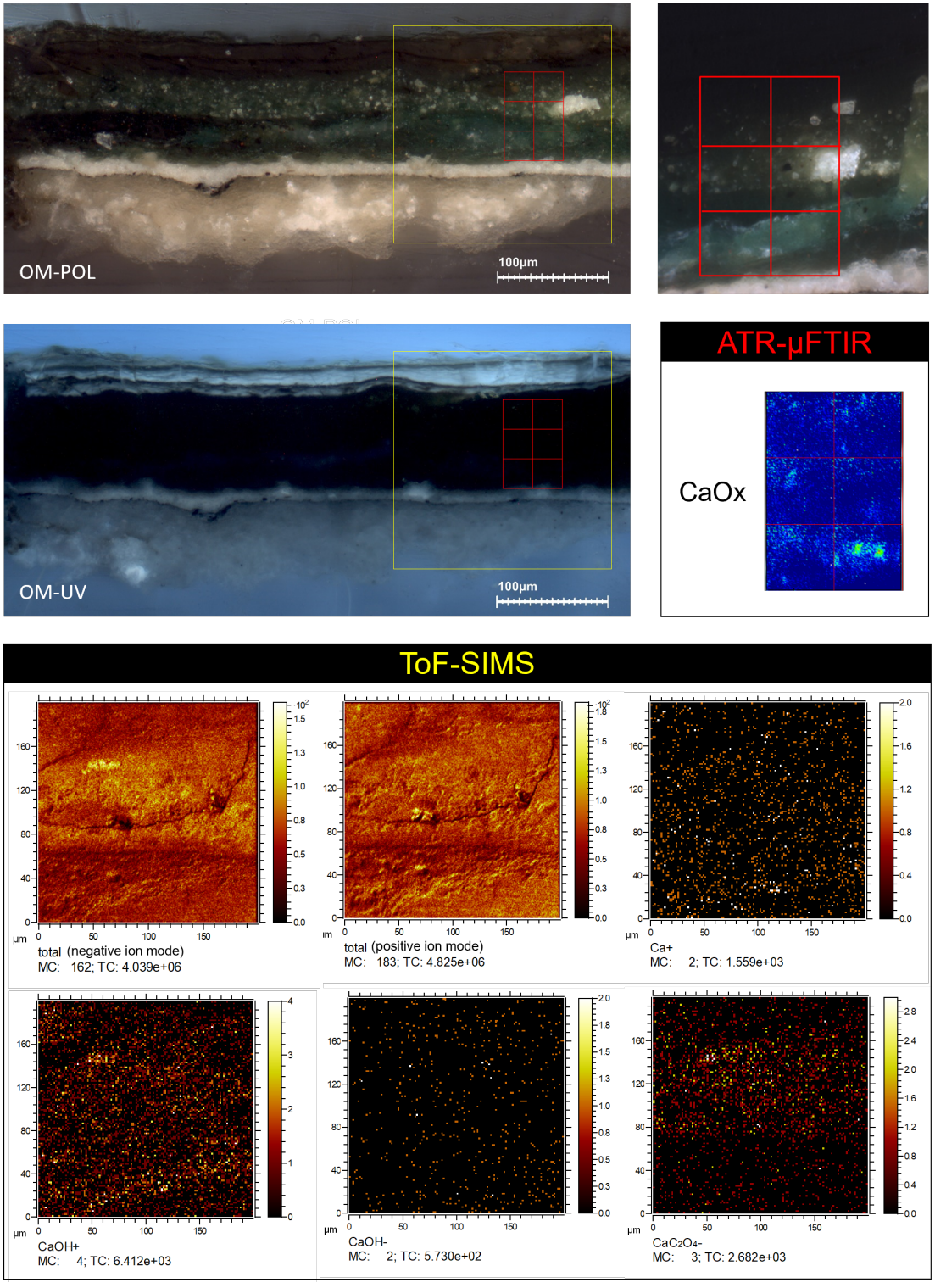

Figure 8.6: POL and UV microphotographs, ATR-µFTIR mappings showing the spatial distribution of CaOx (1336-1296 cm^{-1}), and ToF-SIMS ion images of CaOx-related compounds in cross-section C17-085. The red and yellow squares in the OM images represent respectively the analysis areas in ATR-µFTIR and ToF-SIMS.

In Figure 8.6, $CaC_2O_4^-$ ions are found in the paint layers, relatively well colocalized

with $CaOH^+$ even if the latter's presence extends to the preparation layer.

Mock-up: delayed extraction

The main obstacle to localizing oxalate, CaOx and CuOx in cross-sections is that these peaks are too weak to be distinguished from featureless structures that are very difficult to interpret. The aim of delayed extraction (DE) was to achieve a higher mass resolution that would enable the oxalate peaks to be discerned. As this was the first time this methodology had been used, DE was tested on the mock-up (H1-Ml-br-T6-N1) rather than on historical cross-sections.
It has been proven to efficiently increase the mass resolution by up to more than double, as illustrated in Figure 8.7. The shape of a peak is also modified, becoming steeper on its left side with a slight extension to the right.

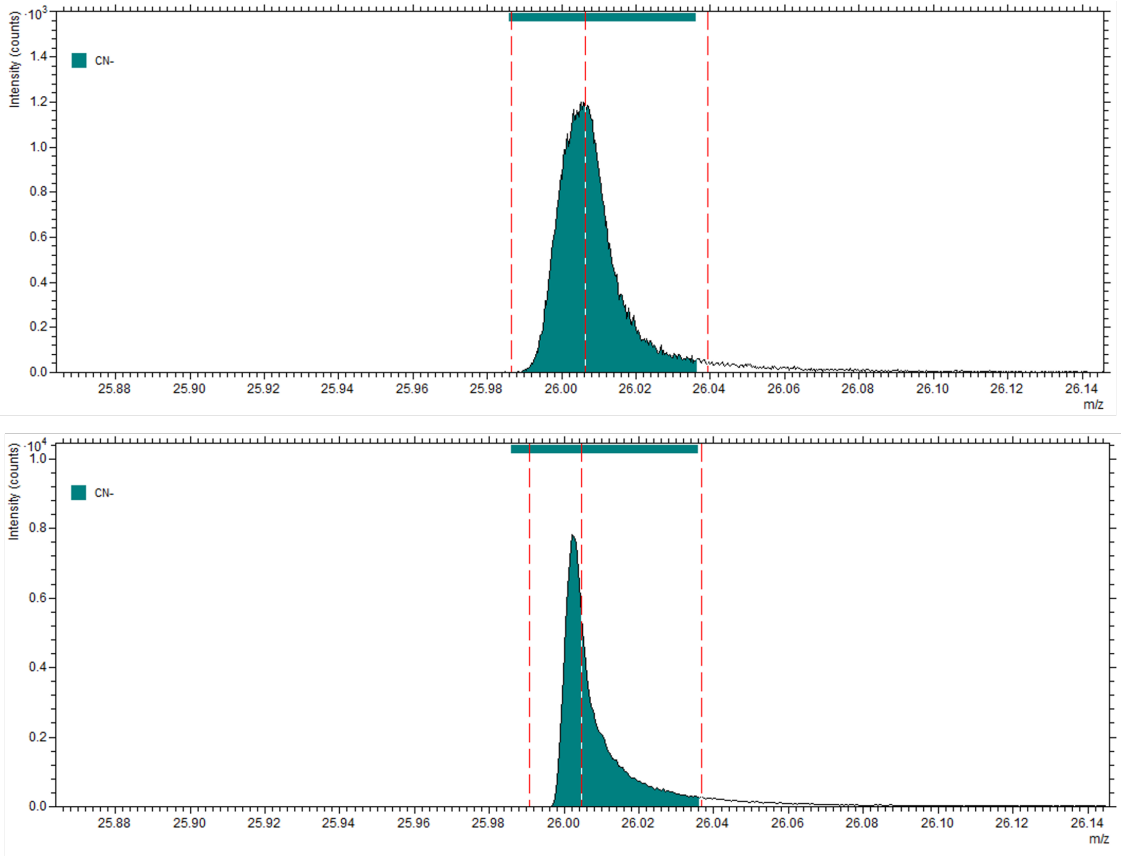

Figure 8.7: CN^- peak in the mock-up with (bottom) and without (top) delayed extraction. Its mass resolution goes from 1809 to 4400 when using DE.

Although the mass resolution is undoubtedly improved to the point of revealing sub-structures around the oxalate peak, it is not sufficient to observe it distinctly, as demonstrated in Figure 8.8. In addition to that, spatial resolution is reduced and the low mass peaks are lost.

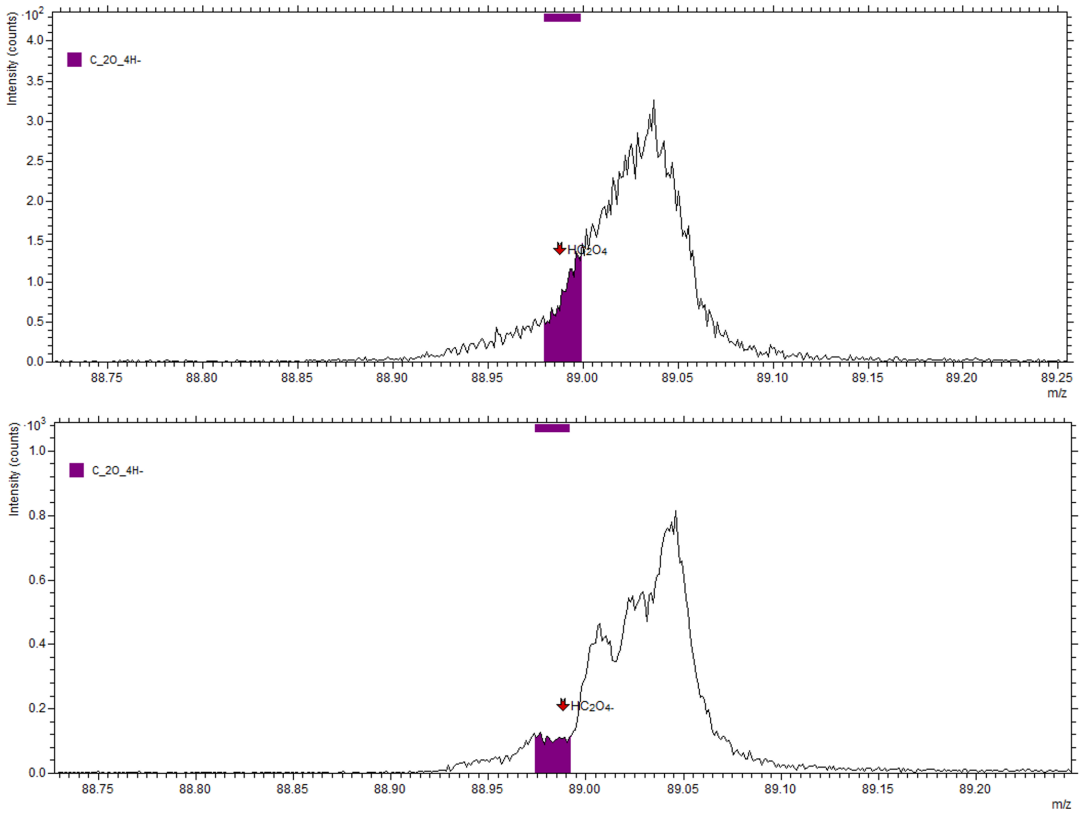

Figure 8.8: $HC_2O_4^-$ peak in the mock-up with (bottom) and without (top) delayed extraction.

Figure 8.9 shows the calcium oxalate-related negative ions for the mock-up with and without delayed extraction. The area in the top left corner presents a higher intensity of $CaC_2O_4^-$, and even $HC_2O_4^-$ (see subsubsection 8.2.1) in both cases, although with a slightly more precise localization with DE.

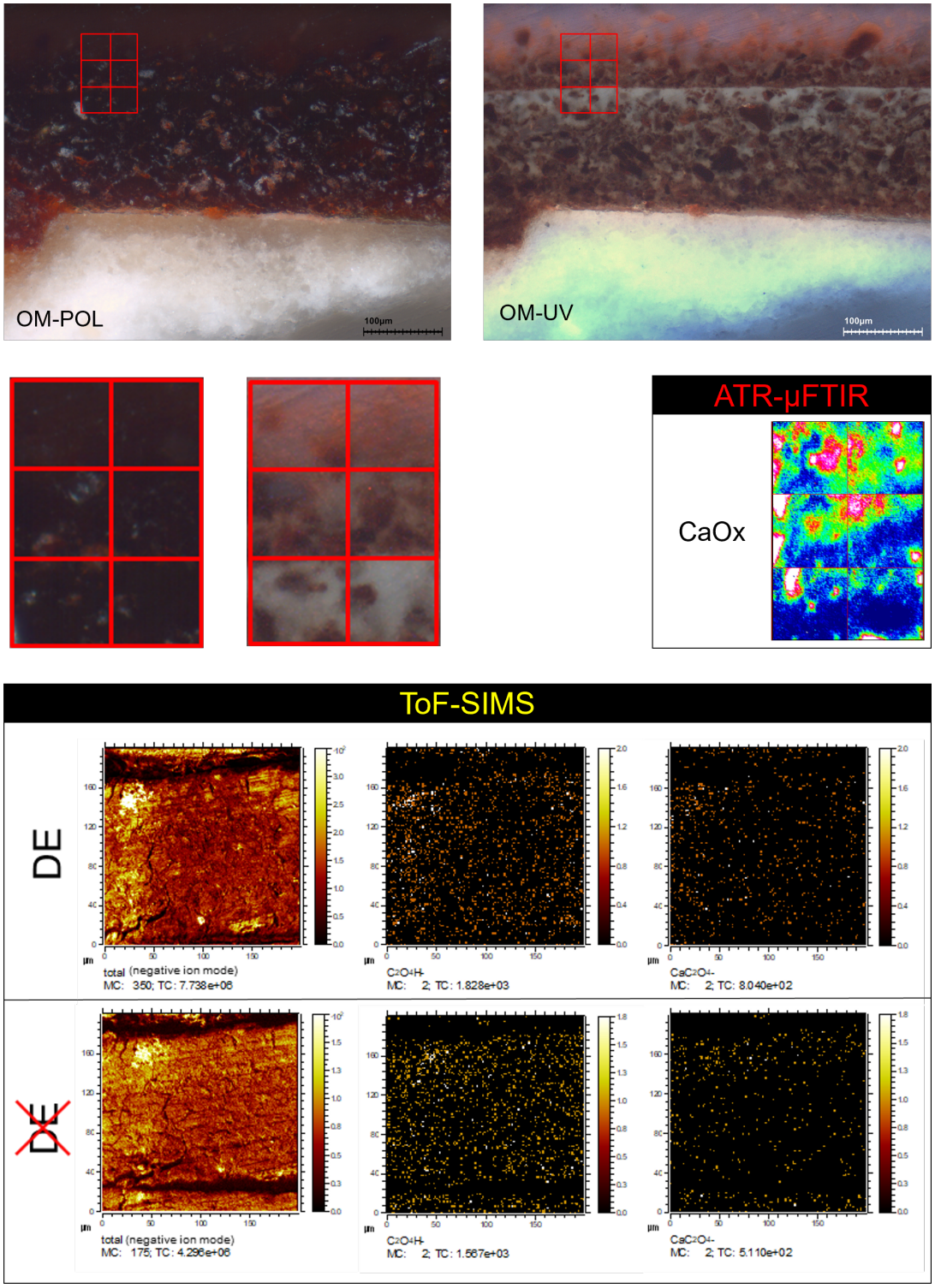

Figure 8.9: POL and UV microphotographs, ATR-µFTIR mappings showing the spatial distribution of CaOx (1336-1296 cm^{-1}), and ToF-SIMS ion images of CaOx-related compounds in the mock-up H1-Ml-br-T6-N1. The red and yellow squares in the OM images represent respectively the analysis areas in ATR-µFTIR and ToF-SIMS.

8.2.2 Interpretation

The presence of $CaC_2O_4^-$ ions in areas consistent with the ATR-µFTIR mappings confirms the presence of calcium oxalate in these cross-sections. Moreover, $CaC_2O_4^-$ tends to appear colocalized with $CaOH^+$, rather than Ca^+. Perhaps $CaOH^+$ originates from the dissociation of one carboxylic function of the two in calcium oxalate molecules, explaining why it is as much observed in areas where CaOx is detected.

Calcium that appears elsewhere in the samples and that is not correlated with oxalate, for instance in the preparation layer of C30-153, likely originates from the calcium carbonate of chalk.

Appendix D displays the $CaC_2O_4^-$ peaks for these four samples. Remarkably, all of them seems to be relatively well-defined. However, in view of the results obtained in the past as part of the MetOx project, including Lebrun's work, and elsewhere in the literature, it is crucial to keep a critical eye. The instrument's resolution is too low to be able to unequivocally ensure that this is indeed a calcium oxalate peak. As demonstrated with delayed extraction, the structure between 127.8 and 128.2 is indeed composed of several sub-peaks, and it is possible that an increased mass resolution would indicate that at the precise m/z where CaOx is supposed to be, there is in fact no peak. Nevertheless, these results still provide optimism for potential future applications of this methodology, and it would be interesting to try it on instruments providing a higher mass resolution.

8.3 Conclusions on ToF-SIMS analyses

As prior studies on the subject have already indicated, the detection of oxalate in ToF-SIMS poses significant complexity. The ion characterizing oxalate alone, $HC_2O_4^-$, was not precisely observed in any of the samples, confirming what H. Lebrun stated in his work.

Satisfyingly, $CuC_2O_4^-$ appears colocalized with copper cations and anions in C21-053 and the left side of C30-153, and concerning $CaC_2O_4^-$, it is often colocalized with Ca^+ and $CaOH^+$ in C17-085, C21-053 and C30-153 (both sides). These results are a good argument for the presence of CuOx and CaOx, respectively, and the correlations with ATR-µFTIR results also point in this direction.

However, their intensities remain quite low. The reason why these compounds are typically observed with very low intensities is likely attributed to their low ionization probabilities. In fact, H. Lebrun already came to this conclusion in his work, which is consistent with our results.

Another main issue of CuOx, CaOx and oxalate in ToF-SIMS is that their m/z ratio is hidden in a large contamination-induced peak very complex to identify (probably containing silicon). Furthermore, the ion mappings show minimal improvement with delayed extraction, and the enhancement in localization is not readily apparent. Even though it clearly provides an excellent mass resolution, delayed extraction also causes the loss of low-mass peaks and a slight deformation of the images. While the conclusive application of DE for locating MetOx in historical cross-sections has not been fully proved in this work, its promising results suggest that one could further investigate this technique using reference powders or mock-ups to study the direct detection of MetOx in ToF-SIMS.

It is also possible that the process of polishing, employed to reach a desired depth within the embedding resin for visualizing the complete stratigraphy of a cross-section and to restore a clean surface after analysis, may have adverse effects on the sample. In fact, sometimes (as in cross-section C21-053) the cross-section cracks during polishing, allowing materials from other layers or even the resin itself to penetrate. This type of damage is annoying, but generally easy to spot. A more insidious concern, yet to be substantiated, would involve the potential global blending of the different compounds on the surface during polishing, thereby posing challenges in identifying and locating the various species. In other words, even if a particular compound is initially localized in a specific area, it will undergo redistribution across a broader zone or the entire surface with each successive pass of the polishing wheel. Consequently, KIK-IRPA researchers are currently looking into alternative techniques to polishing for the analysis of historical cross-sections. For instance, ion beam milling techniques enable the production of pristine cross-sections, devoid of contamination, distortion, crumbling, or smearing. It consists of thinning the sample down by bombarding it with a beam of ions, usually inert gases like argon, which sputters away material from the surface. This controlled removal of material results in a fine cross-section that can be analyzed with high precision [60].

Chapter 9

Investigation of metal oxalates XPS spectra

Looking into potential future XPS studies on historical samples and aiming to better understand common MetOx characteristics, this research explores XPS spectra of metal oxalate powders. A Chenakin et al.'s study characterized transition metal oxalates (Mn, Fe, Co, Ni, and Cu oxalates) in XPS [56], assessing various parameters across these species, including binding energies between metal cations and oxalate anions. However, their studied metal oxalates differ from those in historical paintings. This thesis aims to extract insights from CaOx, CuOx, PbOx, and ZnOx spectra, deepening understanding of these phenomena.

9.1 XPS results and interpretations

9.1.1 Me core-level spectra

Figure 9.1 displays high-resolution metal (Me) spectra of Ca 2p, Cu 2p, Pb 4f and Zn 2p. Their shapes and peak-fitting components differ significantly, making a meaningful comparison between them challenging. Nonetheless, several noteworthy points can be observed.

As shown in Figure 9.1, the Ca 2p line shows the two peaks $2p_{3/2}$ and $2p_{1/2}$ emerging from spin-orbit splitting (SOS) and separated by 3.5 eV. Since calcium has no unpaired electron in its electronic structure, its spectrum does not present multiplet splitting. It appears that the Ca $2p_{3/2}$ spectrum only features one main line at 347.1 eV, which comes close to observations of this line in $CaCO_3$ at ∼347 eV. Metallic calcium nor CaO do not seem to be present in the sample, given the absence of any other peak near ∼346.6 eV or below [61]. This could be attributed

to the high reactivity of alkaline earth metals, meaning that if calcium has been decomplexed from oxalate, it quickly rebinds to form other compounds such as $CaOH^-$ or $Ca(OH)_2$. Hence, it does not rule out the possibility that this peak could also contain single Ca^{2+} ions or other forms of twice oxidized calcium. As calcium contains no electrons in its 3d shell and all its other shells are filled, there is no satellite in the Ca 2p spectrum.

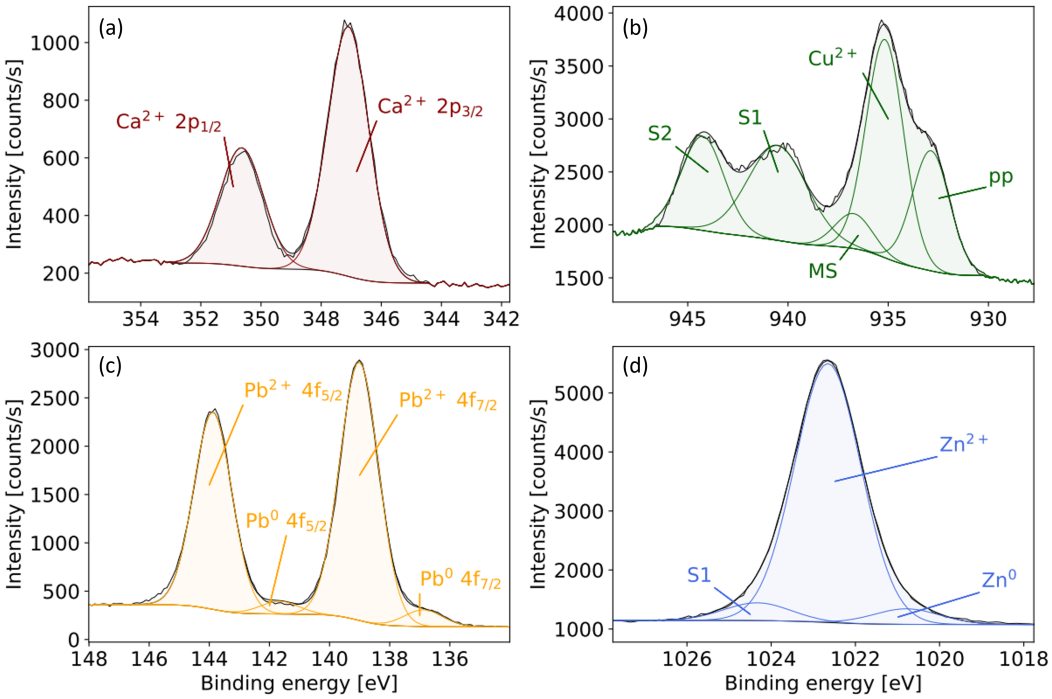

Figure 9.1: Me core level spectra of the four analyzed oxalate powders. The raw data is represented in black. The fitted curves and components are (a) in red for CaOx, (b) in green for CuOx, (c) in yellow for PbOx and (d) in blue for ZnOx. This color code is maintained throughout the study.

The copper spectrum is the most complex of the four, fitted with five different components. Starting from the lowest binding energy, one finds a pre-peak (pp) at 932.9 eV, corresponding to the presence of Cu ions in a lower oxidation state such as Cu(I), possibly from Cu_2O (932.2 eV [62]) for instance, as proposed in the literature [55]. It also aligns with the typical BE of metallic Cu^0 of 932.6 eV [62]). They might originate from analysis-induced degradation in the sample, causing oxygen vacancies in nearby sites. In literature, the pp is already described as intense in CuOx in comparison to other transition metal oxalates (Mn, Fe, Co, Ni) while representing ~6.5% of the Cu $2p_{3/2}$ line, but its intensity is almost three times greater here, i.e. 18.92%. This suggests a more advanced degradation of the CuOx powder in our case. Other works [55] have also shown that this pp increases with XPS irradiation, up to at least 41%.

Next, the most prominent peak at 935.2 is associated with Cu^{2+} compounds, from the metal oxalate.
The smaller component at 936.7 eV appears due to multiplet splitting and the two structures at 940.5 eV and 944.2 eV are satellites, respectively abbreviated S1 and S2 in Figure 9.1. Copper oxalate is the sample displaying the most intense and well-resolved satellites.
Table 9.1 shows the adequacy between this work's data and Chenakin's with regard to their positions and areas. ΔBE(A-B) (in eV) refers to the binding energy shift between peaks A and B and A/B ratio refers to the ratio of the areas of peaks A and B. For instance, the binding energy shift between the MS and Cu^{2+} components, ΔBE(MS-Me^{2+}), is equal to ∼1.6 eV, which closely aligns with the value obtained by Chenakin's team of ∼1.4 eV.
They state that the nature of the ligand and the type of bonding (more or less covalent) play a role in the apparition of the satellites and thus, information could be extracted from them. However, when observing the distribution and proportion of S1 and S2 in CuOx, it closely resembles what is reported in the literature for oxide +2, or even for hydroxide. Since the synthesis is carried out from nitrates that are no longer detected, the copper can only exist in the form of oxalate, oxide +2, oxide +1, hydroxide +2, or reduced 0. The presence of a prepeak indicates the existence of a portion of copper in either the 0 or +1 oxidation state, and the positions and shapes of the satellites ultimately do not provide the means to distinguish between an oxalate, an oxide +2, or a hydroxide +2. It is only by verifying the ratio between copper and carbon in the oxalate that an assessment of the compound's purity can be made.

Table 9.1: Comparison between the experimental results obtained in this work and the ones obtained by Chenakin et al. [56] relative to Cu 2p satellites in copper oxalate.

	This work	Chenakin et al. [56]
ΔBE(S1-Me)	5.2	5.3
ΔBE(S1-Me^{2+})	5.5	5.3
ΔBE(S2-S1)	3.7	3.9
S1/(Me^{2+}+MS) ratio	0.60	0.59
S1/(Me^{2+}+MS) ratio	0.43	0.43
(S1+S2)/Me^{2+} ratio	1.19	1.16

The Pb $4f_{7/2}$ line contains its main line at 139.0 eV, associated to lead oxalate. The small component at 136.9 eV is attributed to metal lead, Pb(0) [63], likely due to

slight degradation or contamination. There is no multiplet splitting. The Pb $4f_{5/2}$ is also visible in Figure 9.1, 4.8eV higher.

Zn $2p_{3/2}$ does not present MS and takes the form of a single line. Its interpretation is complicated by the overlap between its components [62]. Its main component, which is considered to arise from Zn^{2+} in the ZnOx, appears at 1022.7 eV and is enclosed between two small peaks at 1020.8 eV and 1024.3 eV. The former corresponds to the BE of metallic zinc Zn(0), which again probably originates from contamination and degradation. The second peak at 1024.3 eV could be a small satellite, similar to the Cu spectrum. However, given that the 3d shell is filled and stable, it seems unlikely that a satellite will be observed, or only in a very small contribution. The widening would then be due to a less-than-optimal proportion of Gaussian or Lorentzian contribution in the fitting peak, rather than to the actual presence of two small peaks.

Measured SOS values of the Me spectra for the metal oxalates have been compared with each other and with their respective oxides and metallic forms. To reproduce Chenakin's paper's methodology, SOS(Me) and SOS(MeO) values have been taken from the NIST database [64], averaged [56], and gathered in Table 9.2. Whatever the ligand, the following trend is constant for all four metals: SOS(Ca) < SOS(Pb) < SOS(Cu) < SOS(Zn). Regarding the analysis of transition metal oxalate powders, Chenakin et al. report a nearly linear dependence of the SOS of their 2p spectral lines on the cation effective nuclear charge Z^*. This trend is indeed observed when combining their values for Mn, Fe, Co, and Ni oxalates and ours for Ca, Cu and Zn oxalates, as shown in Figure 3.6.

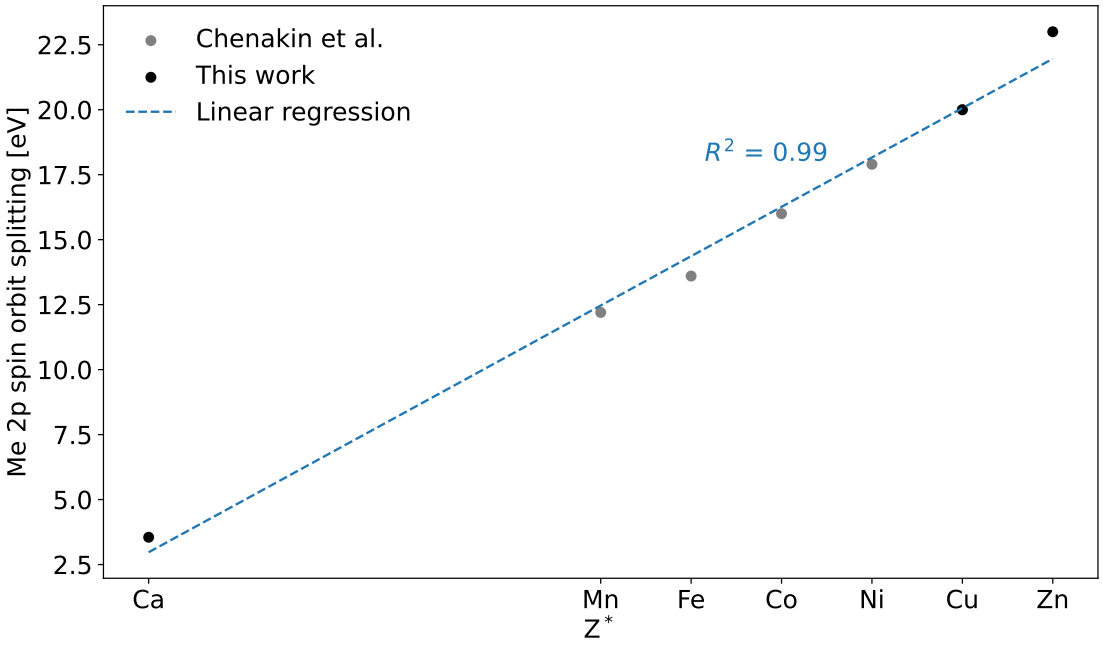

Figure 9.2: Spin-orbit splitting in Me 2p spectra of metal oxalates versus the effective nuclear charge of the metal cation Z^*. The linear dependence is demonstrated by a linear regression with a coefficient of determination R^2 of 0.99.

While an increase of SOS with Z^* has been observed in this work for calcium, copper and zinc (although calcium breaks the linear tendency observed in Mn, Fe, Co, Ni, Cu and Zn), lead does not fit into this trend. This was to be expected since the valence electron shell observed for this metal is 4f instead of 2p, although the formula of Z^* takes into account this difference of shell ($Z^* = Z - s$ where Z is the atomic number and s the adequate screening constant) [65, 66]. Because of this shell difference, lead actually must be set aside when interpreting the SOS.

Table 9.2: SOS values (in eV) for each metal oxalate (from analysis), oxide and metallic Me lines (from literature), along with the corresponding atomic number Z, screening constant s and effective nuclear charge Z^* [65, 66].

	Ca $2p_{1/2}$-$2p_{3/2}$	Cu $2p_{1/2}$-$2p_{3/2}$	Pb $4f_{5/2}$-$4f_{7/2}$	Zn $2p_{1/2}$-$2p_{3/2}$
Oxalate	3.55	20.00	4.83	23.00
Oxide	3.45	19.95	4.85	23.07
Metal	3.70	19.83	4.90	23.09
Z	20	29	89	30
s	4.15	4.15	50.55	4.15
Z^*	15.85	24.85	31.45	25.85

A second observation, concerning the ligand, has been made by Chenakin. He observed an increase of the SOS from the metals to the metal oxide, and from

the metal oxide to the metal oxalate in Mn, Fe, Co, and Ni oxalates. As shown in Table 9.2, this trend is observed here for copper: SOS(Cu) < SOS(CuO) < SOS(CuC2O4). The other three metals do not show the same trend. However, the small variations between the SOS values of the different ligands for the same metal remain smaller or on the order of 0.1 eV. To remain rigorous and critical, it is wiser not to draw unfounded conclusions from these trends, even the ones presented in Chenakin's paper. Chenakin et al. also assert that the rise in the SOS with Z^* progresses more rapidly for metals and oxides than for oxalates, which could explain why greater Z^* leads to lower SOS(MeC_2O_4) in comparison to SOS(Me) and SOS(MeO) among Ca, Pb and Zn in this study.

Finally, Chenakin and his team found out that the Me 2p shift between metallic and oxalate states ΔBE(Me-Me^{2+}) increases when the electronegativity difference $\Delta\chi$ between the metal and the ligand decreases, i.e. when the covalency of the Me-O bond increases. According to the Allen scale [67], χ(Ca) = 1.034, χ(Cu) = 1.85, χ(Pb) = 1.854, and χ(Zn) = 1.59. Given χ(Oxalate) = 3.46, the $\Delta\chi$ values for the four metal oxalates under study are: PbOx ($\Delta\chi$ = 1.606) $\leq$ CuOx ($\Delta\chi$ = 1.61) < ZnOx ($\Delta\chi$ = 1.87) < CaOx ($\Delta\chi$ = 3.46)). Unfortunately, this tendency is not replicated here: Zn=(ΔBE(Me-Me^{2+}) =1.01) < Pb(ΔBE(Me-Me^{2+}) =2.21) < Ca(ΔBE(Me-Me^{2+}) =1.29) < Cu(ΔBE(Me-Me^{2+}) =2.56), probably because the greater differences among our MetOx samples pose challenges when attempting to apply these interpretations to their Me spectra.

9.1.2 C 1s and O 1s core-level spectra

Every oxalate powder presents a characteristic two-peak C 1s line as shown in Figure 9.3, which is typical of metal oxalates [55, 56, 68, 69]. This core-level spectrum was fitted using four components, similarly to Chenakin's work. Starting from the lowest BE, the first one corresponds to the reference peak of C-C/C-H bonds, set at 284.8 eV. It is followed by the C-O peak at 286.5 ± 0.12 eV and the O-C-O at 288.7 ± 0.15 eV, which corresponds to the oxalate anion $C_2O_4{}^{2-}$ and is, accordingly, the largest component [58]. C-C/C-H and C-O peaks point out that the oxalate powders have been contaminated with other carbon-based compounds, or degraded. The fourth and smaller one is a satellite peak and will be addressed in subsection 9.1.3.

While the relative positions of the peaks correspond to the literature, the spectra obtained in this work are, on average, shifted approximately 0.3 eV lower, even after accounting for the 0.2 eV adjustment due to their reference set at 285 eV instead

of 284.8 eV. However, upon examining their C 1s spectra, it appears that their CC/CH peaks are occasionally very close to the noise level, potentially impacting their calibration.

Three components were used to fit the O 1s core-level spectrum, visible in the right part of Figure 9.3. From the lowest to the highest BE, the first ones are attributed to O^{2-} from O-Me bonds at 530.1 ± 0.4 eV and O-C-O bonds in $C_2O_4{}^{2-}$ at 532.1 ± 0.4 eV, which significantly dominates the other two. The small component S1 is discussed in the next section. These values are in agreement with those obtained by Chenakin with 0.3 eV less.

Several features of both C 1s and O 1s spectra can be evaluated in relation to each other. Firstly, the BE shift between the C(OCO) and O(OCO) components, abbreviated ΔBE(OCO), is nearly identical for every oxalate and equals 243.4 ± 0.3 eV, as confirmed by Chenakin et al. The tendency of this value to remain constant within the same carboxylate family has also already been demonstrated for formates and acetates for instance, that have close ΔBE(OCO) of ∼243.5 and ∼243.3, respectively. It can have values further away from these in other types of components, ranging from 242.1 for carbonates to 246.2 for metal carbonyls, for example. This confirms the usefulness of ΔBE(OCO) in the differentiation of organometallic compounds such as oxalate within a sample, especially given its independence from any charge-induced BE shift.

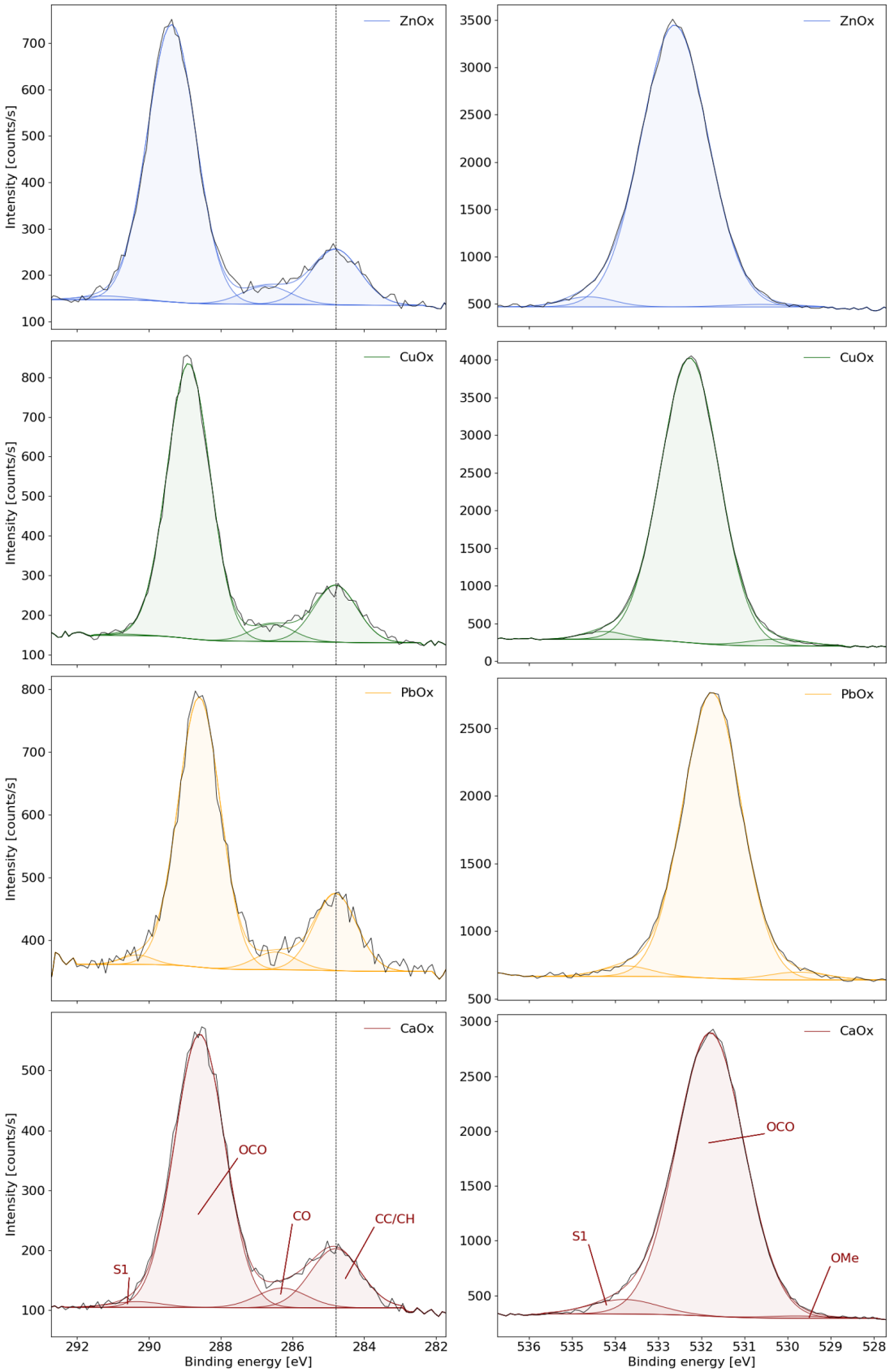

Figure 9.3: XPS C 1s (left) and O 1s (right) core-level spectra of the MetOx. The dashed line represents the reference value of 284.8 at which the CC/CH peak is set.

Moreover, as found by Chenakin and shown in Table 9.3, the FWHM of C(O$\underline{C}$O) and O($\underline{O}$C$\underline{O}$) both increase across the four oxalates in the same order: PbOx, CuOx, ZnOx, CaOx in our case. Furthermore, C($\underline{O}$C$\underline{O}$) line is thinner than the O($\underline{O}$C$\underline{O}$) line within the same oxalate. This can be explained by two main reasons. Firstly, oxygen is likely present in multiple chemical states. However, due to its high electronegativity, it is less susceptible to environmental influences, resulting in minimal shifts, typically in the range of a few tenths of an eV, and its peak appears broadened. Further decomposition of the peak would be meaningless given the resolution of the instrument. Secondly, unlike metals in their metallic state, which exhibit sharp peaks, other elements like oxides possess a more 'flexible' atomic arrangement. Unless they feature a highly stable crystalline structure, there exists a consistent variation in short-scale bond lengths. This variance translates to increased vibration. During the photoelectric effect, a broader distribution of bond energies forms around an average value. Consequently, a single component will display greater width.

Table 9.3: FWHM (in eV) of the O$\underline{C}$O, $\underline{O}$C$\underline{O}$ and Me^{2+} components in the metal oxalate powders analyzed in XPS.

	CaOx	CuOx	PbOx	ZnOx
FWHM(O$\underline{C}$O)	1.64	1.42	1.39	1.59
FWHM($\underline{O}$C$\underline{O}$)	1.85	1.60	1.60	1.82
FWHM(Me^{2+})	1.85	2.19	1.52	1.86

9.1.3 C 1s and O 1s satellites

Given that the analysis window stops at ∼297 eV for carbon and ∼540 eV for oxygen, only the lowest BE satellite of each is observed. This consists of the minor component at 290.5 ± 0.2 eV in the C 1s spectrum and the one at 534.1 ± 0.4 eV in the O 1s spectrum, both labeled S1 in their respective spectra in Figure 9.3.
Literature [55, 56] has however reported other satellites at higher binding energies. For carbon, two more satellites would have been observed ∼7.69 eV and ∼10.15 eV above the O$\underline{C}$O peak.
Concerning oxygen, CuOx did not present any other intense satellites but the other transition metal oxalates had two to three of them at higher binding energies at ∼10 eV and higher.

C(S1) could be a shake-up satellite arising because of the excitation of bonding and antibonding $2\pi^*$–Me 3d combinations in the Me–(O–C–O) bonding of the

metal oxalate, and corresponding to an unscreened final state when there is no charge transfer between the ligand and the metal.
The small component at 534.1 ± 0.4 eV in the O 1s spectrum may be associated with the presence of adsorbed water, along with C−OH/COOH, or CO_3H [55, 56].

While Chenakin obtained a proportional relationship between S1 and O<u>C</u>O as well as between S1 and 1/(CC/CH), these findings were not replicated in the present study. Nevertheless, this information should be carefully evaluated as the presence of the proposed C(S1) is questionable. In both their and our samples, this component remains at very low levels and is barely distinguishable from the signal-to-noise ratio. It is also possible that this extremely faint peak actually corresponds to the elevation of the baseline due to electrons losing some of their kinetic energy through inelastic collisions on their path to the surface. This region (energy lost peak) is quite challenging to analyze since it depends on the contamination and material density.
The same applies to O(S1). Additionally, the OMe component also remains very low, and it is possible that these two small peaks are in fact artifacts caused by an imbalanced Gaussian-Lorentzian curve fitting of the oxygen line.

9.1.4 X-ray induced Auger spectra

XR-induced LMM Auger lines have been recorded for copper and zinc oxalates, and their modified Auger parameters α'(Me) have been computed. As stated in subsection 3.3.4, this parameter is calculated as $\alpha'(\text{Me}) = E_K(\text{Me Auger}) + E_B(\text{Me 2p})$. The maxima of the CuOx and ZnOx Auger lines, shown in Figure 9.4, being respectively 916.1 eV and 986.8 eV in kinetic energy, modified Auger parameters for copper and zinc are $\alpha'(\text{Cu}) = 1851.26$ eV and $\alpha'(\text{Zn}) = 2009.49$ eV. Literature indeed reports a similar value of 1851.5 eV [56] for the former, and 1851.33 eV for its corresponding oxide CuO [70]. Zinc oxide has shown a modified Auger parameter of 2010.14 eV [62]; however, no value for zinc oxalate has been found in the literature.

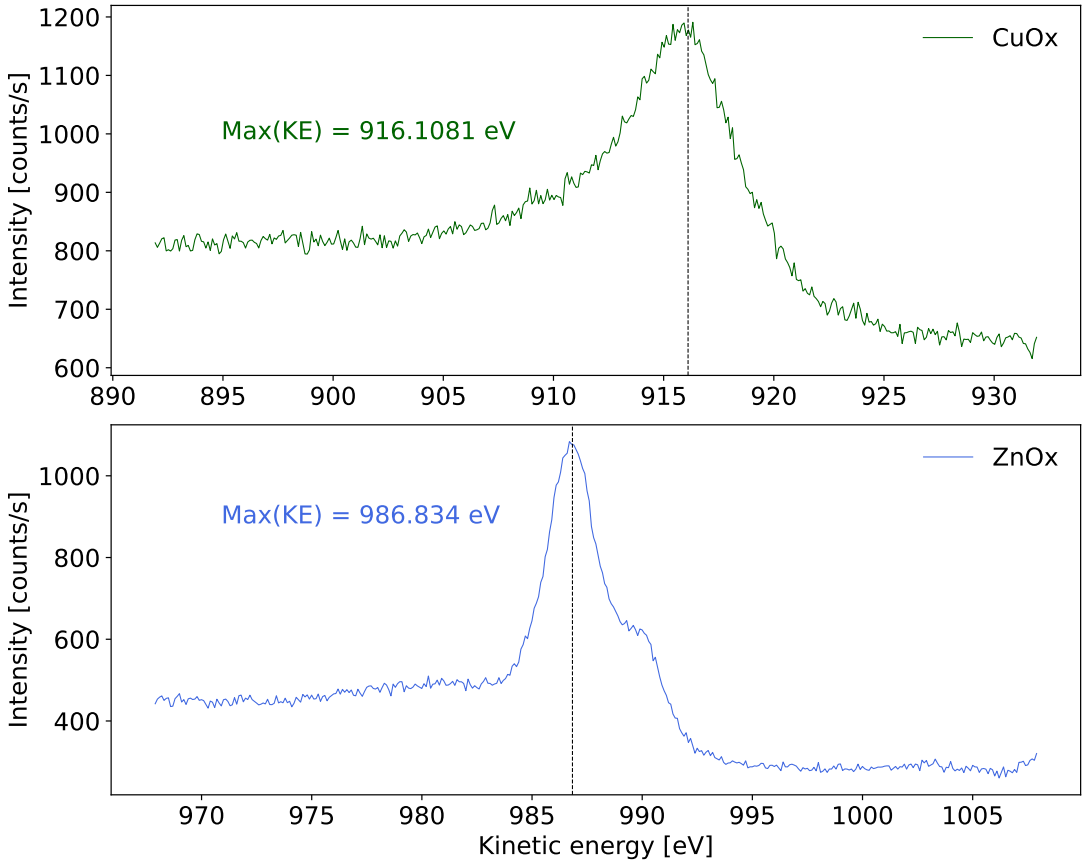

Figure 9.4: XR-induced Auger Me LMM lines in CuOx (top) and ZnOx (bottom).

9.1.5 Valence band

To ensure comprehensive insights and maximize our understanding of these metal oxalates, an investigation of their valence band was conducted.

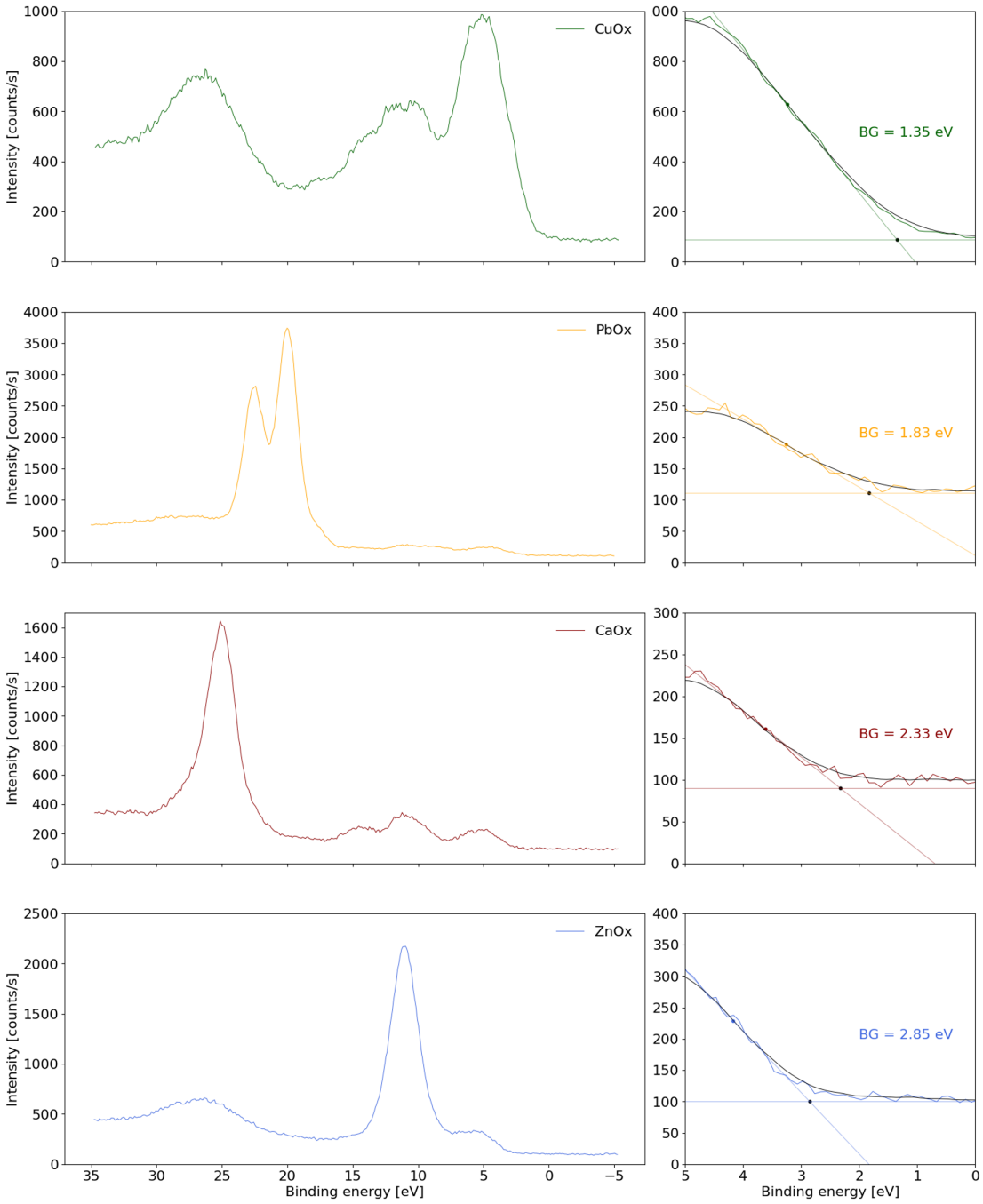

Figure 9.5: VB spectra of the four analyzed metal oxalate powders. The raw data is represented in the color specific to the MetOx in question.

The VB spectra of the four metal oxalates are displayed in Figure 9.5. They exhibit diverse shapes due to the distinct binding energies of valence electrons for each element. The bandgap (BG) is obtained by finding the intersection between the tangent to the curve at the first inflection point and the baseline of the curve [71]. The BG are 1.35, 1.83, 2.33, 2.85 for CuOx, PbOx, CaOx and ZnOx respectively. Concerning CuOx, a BG of 1.2-1.5 eV has been found by Chenakin, which is in

good agreement with this analysis.

9.1.6 Atomic ratios

Taking into account the oxalate-related components of the carbon and oxygen core-level spectra (respectively O-C-O and O-C-O), the stoichiometric atomic ratios for metal oxalates are expected to be O/C=2, O/Me=4 and C/Me=2 [56]. Table 9.4 shows the experimental ratios obtained for each powder.

Table 9.4: Atomic ratios in the metal oxalate powders analyzed in XPS.

	CaOx	CuOx	PbOx	ZnOx
OCO/OCO	2.01	2.07	1.87	1.75
OCO/Me	1.85	1.93	1.73	2.04
OCO/Me	3.72	4.01	3.24	3.58

Copper oxalate presents almost exact stoichiometric ratios. As explained in section 7.2, the CuOx data comes from a different analysis and might require separate consideration within this context, especially if analysis-induced degradation impacts the atomic ratios. The fact that it is the only powder of the four to have almost exact stoichiometric ratios could be due to its different analysis conditions, demonstrating the effect of the instrument on the degradation of the samples.

The OCO/OCO ratio also matches the theoretical value in CaOx. Its slight difference below the theoretical value of 2 for PbOx and ZnOx could ensue from the redundancy of C=O carbonyl groups associated with structural imperfections or contamination (i.e. remaining solvent from the synthesis), or from the XR-induced disruption of O−Me bonds leading to loss of oxygen. Apart from CuOx (and OCO/Me in ZnOx), OCO/Me and OCO/Me are always below the expected stoichiometric ratios.
On the one hand, this could be explained by an advanced degradation stage of the metal oxalate, as proposed in the literature [55] (see subsection 9.1.8). Due to its breakdown, the proportions of oxalate-related components are reduced, and so are these ratios. Copper oxalate would thus be less degraded than the other three.
On the other hand, the intensities and structures of the C 1s and O 1s lines may be affected by impurities introduced during synthesis and/or storage, leading to non-stoichiometric atomic ratios. The surface concentration of CC/CH and CO can be increased due to contamination by carbon-containing compounds, decreasing at the same time the relative ratios of OCO and OCO to the metal.

Chenakin's findings indicate that the contamination by hydrocarbons decreases in the series of transition metal oxalates, i.e. with the increase of the covalency of the Me−O bond. In this case, as shown in subsection 9.1.1, the covalency of this bond increases along PbOx < ZnOx < CaOx. Therefore, it is expected that PbOx would exhibit higher susceptibility to contamination, leading to lower O$\underline{C}$O/Me and $\underline{O}$C$\underline{O}$/Me ratios. Following this trend, ZnOx is next in line, while CaOx displays the least contamination. This sequence aligns well with the observed data.

In any case, it is likely that the analysis chamber already contained a certain quantity of CC/CH-containing compounds from previous analyses because it has been a long time since it was cleaned (baked-out). This would lead to the indirect conclusion that there were single Me nanoparticles in the sample that have been able to capture them, which would not have been the case if they had been bound to oxalate.

9.1.7 Charging effects

As explained in section 3.1, the insulating properties of the oxalates lead to strong charging effects after photoelectrons escape from the surface. The magnitude of these effects can be deduced from the BE shift of the C-C/C-H component in comparison to its reference value, i.e. 284.8 eV in this work. The larger the shift, the stronger the charging effect and the dielectric properties of the sample. The widths of these shifts are displayed in Table 9.5. The fact that it is more intense can be attributed either to lower initial purity or to greater degradation. The combination of vacuum, XR and flood gun is well known for partially reducing some of the more sensitive materials, and oxalates can certainly qualify as such.
It is worth noting that for each sample whose composition was analyzed in this work, the C 1s core spectrum obtained at the end of the sequence does not indicate any undesirable BE shift with regards to the one recorded at the beginning, given all the differences of < 0.04 eV between the two while the instrument has a precision of 0.1 eV. This confirms that the charging has remained constant over the analysis, which is essential for reliable measurement.

Table 9.5: Surface charging-induced shift (in eV) for the four metal oxalate powders analyzed in XPS.

	CaOx	CuOx	ZnOx	PbOx
CC/CH shift	9.7	9.7	9.8	10.0

The width of the BE shift slightly increases with Z^* along CaOx < CuOx < PbOx

< ZnOx. Despite the values being very close to each other, the ZnOx and PbOx shifts slightly surpass the others, which coincides with their sub-stoichiometric OCO/OCO ratio, which could confirm that surface charging might depend on imperfections in the composition and/or structure of the compounds [56].

However, this should be approached with caution, as these values are very similar to each other and the technique used by the Chenakin team is different than the one used in this work. In fact, they press the powders onto gold foils to better observe this phenomenon, whereas here they are pressed into cupules and their surface is negatively saturated with the flood gun, which could obscure the subtle effects that would differentiate their dielectric properties. They obtain charges stabilized between +5 and +8 eV, versus ~ -10 eV in this case, which corresponds to the saturation in electrons of the surface. This value may fluctuate based on surface composition, typically falling within the range of -9 to -12 eV. However, in this scenario, all the powders displayed almost the same charging level. This does not imply the powders are identical (given the varying metals), but it suggests that this entire group of powders can reach electron saturation at a consistent level during analysis.
Chenakin and his team likely did not succeed in implementing a comparable system (or they do not mention it). However, the action of pressing the powder onto a gold foil, enabling partial stabilization, and the utilization of a non-monochromatic anode that naturally generates photons and secondary electrons capable of aiding in neutralization, suggests that employing a flood gun might not have been necessary. An attempt to reproduce these results was made using indium foil in this work, but the results were inconclusive. The surface charge was very unstable and reached excessively high levels of up to several hundred eV, necessitating the utilization of the flood gun anyway. Consequently, the laboratory did not have the chance to approach their analysis conditions more closely. It is possible that the technique was not yet perfected, or that the samples were too insulating.

9.1.8 Metal oxalate degradation during XPS measurements

XPS measurements have been found to be deleterious for metal oxalates. This section focuses on analysis-induced degradation in this reductive environment under vacuum (which is, of course, not representative of the actual paint degradation process).

In 2016 [55], the degradation of transition metal oxalates in XPS, including copper oxalate, has been investigated. This research indeed deduced that CuOx was

particularly prone to XR-induced degradation, that damages the oxalate's polymeric structure and modifies its surface composition. Me−OCO and C=C bonds are broken, CO_2 is produced, especially for low oxalate decomposition temperatures or high second ionization potentials of the bivalent metal atom Me. X-ray exposure also favors the desorption of water of crystallization, especially for oxalates with low temperatures of dehydration. All of this results in an increase in BE shifts and pp, as well as a decrease in oxalate-related peaks in the carbon, oxygen and metal spectra. As stated previously, they also note a decrease in oxygen concentration and atomic ratios C/Me and O/Me, which explains the sub-stoichiometric values obtained for these ratios in this work.

Our second C 1s spectrum indicates that the relative atomic concentrations of the different carbon components vary during analysis. As shown in Table 9.6, in all of the four powders, the O$\underline{\text{C}}$O component is found to decrease between by the end of the analysis, while the CC/CH one increases, suggesting a breakdown of the oxalate.
However, as mentioned in section 7.2, it should be noted that the CuOx data come from a different analysis batch than the other three and therefore cannot be directly compared with them. Based on its ∼1 final to initial concentrations ratios (0.99 for O$\underline{\text{C}}$O and 1.01 for CC/CH), CuOx appears to have undergone less degradation than any of the powders from the other analysis.

Table 9.6: Atomic concentrations ratios of the main C 1s components before and after analysis for CaOx, PbOx and ZnOx.

	CaOx	PbOx	ZnOx
$(O\underline{C}O)_f/(O\underline{C}O)_i$	0.94	0.95	0.92
$(CC/CH)_f/(CC/CH)_i$	1.09	1.10	1.40

Across the other set of samples (CaOx, PbOx and ZnOx powders), a consistent pattern emerges between these two C 1s components. While the distinctions between the values for CaOx and PbOx remain weak, the ZnOx suggest that it is the most degraded powder. It is likely that the degradation rate shown by this tendency is strongly influenced by the order of analysis, i.e. CaOx, PbOx, and lastly ZnOx, with CuOx breaking the trend since its data originates from another analysis.

9.2 Conclusions on XPS analyses

This comprehensive XPS study offered valuable insights into the chemical composition and electronic states of calcium, copper, lead, and zinc oxalates. Notably, with the exception of CuOx, this study represents the first of its kind for the other metal oxalates mentioned.

The four Me spectra have been recorded, providing a reliable series of reference spectra for eventual future analyses. An increase of SOS with Z^* is observed in this study along calcium, copper, and zinc, but lead does not conform to this trend. This is expected, given that lead's valence electron shell is 4f instead of 2p.
Each oxalate powder displays a characteristic two-peak C 1s line, typical of metal oxalates. The O-$\underline{C}$-O peak appears at 288.7 ± 0.15 eV, representing the oxalate anion $C_2O_4{}^{2-}$. The presence of C-C/C-H and $\underline{C}$-O peaks indicates contamination or degradation of oxalate powders. The main line O 1s core-level spectrum, relative to $\underline{O}$-C-$\underline{O}$ bonds in $C_2O_4{}^{2-}$, appears at 532.1 ± 0.4 eV. The BE shift between C(O$\underline{C}$O) and O($\underline{O}$C$\underline{O}$) components, denoted as ΔBE(OCO), is consistent across oxalates at 243.4 ± 0.3 eV. This value's stability within the same carboxylate family can be useful in distinguishing organometallic compounds like oxalates within a sample, independent of charge-induced BE shifts.
Additionally, Cu and Zn Me 2p Auger lines were recorded, and the band gaps of the four investigated MetOx increase along CuOx < PbOx < CaOx < ZnOx.
Then, the expected atomic ratios in metal oxalates are addressed. The theoretical stoichiometric ratios are O/C=2, O/Me=4, and C/Me=2. Experimental ratios show deviations due to structural imperfections, contamination, or XR-induced disruption of O−Me bonds. Impurities from synthesis or storage could affect C 1s and O 1s line intensities and structures, impacting atomic ratios. The study suggests that the analysis chamber's residual compounds might have influenced the results, indicating the presence of single Me nanoparticles in the sample.
Strong charging effects were observed in the MetOx powders during XPS analysis, testifying to their highly insulating nature.
Finally, the negative impact of XPS measurements on metal oxalates has been highlighted, especially during lengthy analyses. The oxalate can breakdown and Me−OCO and C=C bonds break, producing CO_2, and altering surface composition. X-ray exposure also can also lead to water of crystallization loss and changes in binding energies.

The Me−ligand affinity, or covalency of the Me−O bond, decreases along PbOx

($\Delta\chi = 1.606$) > CuOx ($\Delta\chi = 1.61$) > ZnOx ($\Delta\chi = 1.87$) > CaOx ($\Delta\chi = 3.46$)). The more ionic nature of the CaOx Me – O bond makes it harder to break than the others. For further investigation of the strength of this bond in relation to the XPS spectra, it would be interesting to study the satellites of the Me and O 1s lines. Indeed, Chenakin found out that the intensity of the primary satellite demonstrates a reverse correlation with $\Delta\chi$. This suggests that the emission of photoelectrons constituting the satellite is influenced by the strength of the Me–O bond. The problem is that the larger differences between our MetOx make these investigations difficult to apply in the Me spectra.

In the event of a future XPS analysis, it would be interesting to record the oxygen Auger spectra and the higher-BE satellites in C 1s and O 1s lines to draw more conclusions concerning the Me – O bond. With a view to a rigorous comparison with the Chenakin et al. paper, the analysis technique using indium or gold foil could also be perfected. However, it is important to step back from the usefulness of such measurements in the context of cultural heritage metal oxalates and to assess their usability before starting them.

The multiple distinctive features found in metallic oxalates during this study instill hope for the possibility of identifying them in more complex samples. Since they are scarcely observable using ToF-SIMS, especially calcium oxalate, considering the analysis of 3D mock-ups (at least) through XPS could prove intriguing. Of course, it would be necessary for the relevant oxalates to be present in sufficient quantities within the sample to obtain conclusive results, considering the lower sensitivity of this technique compared to ToF-SIMS. Furthermore, special attention should be given to the duration of the analysis, aiming to keep it as brief as possible to avert any degradation that might lead to a decrease in the concentration of metal oxalate beneath its XPS detection threshold. Before attempting this on historical cross-sections, a methodology should be established on mock-ups. Especially as chemical changes may occur, and the results may not be representative of the actual materiality of the artwork.

Part V

Conclusion

Chapter 10

Conclusions and future prospects

In the first part of this work, we have investigated copper and calcium oxalates in six historical cross-sections and one mock-up in ToF-SIMS. Three main parameters were taken into account to assess their presence.
The first one was the consistency with ATR-µFTIR results. The areas analyzed in ToF-SIMS were chosen based on the areas presenting these oxalates in ATR-µFTIR. The latter having a higher depth of information than ToF-SIMS, a first possible explanation for the inconclusiveness of ToF-SIMS analyses on C32-038, C88-145 and C101-040 is that the oxalates detected in ATR-µFTIR were to deep to be observed in ToF-SIMS.
Secondly, their localization and colocalization with their corresponding fragment ions was checked. If the intensity for one of these compounds was homogeneous over all the image, or dispersed in some locations without any evident connection to these ions, the compounds were considered absent of the sample. For CuOx, the main fragments observed correlated with $CuC_2O_4^-$ were the metallic ions $^{(65)}Cu^+$ and $^{(65)}Cu^-$. For CaOx, it was Ca^+ and, interestingly, $CaOH^+$. Maybe the latter originated from the dissociation of one carboxylic function of the two in calcium oxalate molecules. As mentioned in the XPS study, the Ca−O bond is relatively strong and this bond might have remained intact after becoming detached from the rest of the metal oxalate.
Thirdly, the definition of the $CuC_2O_4^-$ and $CaC_2O_4^-$ peaks. Again, this is a frequent issue faced in historical cross-sections, as there are a lot of different compounds that interfere with the signal of the peaks of interest, already of low intensities in the spectra. The reason why these compounds are typically observed with very low intensities is likely attributed to their low ionization probabilities. It may be worthwhile to investigate the feasibility of using matrices to increase these ionization probabilities in future research (on mock-ups small enough, and it

would be quite a complex research to find the adequate matrices). While CuOx had been detected by H. Lebrun, CaOx was even more hard to detect. In this work however, cross-sections C21-053, C30-153 and C17-085 interestingly showed relatively well defined peaks where the $CaC_2O_4^-$ peak should appear, reviving hopes of its detection in ToF-SIMS. It is important to remain critical, however, as the resolution of the instrument does not allow us to be certain that this is indeed an oxalate peak, and not a superposition of contamination peaks that would appear by coincidence at this m/z value. An attempt was made to address this need for higher mass resolution by testing delayed extraction on the modck-up. As a matter of fact, DE allowed the visualization of several sub-peaks rather than a featureless structure for oxalate and calcium oxalate. However, no oxalate nor calcium peak *per se* was observed, and the ion mappings corresponding to these ions were not much more precise. Moreover, the low-mass peaks are lost when using DE and it appeared that the mock-up were slightly deformed after the use of DE. Nevertheless, it could be interesting to pursue the development of this technique in other mock-ups, or to analyse cross-sections in ToF-SIMS with higher mass-resolutions, such as 3D OrbiSIMS for instance [72].
The process of polishing could also have caused sample damage, including cracks and blending of the compounds at the surface of the sample, making species identification challenging. Researchers are exploring alternative techniques such as ion beam milling to create clean cross-sections for analysis, involving thinning samples through ion bombardment to avoid contamination and distortion. This method promises accurate analysis without the drawbacks of traditional polishing. In a more general way, ToF-SIMS did confirm its usefulness of observing metal and organic ions together, although difficulties in interpreting results persist.

The discovery of distinct characteristics in CaOx, CuOx, PbOx and ZnOx during the XPS research also raised optimism for their potential identification in more intricate samples. Due to their low detections using ToF-SIMS, exploring the use of XPS for 3D analyses appears intriguing. In particular, an XPS instrument equipped with a GCIB would be less destructive. Of course, the presence of these relevant oxalates in sufficient quantities within the sample would be essential to derive conclusive outcomes, given the lower sensitivity of this method compared to ToF-SIMS.
Attention must also be given to the analysis duration to prevent extensive degradation that could result in the metal oxalate's concentration falling below the XPS detection threshold. Before applying this approach to historical cross-sections, a systematic procedure should be established on mock-ups. This is especially

important as chemical alterations might occur, and the findings may not accurately represent the actual material composition of the artwork. The samples might also have a low and known roughness.

Ultimately, this master's thesis has furthered our knowledge of metal oxalates as degradation products in historical oil paintings. Despite the persistent challenges in obtaining consistent ToF-SIMS results, there are still numerous pathways to explore for advancing this comprehension. Obstacles have not only prompted innovative thinking but also provided a foundation for XPS studies, fostering the continued advancement of research within this domain.

Bibliography

[1] Hadelin Le Brun. "Study of the formation of metal oxalates and soaps in oil paintings from the Southern Netherlands using ToF-SIMS". Master Thesis. Louvain-la-Neuve: UCLouvain, 2021.

[2] Jana SANYOVA et al. "METOX: Metal-oxalates in the 15th and 16th Century Southern Netherlandish oil paintings". BELSPO-BRAIN.

[3] *Mieux comprendre la formation des oxalates métalliques dans les couches picturales à l'huile avec le projet MetOx | KIK-IRPA*. URL: https://www.kikirpa.be/en/projects/projet-metox?lang=en (visited on 03/13/2023).

[4] Giovanna Bitossi et al. "Spectroscopic Techniques in Cultural Heritage Conservation: A Survey". In: *Applied Spectroscopy Reviews* 40.3 (Aug. 2005), pp. 187–228. ISSN: 0570-4928, 1520-569X. DOI: 10.1081/ASR-200054370. URL: http://www.tandfonline.com/doi/abs/10.1081/ASR-200054370 (visited on 04/08/2023).

[5] María Dolores Gayo and Maite Jover de Celis. *The evolution of preparations for painting on canvas in sixteenth century Spain - Museo Nacional del Prado*. URL: https://www.museodelprado.es/en/learn/research/studies-and-restorations/resource/the-evolution-of-preparations-for-painting-on/39cd7ac1-b445-49da-9362-61dbc19c5ed8#nota-2 (visited on 04/08/2023).

[6] Eugenia Geddes da Filicaia, Richard P. Evershed, and David A. Peggie. "Review of recent advances on the use of mass spectrometry techniques for the study of organic materials in painted artworks". In: *Analytica Chimica Acta* 1246 (Mar. 2023), p. 340575. ISSN: 00032670. DOI: 10.1016/j.aca.2022.340575. URL: https://linkinghub.elsevier.com/retrieve/pii/S0003267022011461 (visited on 04/08/2023).

[7] "Methods and materials of Northern European painting in the National Gallery, 1400-1550". In: *National Gallery Technical Bulletin* (1997).

[8] Ra. Bonewitz. *Rocks and minerals*. London; New York: DK Publishing, 2012.

[9] Nati Salvadó et al. "Identification and Distribution of Metal Soaps and Oxalates in Oil and Tempera Paint Layers in Fifteenth-Century Altarpieces Using Synchrotron Radiation Techniques". In: *Metal Soaps in Art*. Ed. by Francesca Casadio et al. Series Title: Cultural Heritage Science. Cham: Springer International Publishing, 2019, pp. 195–210. DOI: 10.1007/978-3-319-90617-1_11. URL: http://link.springer.com/10.1007/978-3-319-90617-1_11 (visited on 12/08/2022).

[10] Sophie Dallongeville et al. "Proteins in Art, Archaeology, and Paleontology: From Detection to Identification". In: *Chemical Reviews* 116.1 (Jan. 13, 2016), pp. 2–79. ISSN: 0009-2665, 1520-6890. DOI: 10.1021/acs.chemrev.5b00037. URL: https://pubs.acs.org/doi/10.1021/acs.chemrev.5b00037 (visited on 12/08/2022).

[11] Sanyova Jana et al. *The Ghent Altarpiece: The challenges of a Complex Stratigraphy from a Chemical Point of View*. 2021.

[12] Geert Van der Snickt et al. "Dual mode standoff imaging spectroscopy documents the painting process of the Lamb of God in the *Ghent Altarpiece* by J. and H. Van Eyck". In: *Science Advances* 6.31 (July 31, 2020), eabb3379. ISSN: 2375-2548. DOI: 10.1126/sciadv.abb3379. URL: https://www.science.org/doi/10.1126/sciadv.abb3379 (visited on 12/08/2022).

[13] Marika Spring. "New insights into the materials of fifteenth- and sixteenth-century Netherlandish paintings in the National Gallery, London". In: *Heritage Science* 5.1 (Sept. 2017). DOI: 10.1186/s40494-017-0152-3. URL: https://doi.org/10.1186/s40494-017-0152-3.

[14] Kim Pilkjær Simonsen et al. "Formation of zinc oxalate from zinc white in various oil binding media: the influence of atmospheric carbon dioxide by reaction with 13CO2". In: *Heritage Science* 8.1 (Dec. 2020). DOI: 10.1186/s40494-020-00467-z. URL: https://doi.org/10.1186/s40494-020-00467-z.

[15] Ralph Mayer. *The Artist's Handbook of Materials and Techniques*. London: FABER AND FABER, 1951.

[16] Lizet Klaassen and Dieter Lampens. *Harmony in bright colors: Memling's "God the father with singing and music-making angels" restored*. Turnhout, Belgium: Brepols, 2021. ISBN: 978-2-503-58028-9.

[17] Atheer A Mahmood et al. *Studying of transition metal complexes containing oxalate ion with antibacterial activity*. 2015.

[18] Armida Sodo et al. "Raman and time of flight secondary ion mass spectrometry investigation answers specific conservation questions on Bosch painting *Saint Wilgefortis Triptych*". In: *Journal of Raman Spectroscopy* 50.2 (Feb. 2019), pp. 150–160. ISSN: 03770486. DOI: 10.1002/jrs.5479. URL: https://onlinelibrary.wiley.com/doi/10.1002/jrs.5479 (visited on 11/06/2022).

[19] PubChem. *Oxalate*. URL: https://pubchem.ncbi.nlm.nih.gov/compound/71081 (visited on 03/07/2023).

[20] PubChem. *palmitate*. URL: https://pubchem.ncbi.nlm.nih.gov/substance/3050 (visited on 05/23/2023).

[21] PubChem. *Stearate*. URL: https://pubchem.ncbi.nlm.nih.gov/compound/3033836 (visited on 05/23/2023).

[22] Francisco Mederos-Henry. *Oxalates métalliques dans la peinture à l'huile des Pays-Bas Méridionaux des 15e et 16e siècles (METOX): final report*. Tech. rep. SP3228. Brussels: Belgian Science policy, 2023.

[23] *Tof - SIMS | UCLouvain*. URL: https://uclouvain.be/en/research-institutes/imcn/tof-sims.html (visited on 11/17/2022).

[24] Eun Ji Park et al. "Dynamic secondary ion mass spectroscopy of Au nanoparticles on Si wafer using Bi_3^+ as primary ion coupled with surface etching by Ar cluster ion beam: The effect of etching conditions on surface structure". In: *Journal of Applied Physics* 123.1 (Jan. 7, 2018), p. 015303. ISSN: 0021-8979, 1089-7550. DOI: 10.1063/1.5011686. URL: http://aip.scitation.org/doi/10.1063/1.5011686 (visited on 03/16/2023).

[25] Arnaud Delcorte and Pierre Eloy. Lecture notes in *LMAPR2631 - Surface Analysis* at the Université Catholique de Louvain.

[26] J. C. Vickerman and David Briggs. *ToF-SIMS: Materials Analysis by Mass Spectrometry*. IM Publications, 2013. 742 pp. ISBN: 978-1-906715-17-5.

[27] Cody Cushman et al. "Sample Charging in ToF-SIMS: How it Affects the Data that are Collected and How to Reduce it". In: *Characterization of Thin Films and Materials* (2018).

[28] Amy V. Walker. "Secondary Ion Mass Spectrometry". In: *Encyclopedia of Spectroscopy and Spectrometry*. Elsevier, 2017, pp. 44–49. ISBN: 978-0-12-803224-4. DOI: 10.1016/B978-0-12-803224-4.00022-4. URL: https://linkinghub.elsevier.com/retrieve/pii/B9780128032244000224 (visited on 03/21/2023).

[29] *Time-of-Flight Secondary Ion Mass Spectrometry (ToF-SIMS) – Labs Services*. URL: https://www.labs-services.com/product/time-of-flight-secondary-ion-mass-spectrometry-tof-sims/ (visited on 03/16/2023).

[30] Quentin P. Vanbellingen et al. "Time-of-flight secondary ion mass spectrometry imaging of biological samples with delayed extraction for high mass and high spatial resolutions". In: *Rapid Communications in Mass Spectrometry* 29.13 (May 2015), pp. 1187–1195. DOI: 10.1002/rcm.7210. URL: https://doi.org/10.1002/rcm.7210.

[31] Koivula et al. "Characterization of Pigment Particle Surfaces by ToF-SIMS". In: *TAPPI Advanced Coating Fundamentals Symposium* (2006), p. 7.

[32] Morena Iorio et al. "Exploring Manufacturing Process and Degradation Products of Gilt and Painted Leather". In: *Applied Sciences* 9.15 (July 2019), p. 3016. DOI: 10.3390/app9153016. URL: https://doi.org/10.3390/app9153016.

[33] Manale Noun et al. "High mass and spatial resolution mass spectrometry imaging of Nicolas Poussin painting cross section by cluster TOF-SIMS". In: *Journal of Mass Spectrometry* 51.12 (Nov. 2016), pp. 1196–1210. DOI: 10.1002/jms.3885. URL: https://doi.org/10.1002/jms.3885.

[34] Pascale Richardin et al. "Identification of Different Copper Green Pigments in Renaissance Paintings by Cluster-TOF-SIMS Imaging Analysis". In: *Journal of the American Society for Mass Spectrometry* 22.10 (June 2011), pp. 1729–1736. DOI: 10.1007/s13361-011-0171-3. URL: https://doi.org/10.1007/s13361-011-0171-3.

[35] Zachary E. Voras et al. "ToF–SIMS imaging of molecular-level alteration mechanisms in Le Bonheur de vivre by Henri Matisse". In: *Applied Physics A* 121.3 (Nov. 2015), pp. 1015–1030. ISSN: 0947-8396, 1432-0630. DOI: 10.1007/s00339-015-9508-2. URL: http://link.springer.com/10.1007/s00339-015-9508-2 (visited on 11/05/2022).

[36] Caroline Bouvier et al. “Time-of-Flight Secondary Ion Mass Spectrometry Imaging of Cross Sections from the Bacchanals Paintings of Nicolas Poussin”. In: *Analytical Chemistry* 93.10 (Mar. 2021), pp. 4463–4471. DOI: 10.1021/acs.analchem.0c04471. URL: https://doi.org/10.1021/acs.analchem.0c04471.

[37] Jana Sanyova et al. “Unexpected Materials in a Rembrandt Painting Characterized by High Spatial Resolution Cluster-TOF-SIMS Imaging”. In: *Analytical Chemistry* 83.3 (Feb. 1, 2011), pp. 753–760. ISSN: 0003-2700, 1520-6882. DOI: 10.1021/ac1017748. URL: https://pubs.acs.org/doi/10.1021/ac1017748 (visited on 12/08/2022).

[38] Vincent Mazel and Pascale Richardin. “ToF-SIMS Study of Organic Materials in Cultural Heritage: Identification and Chemical Imaging”. In: *Organic Mass Spectrometry in Art and Archaeology*. Ed. by Maria Perla Colombini and Francesca Modugno. Chichester, UK: John Wiley & Sons, Ltd, Aug. 21, 2009, pp. 433–457. DOI: 10.1002/9780470741917.ch15. URL: https://onlinelibrary.wiley.com/doi/10.1002/9780470741917.ch15 (visited on 12/08/2022).

[39] Chaudhry Amjad Ali Ghumman. “Time-of-Flight Secondary Ion Mass Spectrometry: New application for urinary stones analysis”. PhD thesis. Faculdade de Ciências e Tecnologia, Universidade Nova de Lisboa, 2013.

[40] C. A. A. Ghumman et al. “TOF-SIMS VG Ionex IX23LS: upgrade and application for the urinary stones analysis: Upgraded TOF-SIMS VG Ionex IX23LS for urinary stones analysis”. In: *Surface and Interface Analysis* 45.1 (Jan. 2013), pp. 532–536. ISSN: 01422421. DOI: 10.1002/sia.5031. URL: https://onlinelibrary.wiley.com/doi/10.1002/sia.5031 (visited on 11/06/2022).

[41] C. Amjad A. Ghumman et al. “Identification of human calculi with time-of-flight secondary ion mass spectrometry: Identification of human calculi with TOF-SIMS”. In: *Rapid Communications in Mass Spectrometry* 24.2 (Jan. 30, 2010), pp. 185–190. ISSN: 09514198. DOI: 10.1002/rcm.4376. URL: https://onlinelibrary.wiley.com/doi/10.1002/rcm.4376 (visited on 11/06/2022).

[42] C. A. A. Ghumman et al. “TOF-SIMS study of cystine and cholesterol stones: Cystine and cholesterol stones”. In: *Journal of Mass Spectrometry* 47.5 (May 2012), pp. 547–551. ISSN: 10765174. DOI: 10.1002/jms.2972. URL:

https://onlinelibrary.wiley.com/doi/10.1002/jms.2972 (visited on 11/04/2022).

[43] *XPS and UPS Background – Grimmgroup Research*. URL: https://grimmgroup.net/research/xps/background/ (visited on 04/11/2023).

[44] Yang Leng. *Materials Characterization*. Chichester, UK: John Wiley & Sons, Ltd, Apr. 21, 2008. DOI: 10.1002/9780470823002. URL: http://doi.wiley.com/10.1002/9780470823002 (visited on 04/11/2023).

[45] *XPS - ESCA*. UCLouvain. URL: https://uclouvain.be/en/research-institutes/imcn/such/xps-esca.html (visited on 04/11/2023).

[46] S. Tougaard. "SURFACE ANALYSIS | X-ray Photoelectron Spectroscopy". In: *Reference Module in Chemistry, Molecular Sciences and Chemical Engineering*. Elsevier, 2013, B9780124095472005278. ISBN: 978-0-12-409547-2. DOI: 10.1016/B978-0-12-409547-2.00527-8. URL: https://linkinghub.elsevier.com/retrieve/pii/B9780124095472005278 (visited on 04/11/2023).

[47] Mauro Sardela, ed. *Practical Materials Characterization*. New York, NY: Springer New York, 2014. DOI: 10.1007/978-1-4614-9281-8. URL: https://link.springer.com/10.1007/978-1-4614-9281-8 (visited on 04/12/2023).

[48] Gujie Qian, Yubiao Li, and Andrea R. Gerson. "Applications of surface analytical techniques in Earth Sciences". In: *Surface Science Reports* 70.1 (Mar. 2015), pp. 86–133. ISSN: 01675729. DOI: 10.1016/j.surfrep.2015.02.001. URL: https://linkinghub.elsevier.com/retrieve/pii/S0167572915000035 (visited on 11/04/2022).

[49] Karol Nass. "Radiation damage in protein crystallography at X-ray free-electron lasers". In: *Acta Crystallographica Section D Structural Biology* 75.2 (Jan. 2019), pp. 211–218. DOI: 10.1107/s2059798319000317. URL: https://doi.org/10.1107/s2059798319000317.

[50] Markus Ammann. Lecture notes in *Characterization of Catalysts and Surfaces* at the Paul Scherrer Institut.

[51] G. Greczynski and L. Hultman. "X-ray photoelectron spectroscopy: Towards reliable binding energy referencing". In: *Progress in Materials Science* 107 (Jan. 2020), p. 100591. ISSN: 00796425. DOI: 10.1016/j.pmatsci.2019.100591. URL: https://linkinghub.elsevier.com/retrieve/pii/S0079642519300738 (visited on 04/15/2023).

[52] A.F. Carley and D.J. Morgan. "Surface Analysis: X-Ray Photoelectron Spectroscopy". In: *Reference Module in Materials Science and Materials Engineering*. Elsevier, 2016, B9780128035818033117. ISBN: 978-0-12-803581-8. DOI: 10.1016/B978-0-12-803581-8.03311-7. URL: https://linkinghub.elsevier.com/retrieve/pii/B9780128035818033117 (visited on 04/18/2023).

[53] Hamed Simchi. Presentation on *X-Ray Photoelectron Spectroscopy (XPS)* from the NACK Network.

[54] A. Coetzee et al. "Kinetics of the thermal dehydrations and decompositions of some mixed metal oxalates". In: *Journal of Thermal Analysis* 41.2-3 (Feb. 1994), pp. 357–385. DOI: 10.1007/bf02549321. URL: https://doi.org/10.1007/bf02549321.

[55] S.P. Chenakin et al. "Surface analysis of transition metal oxalates: Damage aspects". In: *Journal of Electron Spectroscopy and Related Phenomena* 209 (May 2016), pp. 66–77. DOI: 10.1016/j.elspec.2016.04.001. URL: https://doi.org/10.1016/j.elspec.2016.04.001.

[56] Sergey Chenakin and Norbert Kruse. "XPS characterization of transition metal oxalates". In: *Applied Surface Science* 515 (June 2020), p. 146041. DOI: 10.1016/j.apsusc.2020.146041. URL: https://doi.org/10.1016/j.apsusc.2020.146041.

[57] Zhaoying Wang et al. "ToF-SIMS depth profiling of insulating samples, interlaced mode or non-interlaced mode?" In: *Surface and Interface Analysis* 46.S1 (Feb. 2014), pp. 257–260. DOI: 10.1002/sia.5419. URL: https://doi.org/10.1002/sia.5419.

[58] Thomas R. Gengenbach et al. "Practical guides for x-ray photoelectron spectroscopy (XPS): Interpreting the carbon 1s spectrum". In: *Journal of Vacuum Science & Technology A: Vacuum, Surfaces, and Films* 39.1 (Jan. 2021). DOI: 10.1116/6.0000682. URL: https://doi.org/10.1116/6.0000682.

[59] Kepa Castro et al. "Green Copper Pigments Biodegradation in Cultural Heritage: From Malachite to Moolooite, Thermodynamic Modeling, X-ray Fluorescence, and Raman Evidence". In: *Analytical Chemistry* 80.11 (Apr. 2008), pp. 4103–4110. DOI: 10.1021/ac800255w. URL: https://doi.org/10.1021/ac800255w.

[60] JEOL USA. *Broad Ion Beam Milling - Cross-Section Polisher (CP)*. 2023-08-11. 2023. URL: https://www.jeolusa.com/PRODUCTS/Sample-Preparation-Tools/Cross-Section-Polisher.

[61] John F Moulder, William F Stickle, and Peter E Sobol. *Handbook of X-ray photoelectron spectroscopy*. Perkin-Elmer, Physical Electronics Division, Sept. 1992.

[62] Mark C. Biesinger et al. "Resolving surface chemical states in XPS analysis of first row transition metals, oxides and hydroxides: Sc, Ti, V, Cu and Zn". In: *Applied Surface Science* 257.3 (Nov. 2010), pp. 887–898. DOI: 10.1016/j.apsusc.2010.07.086. URL: https://doi.org/10.1016/j.apsusc.2010.07.086.

[63] C. Hinnen, C. Nguyen van Huong, and P. Marcus. "A comparative X-ray photoemission study of $Bi_2Sr_2CaCu_2O_{8+\delta}$ and $Bi_1 \cdot 6\,Pb_0 \cdot 4\,Sr_2CaCu_2O_{8+\delta'}$". In: *Journal of Electron Spectroscopy and Related Phenomena* 73.3 (1995), pp. 293–304. ISSN: 0368-2048. DOI: https://doi.org/10.1016/0368-2048(94)02288-7. URL: https://www.sciencedirect.com/science/article/pii/0368204894022887.

[64] Cedric Powell. *X-ray Photoelectron Spectroscopy Database XPS, Version 4.1, NIST Standard Reference Database 20*. en. 1989. DOI: 10.18434/T4T88K. URL: http://srdata.nist.gov/xps/.

[65] E. Clementi and D. L. Raimondi. "Atomic Screening Constants from SCF Functions". In: *The Journal of Chemical Physics* 38.11 (June 1963), pp. 2686–2689. DOI: 10.1063/1.1733573. URL: https://doi.org/10.1063/1.1733573.

[66] E. Clementi, D. L. Raimondi, and W. P. Reinhardt. "Atomic Screening Constants from SCF Functions. II. Atoms with 37 to 86 Electrons". In: *The Journal of Chemical Physics* 47.4 (Aug. 1967), pp. 1300–1307. DOI: 10.1063/1.1712084. URL: https://doi.org/10.1063/1.1712084.

[67] Pavel Karen, Patrick McArdle, and Josef Takats. "Comprehensive definition of oxidation state (IUPAC Recommendations 2016)". In: *Pure and Applied Chemistry* 88.8 (Aug. 2016), pp. 831–839. DOI: 10.1515/pac-2015-1204. URL: https://doi.org/10.1515/pac-2015-1204.

[68] J.M. Ferreira et al. "Development and characterisation of zinc oxalate conversion coatings on zinc". In: *Corrosion Science* 137 (June 2018), pp. 13–32. ISSN: 0010938X. DOI: 10.1016/j.corsci.2018.03.011. URL: https:

//linkinghub.elsevier.com/retrieve/pii/S0010938X17321364 (visited on 07/11/2023).

[69] Anna Maria Salvi et al. “Comparative Spectra Illustrating Degradation of CaC2O4·H2O During XPS Analysis”. In: *Surface Science Spectra* 22.1 (Mar. 2015), pp. 21–31. DOI: 10.1116/11.20141101. URL: https://doi.org/10.1116/11.20141101.

[70] Mark C. Biesinger. “Advanced analysis of copper X-ray photoelectron spectra”. In: *Surface and Interface Analysis* 49.13 (May 2017), pp. 1325–1334. DOI: 10.1002/sia.6239. URL: https://doi.org/10.1002/sia.6239.

[71] Shanshan Chen et al. “X-ray photoelectron spectroscopy study of energy-band alignments of ZnO on buffer layer Lu_2O_3”. In: *Physics Letters A* 380.7-8 (Feb. 2016), pp. 970–972. DOI: 10.1016/j.physleta.2015.12.038. URL: https://doi.org/10.1016/j.physleta.2015.12.038.

[72] Melissa K Passarelli et al. “The 3D OrbiSIMS—label-free metabolic imaging with subcellular lateral resolution and high mass-resolving power”. In: *Nature Methods* 14.12 (Nov. 2017), pp. 1175–1183. DOI: 10.1038/nmeth.4504. URL: https://doi.org/10.1038/nmeth.4504.

Appendix A

Paintings from which the analyzed cross-sections originate

Figure A.1: *Lamentation over the dead Christ* by Jacob Jordaens (cross-section C88-145), belonging to the Maagdenhuis Museum.

Figure A.2: *The Seven Joys of Our Lady* by L. Blondeel (cross-sections C101-040 A and B), belonging to Cathedral of Our Lady in Tournai, Belgium.

Figure A.3: *Holy Trinity* by the Master of the Holy Blood (cross-section C32-038), belonging to the Royal Museums of Fine Arts of Belgium (MRBAB-KMSKB).

Figure A.4: *Adam and Eve* by the Master of the Mansi Magdalen (cross-section C30-153), belonging to the Royal Museums of Fine Arts of Belgium (MRBAB-KMSKB).

Figure A.5: *The Resurrection of Christ* by Peter Paul Rubens (cross-section C21-053), belonging to the Cathedral of Our Lady in Antwerp, Belgium.

Figure A.6: *Pietà* by Petrus Christus (cross-section C17-085), belonging to the Royal Museums of Fine Arts of Belgium (MRBAB-KMSKB).

Appendix B

Presentation of historical cross-section 101-040 A

The first cross-sections analyzed were two fragments of a single artwork described in Table 6.1 and shown in Appendix A. ATR-µFTIR indicates the presence of calcium oxalate in fragment A, shown in Figure B.1, that is the only one of the two presented in this work because the protocol was not yet perfected when analyzing fragment B, which showed no conclusive results.
Fragment A was mainly used to study the detection of CaOx, located in the upper part of the cross-section.

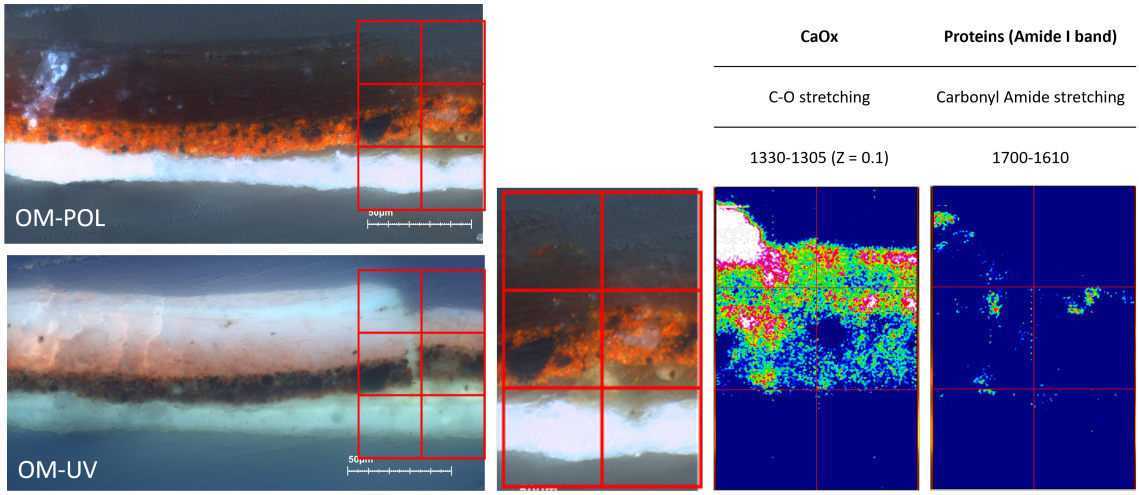

Figure B.1: Presentation of historical cross-section 101-040 A.

Appendix C

ToF-SIMS ion images of cross-sections in which no oxalate/CaOx/CuOx was detected

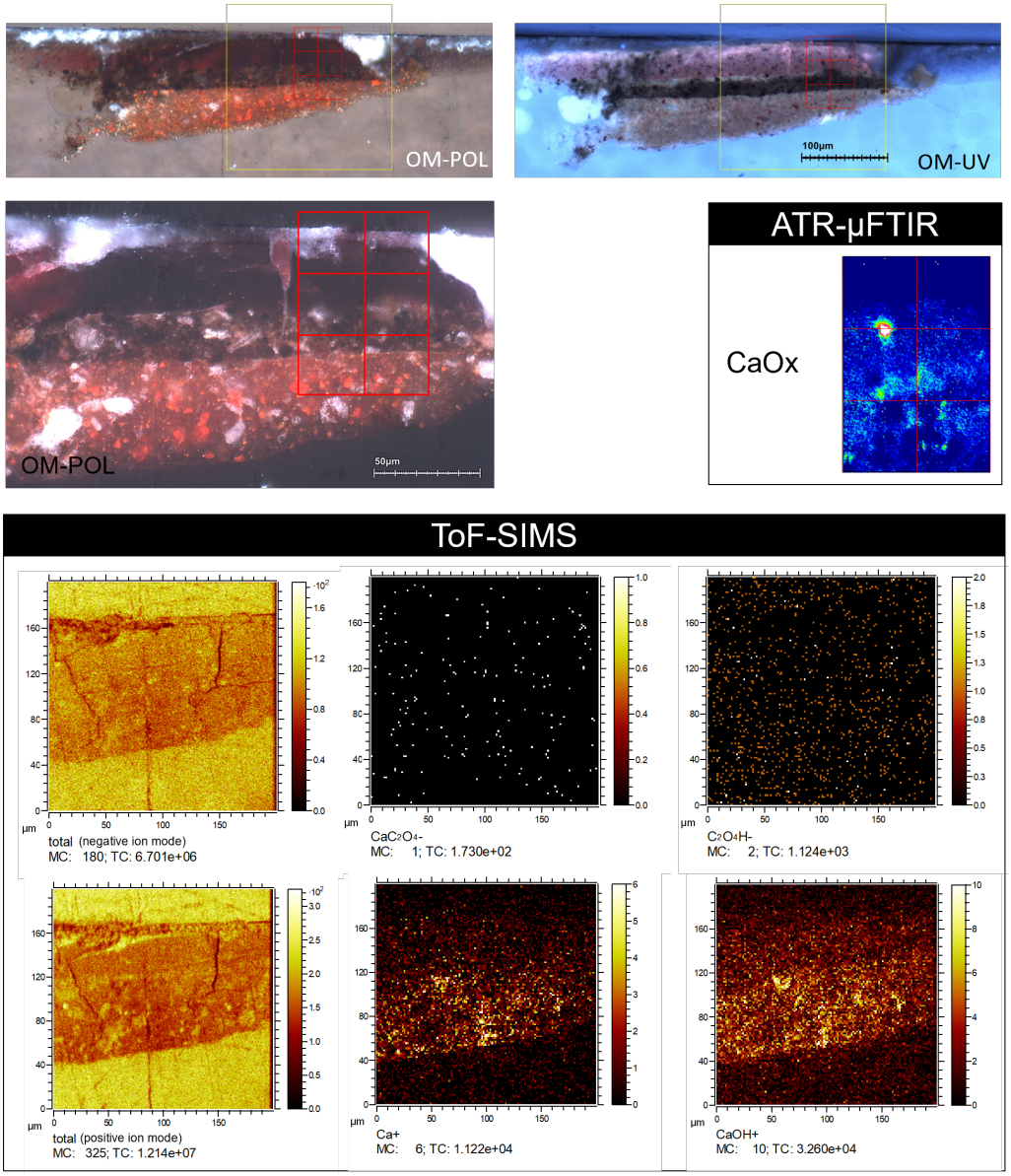

Figure C.1: POL and UV microphotographs, ATR-µFTIR mappings showing the spatial distribution of CaOx (1336-1296 cm^{-1}), and ToF-SIMS ion images of CaOx-related compounds in the left part of cross-section C88-145.

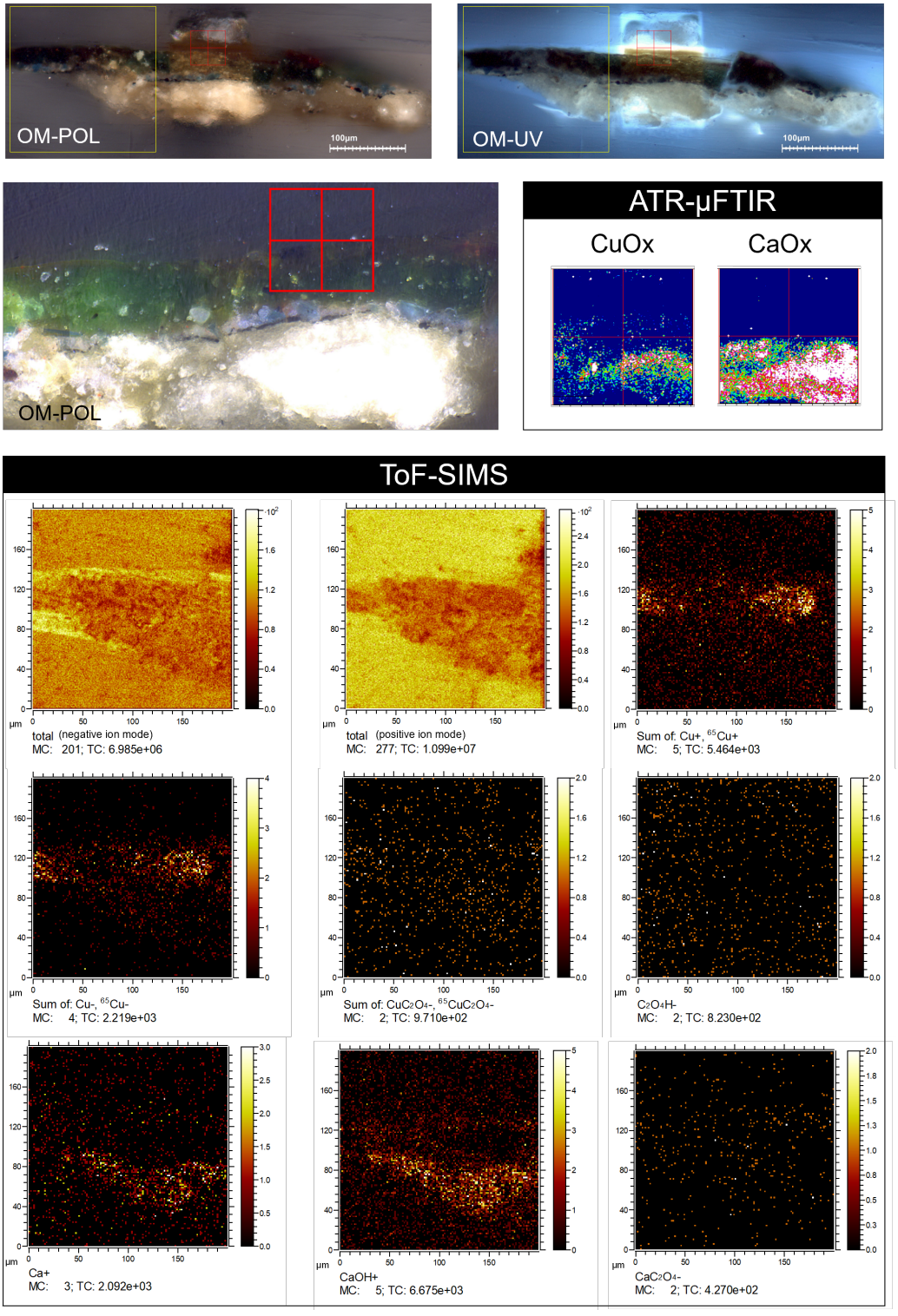

Figure C.2: POL and UV microphotographs, ATR-µFTIR mappings showing the spatial distribution of CaOx (1336-1296 cm^{-1}) and CuOx (1375-1355 cm^{-1}), and ToF-SIMS ion images of CaOx-related compounds in the left part of cross-section C32-038.

Appendix D

ToF-SIMS calcium oxalate peaks

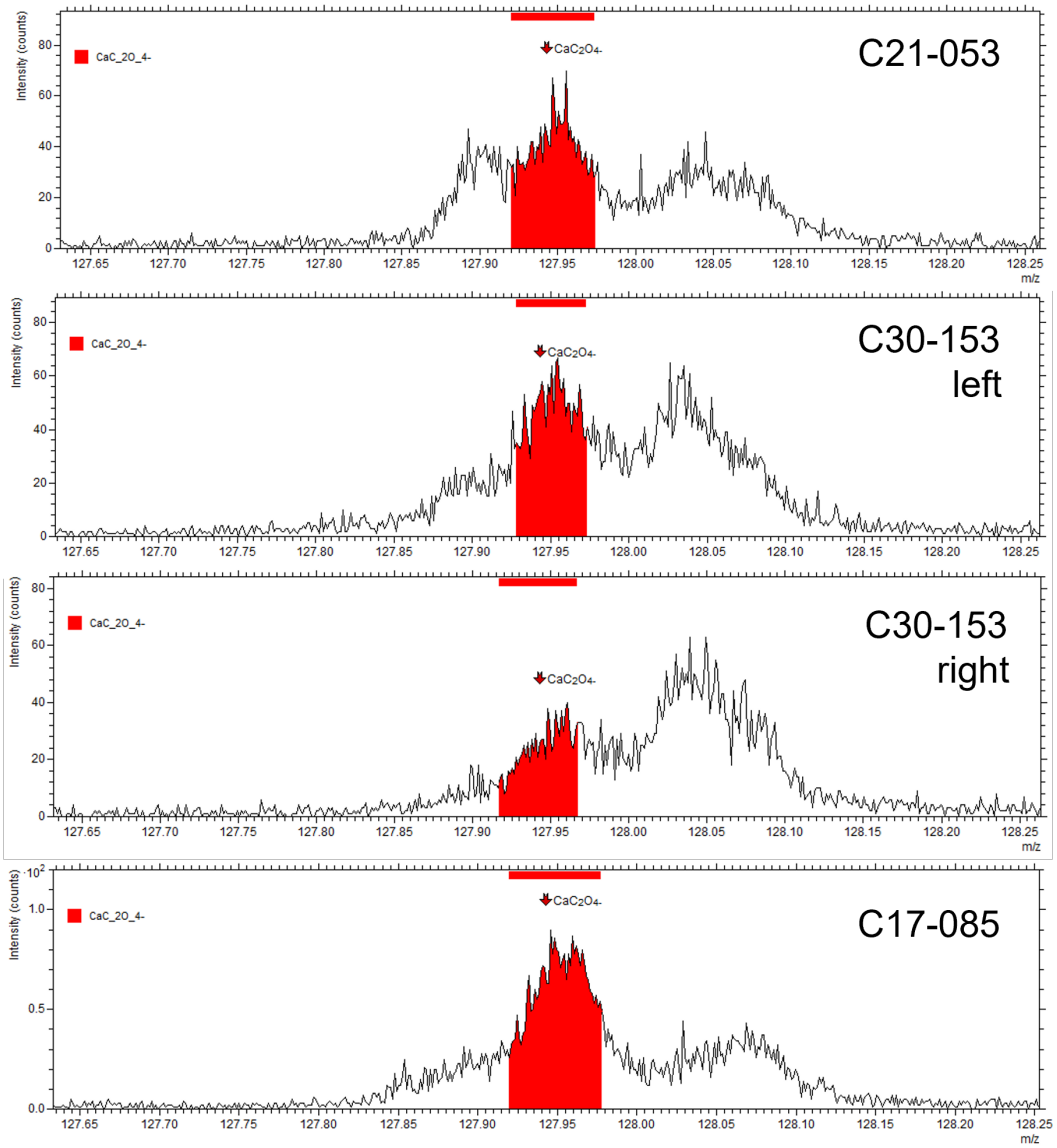

Figure D.1: ToF-SIMS $CaC_2O_4^-$ peaks in C21-053, C30-153 and C17-085.

Appendix E

Depth profiles on Mock-up H1-Ml-br-T6-N1

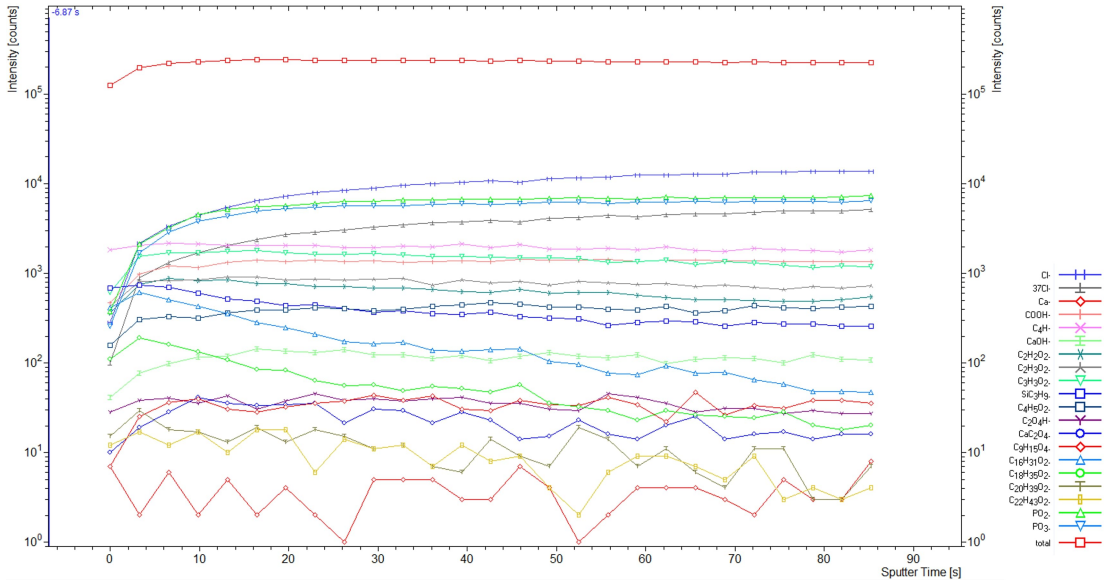

Figure E.1: Depth profiles of negative ions in mock-up H1-Ml-br-T6-N1.

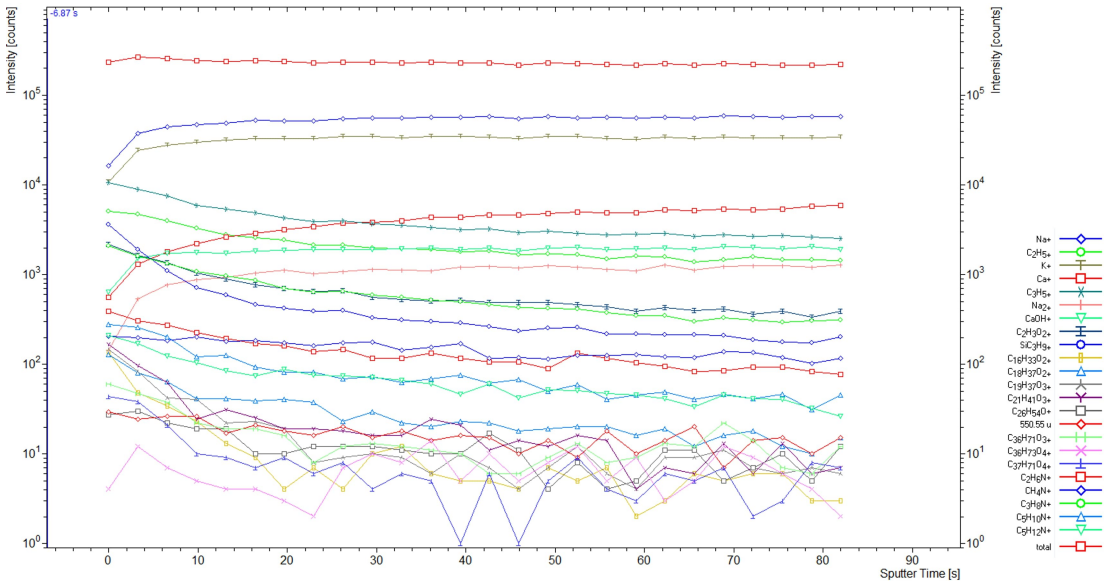

Figure E.2: Depth profiles of positive ions in mock-up H1-Ml-br-T6-N1.

Appendix F

XPS sample preparation

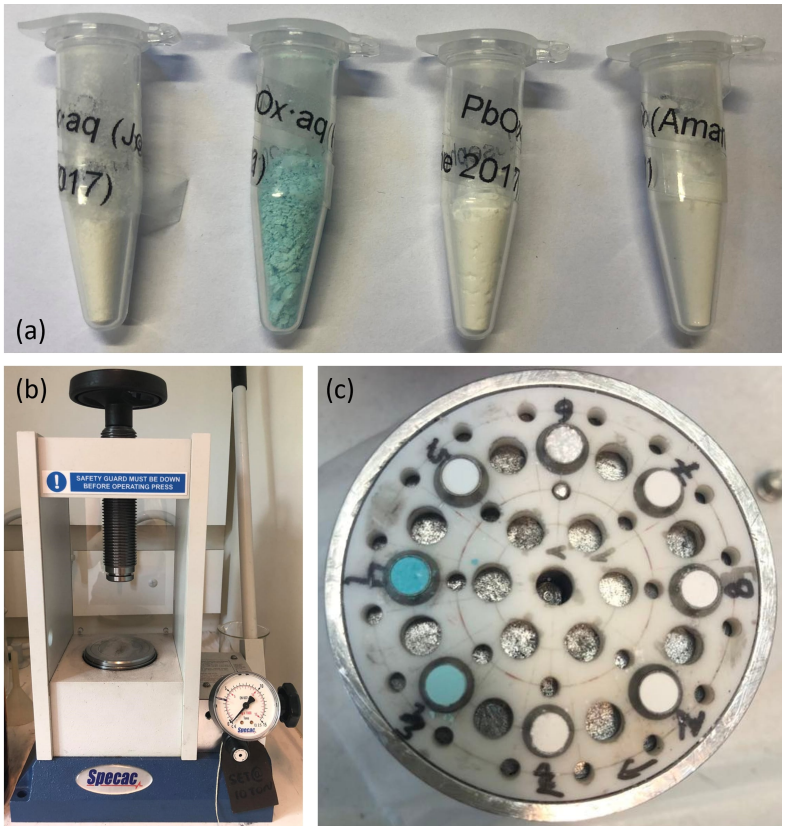

Figure F.1: XPS sample preparation. (a) Analyzed CaOx, CuOx, PbOx and ZnOx powders (from left to right). (b) Press. (c) Carousel. The powders visible in this particular image are the four metal oxalates and palmitates.

UNIVERSITÉ CATHOLIQUE DE LOUVAIN
École polytechnique de Louvain
Rue Archimède, 1 bte L6.11.01, 1348 Louvain-la-Neuve, Belgique | **www.uclouvain.be/epl**